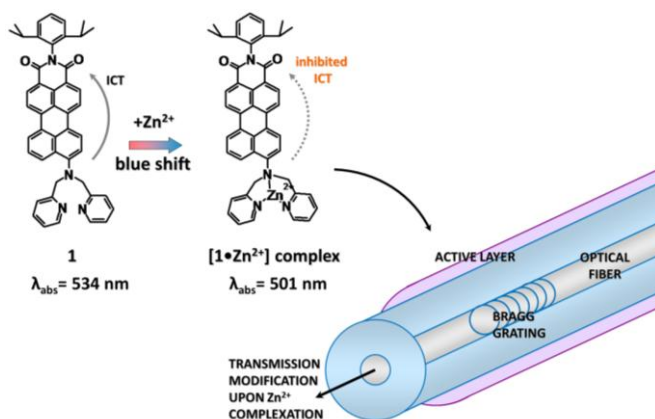# Chemical Sensors:
Modelling the Photophysics of Cation
Detection by Organic Dyes

Claire Tonnelé

Dissertation originale présentée

pour l'obtention du grade académique de Docteur en Sciences

de l'Université de Mons et de l'Université Bordeaux 1

2013

Membres du jury

Prof. Roberto LAZZARONI

Dr. David BELJONNE

Dr. Frédéric CASTET

Prof. Jean-Luc BRÉDAS

Prof. Toussaint ROBERT

Prof. Luisa DE COLA

Prof. Mark VAN DER AUWERAER

Et nous existerons en nous amusant,
en rêvant amours monstres
et univers fantastiques..

Arthur Rimbaud, *L'éclair*, 1873.

à los de qui cau

Résumé

La présence croissante de diverses substances dans notre environnement, conséquence des activités anthropiques de ces dernières décennies, a entraîné un besoin grandissant et urgent de nouveaux matériaux et dispositifs dans la quête de senseurs chimiques efficaces et fiables. D'énormes progrès technologiques ont permis de mettre à disposition toute une gamme d'outils techniques pour leur développement, en prenant en compte les exigences à respecter en terme de sélectivité ou de rapidité de réponse, entre autres. Dans ce contexte, les méthodes de chimie quantique permettent une compréhension fondamentale des processus en jeu dans la détection des espèces chimiques, et par extension, l'élaboration de manière rationnelle de nouveaux matériaux sensibles. Certaines molécules organiques pouvant être largement fonctionnalisées, elles constituent un point de départ idéal en raison des importantes modulations possibles de leurs propriétés par des modifications structurales appropriées.

Cette étude vise à développer de manière rationnelle des chromoionophores pour la complexation de cations par une approche combinant méthodes de chimie computationnelles et caractérisation par spectroscopie optique. Deux points principaux ont été traités à l'aide de la Théorie de la Fonctionnelle de la Densité (DFT) et son extension dépendante du temps (TD-DFT): d'une part les relations structure moléculaire-propriétés optiques de chromophores, d'autre part le phénomène de complexation. En particulier, la détection de l'ion Zn^{2+}, démontrée de manière théorique et expérimentale, est finalement réalisée après intégration du senseur moléculaire dans un dispositif à fibre optique.

Abstract

The increasing presence of various substances in our environment has brought about a growing need for rapid emergence of new materials and devices in the quest for efficient and reliable chemical sensors. Massive technological progress have made available an extensive range of technical tools to serve their development, accounting for the requirements to be fulfilled (selectivity, quick response..). In this context, quantum chemistry methods provide a fundamental understanding of the processes at stake in the detection of chemical species and allow for rational design of sensing materials. Certain organic molecules can be extensively functionalised and thus constitute an evident starting point owing to the tunability of their properties provided by appropriate choice of structural modifications. The versatility of some chromophores associated to the selectivity offered by receptor units constitute the research playground for the development of ever better chemosensors.

The present research aims at the rational development of chromoionophores for the complexation of cations, combining computational chemistry methods with basic spectroscopic characterisation. Using Density Functional Theory (DFT) and its time-dependent extension (TD-DFT), two main aspects were treated, namely the relationship between molecular structure and optical properties of organic chromophores featuring valuable characteristics, and the complexation phenomenon. Photophysics of Zn^{2+} ion detection were more specifically studied, and recognition was demonstrated with both quantum-chemical calculations and experiments, accounting for the future integration of the chemical sensor in an optical fibre device.

Modélisation des propriétés photophysiques de capteurs chimiques pour des applications de détection de cations par fibre optique.

Bien que naturellement présents dans notre environnement, la quantité d'ions métalliques a fortement augmenté durant les dernières décennies en raison d'intensives activités humaines, telles que les exploitations minières ou le rejet croissant de déchets industriels et agricoles, engendrant un intérêt grandissant pour la détection de ces espèces au sein des communautés industrielle et scientifique. Les méthodes analytiques à ce jour disponibles présentent pour la plupart des limitations techniques et/ou des coûts excessifs. Une alternative réside dans l'élaboration de senseurs chimiques abiotiques en se basant sur les principes de la chimie moléculaire et supra-moléculaire. Ainsi, un senseur chimique moléculaire peut être défini comme étant composé de 2 éléments: l'unité de reconnaissance de l'ion métallique, ou *ionophore*, responsable de la liaison spécifique avec un analyte donné, et l'unité *chromophore* qui permet de traduire la complexation en un signal optique, la détection étant généralement basée sur des modifications d'absorption ou d'émission de la lumière. Ces deux entités, dont les modifications permettent d'obtenir des propriétés et fonctionnalités désirées, peuvent être liées de façon covalente par un éventuel groupe espaceur, et constituent le senseur moléculaire chimique, aussi appelé *chromoionophore*. Ce travail de recherche vise à développer de tels systèmes de manière rationnelle en utilisant les outils de la chimie computationelle, principalement la Théorie de la Fonctionnelle de la Densité (DFT, pour Density Functional Theory) et son extension dépendante du temps (TD-DFT, pour Time-Dependent DFT), combinés à une caractérisation basique par spectroscopique optique. Pour cela, deux aspects principaux ont été abordés, à savoir les relations structure-propriétés optiques du chromophore, ainsi que les aspects photophysiques associés au phénomène de complexation. Nous nous sommes plus particulièrement focalisés à la détection de l'ion Zn^{2+}, intéressant dans le cadre du suivi de la corrosion de l'acier

galvanisé, considérant l'intégration du senseur chimique dans un futur dispositif à fibre optique.

1. Modulation des propriétés optiques et électroniques de colorants BODIPY.

L'étude des relations structure-propriétés optiques du chromophore a été menée sur la famille des BODIPYs, un colorant très populaire et largement utilisé dans diverses applications, telles que les dispositifs photovoltaïques luminescents, en raison de ses remarquables propriétés thermiques et photochimiques, entre autres, ainsi que sa grande versatilité résultant des multiples fonctionnalisations possibles du BODIPY non-substitué (Figure 1).
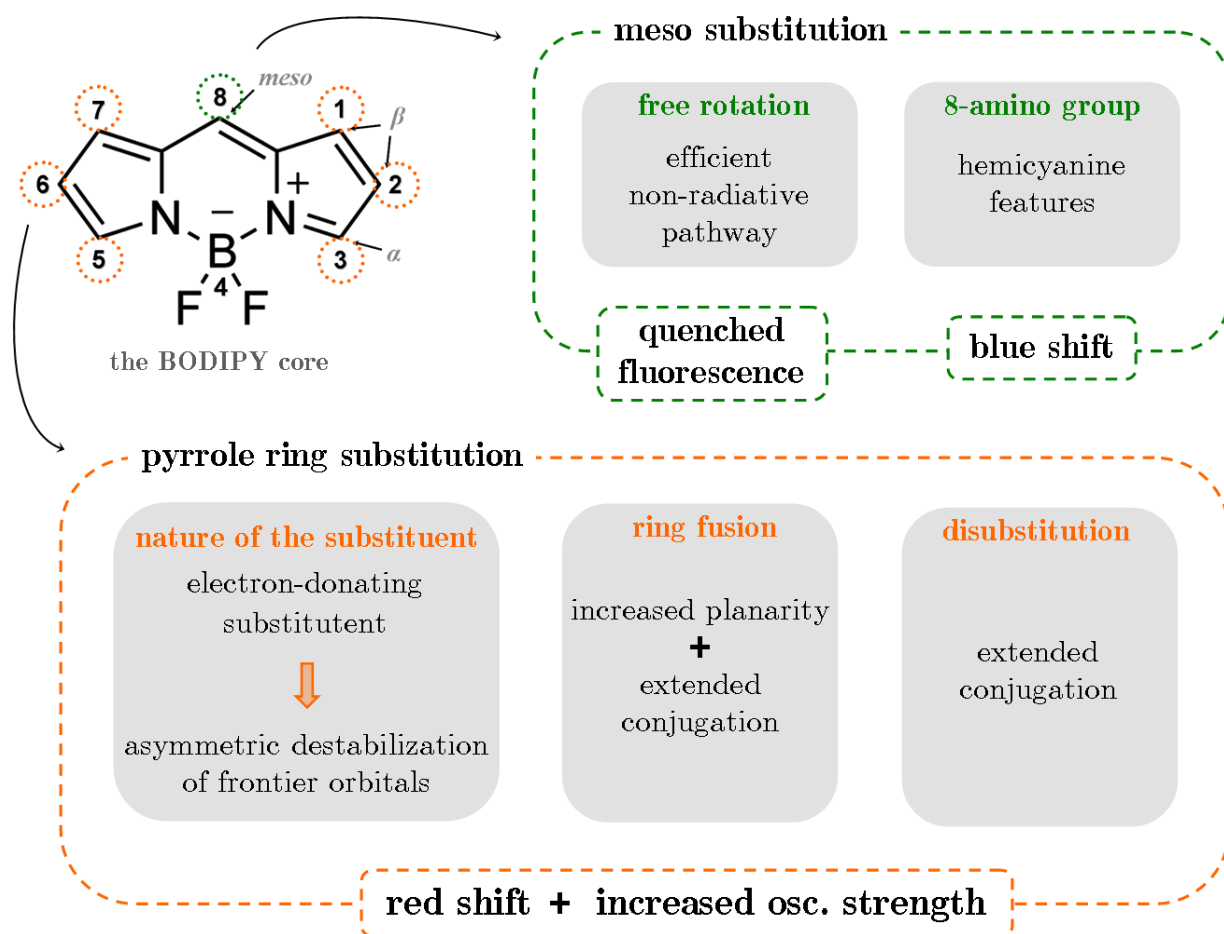

Figure 1. Structure et nomenclature IUPAC du BODIPY et principaux résultats.

Alors que les valeurs des longueurs d'onde d'absorption et d'émission se révèlent quasi-insensibles à l'introduction d'un groupement aryle en position *meso*, une telle substitution peut en revanche conduire à un important changement du rendement quantique de fluorescence puisqu'elle offre une voie de désexcitation non-radiative efficace via la rotation permise de ce substituant. La restriction de ce degré de liberté par l'introduction de groupes stériquement encombrés permet alors de restaurer la fluorescence. Fonctionnaliser le BODIPY en position *meso* de manière appropriée est l'une des stratégies employées par exemple dans l'élaboration de senseurs chimiques basés sur des processus d'oxydation ou de réduction (ou senseurs PET - Photoinduced Electron Transfer). Cette position 8 présente aussi un grand intérêt en terme de modulation des longueurs d'onde d'absorption et d'émission: ces dernières peuvent en effet être déplacées vers le bleu par l'introduction de groupements amino. L'autre partie du spectre peut être explorée par des modifications structurales aux positions de substitution présentes sur les cycles pyrroles. Ainsi, en fonction de la nature des substituants, de la symétrie de la substitution, ou encore de la possible rigidification de la molécule, nous avons montré que d'importants déplacements spectraux vers les grandes longueurs d'onde peuvent être obtenus, accompagnés d'une augmentation de la force d'oscillateur.

2. Étude conjointe expérimentale et théorique de chromoionophores pour la détection de cations Zn^{2+}.

Parmi les multiples chromophores disponibles, les pérylènes sont d'intéressantes plateformes de départ pour l'élaboration de nouveaux senseurs moléculaires de part leurs remarquables propriétés photochimiques pouvant être largement modulées grâce aux multiples fonctionnalisations possibles. Le senseur d'ions zinc objet de notre étude, constitué d'un pérylène monoimide (PMI) couplé à une unité dipicolylamine (DPA), possède une architecture de type donneur-accepteur. Nous avons montré par nos calculs que le déplacement spectral du maximum d'absorption vers le bleu, mesuré en solution lors d'ajout d'ion Zn^{2+}, s'expliquait par l'impact du cation sur le transfert de charge intramoléculaire ayant lieu dans le composé libre après photo-excitation. La formation du complexe s'accompagne d'une stabilisation asymétrique des orbitales frontières principalement impliquées dans la transition électronique d'intérêt. Plus

spécifiquement, cet effet est dû à une diminution du caractère donneur de l'azote de l'unité DPA, sa paire libre étant impliquée dans la complexation du cation, contribuant à l'altération du transfert de charge intramoléculaire (Figure 2). En d'autres termes, la réponse optique du PMI-DPA à l'ion Zn^{2+} est reliée au degré de couplage électronique entre l'unité ionophore et l'unité chromophore qui le constituent.
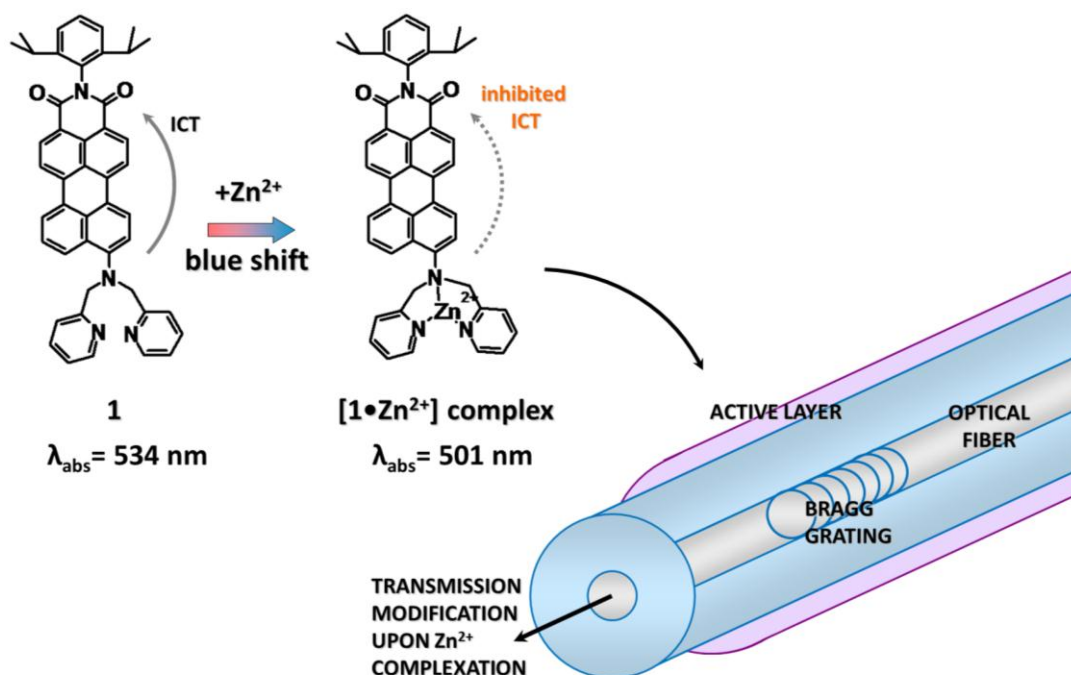
Figure 2. Structure du dérivé de pérylène monoimide senseur d'ions zinc et principe de détection par fibre optique.

Etant donné l'objectif final, à savoir l'intégration du composé dans un dispositif de détection par fibre optique, une série d'expériences a été menée pour mettre en évidence la réponse du senseur en phase solide. L'encapsulation dans un sol-gel permettant d'améliorer le temps de réponse, ce dernier a été déposé sur une fibre optique modifiée: dans ce dispositif, la présence d'ions Zn^{2+} se traduit par une modification significative du spectre de transmission de la fibre, confirmant le caractère prometteur de ce type de système pour la détection d'ions zinc.

Acknowledgements

Il me semble impossible de débuter ces remerciements autrement que par toi, Frédéric, sans qui rien de tout ceci ne serait arrivé. Sache que je ne regrette pas une seconde de t'avoir croisé sur le chemin de mon indécision chronique, je n'aurais pas pu mieux tomber. Merci pour tout.

Beaucoup de reconnaissance aussi envers tes deux "complices" dans cette affaire, Roberto et David, que je remercie avant tout pour leur confiance.

Roberto, merci pour ta bienveillance tout au long de ce travail de thèse, mais aussi pour ta rigueur (celle qui m'a parfois fait défaut), et ta disponibilité. Au delà de l'aspect scientifique, je voudrais aussi te remercier pour ta grande générosité et l'atmosphère vivante et humaine que tu privilégies au sein du groupe, et sans laquelle les choses ne seraient à mon sens pas tout à fait les mêmes.

David, merci pour ton enthousiasme et ton optimisme débordants, ton humanité, ainsi que ta disponibilité sans limites - ou presque. Malgré les quelques incompatibilités de nos langages respectifs, tes précieux conseils et ta patience m'auront plus d'une fois permis d'avancer et de m'enrichir. Tu as été pour moi un peu plus qu'un directeur de thèse, ça valait bien des pommes pour la vie.

Besides my supervisors, I would like to thank the other members of my thesis committee, the professors Jean-Luc Brédas, Toussaint Robert, Luisa de Cola and Mark Van der Auweraer, for accepting to be part of my jury and evaluate my work.

Agnès, un grand merci pour ton aide (incommensurable) bien avant que j'arrive et tout au long de ces 4 années, du logement aux méandres de l'administration, en passant par le sauvetage d'une petite boule de poil.

Naturally, I would like to thank my two first friends in Mons, without who things would not have been the same. Lucas, thank you for knocking at my door the very first evening I was facing my new life alone, and for all that followed. Mike, thank you for all that we shared, and the things you made me discover, from Praha to Abingdon, with a hint of garlic and ginger, awful mouthwash smell not included. I also would like to thank the other people of the small group that welcomed me. Juan, Cris and Sara, I share with you great memories of moments together, chatting around a beer or stuck in endless darts games, and sincerely hope it was just a beginning. Sergey, I'm sure you understand what I just meant, you were part of it.

Place enfin à ces belges, qui m'ont permis de me sentir chez moi. Bro, merci pour tous ces moments que l'on a partagé, ces carnavals et ces festivals de Dour, et ta générosité de chaque instant. Finalement, pour un type qui se la raconte dans Chemical Reviews, t'es quand même plutôt chouette. Merci aussi à ta Paupiette. Mathieu, merci pour ces longues heures à refaire le monde, d'une façon ou d'une autre, sous les oranges ou sous la lune, je n'oublierai pas. Patrick, merci de t'être suffisamment ouvert pour tolérer le petit dinosaure qui est en moi. Et plus sérieusement, Papinou, merci pour ton soutien, ta gentillesse, et tout simplement, ton amitié.

Je tiens aussi à remercier toutes les autres personnes que j'ai eu la chance de côtoyer au sein du groupe. Olivier, "crouch, touch, pause, engaged" (à l'ancienne), merci pour ça et tout le reste. Colin, pour m'avoir fait découvrir les chemins de ton enfance, à bicyclette. Max, merci pour ta patience dans ma relation tumultueuse avec la DFT, entre autres. Vincent,

Fabien, je ne pouvais réaliser quand j'étais petite la chance que c'était d'avoir cette relation exclusive avec toi, tu sais, celle qui inquiétait ceux qui nous gardaient à la maternelle. 25 ans plus tard, tu es toujours là, et je crois que j'ai compris. Merci.

Merci aussi à Cathy, ma "deuxième maman", et son Jacques.

Enfin, un grand merci à ma famille, et en particulier à mes parents et ma sœur, qui m'ont toujours soutenue et encouragée.

Mamie Lulu, merci pour tes petits pots en verre au bon goût de chez moi.

Abstract

The increasing presence of various substances in our environment has brought about a growing need for rapid emergence of new materials and devices in the quest for efficient and reliable chemical sensors. Massive technological progress have made available an extensive range of technical tools to serve their development, accounting for the requirements to be fulfilled (selectivity, quick response..). In this context, quantum chemistry methods provide a fundamental understanding of the processes at stake in the detection of chemical species and allow for rational design of sensing materials. Certain organic molecules can be extensively functionalised and thus constitute an evident starting point owing to the tunability of their properties provided by appropriate choice of structural modifications. The versatility of some chromophores associated to the selectivity offered by receptor units constitute the research playground for the development of ever better chemosensors.

In this thesis, we used density functional theory (DFT) and its time-dependent extension (TD-DFT) to investigate the relationship between molecular structure and optical properties of organic chromophores featuring valuable characteristics. Furthermore, photophysics of cation detection were studied, and ion recognition demonstrated with both quantum-chemical calculations and experiments. In particular, we have worked on : (i) series of BODIPY derivatives and highlighted the conformational restriction consequences on their optical properties, that is to say bathochromic shifts of absorption and emission maxima, as well as the effects of substitution ; (ii) push-pull rylene derivatives that show a reduced intrachain charge transfer character upon binding zinc ions ; this results in a change in optical absorption and refractive index that can be probed by a sol-gel microporous layer grown on an optical fibre.

Contents

General introduction

A lthough metal ions occur naturally in our environment, intensive human activities have severely modified the original balance and the past decades have seen an increased interest among the scientific and industrial communities for the detection and the quantification of those species[i]. In spite of the essential role some of them can play in various biological processes of living organisms (e.g. the zinc ion for protein synthesis, activity of many enzymes, regulation of the cell production in the immune system of the human body or genetic expression[1]), excessive amounts of most metal ions in water, air and soil represent serious environmental and public health issues due to their potential (eco-)toxicity[2,3], which depends on their chemical form. Diverse anthropogenic sources may be identified, as corrosion, industrial effluents or gold mining wastes, and dramatic concentrations can be reached as a consequence of their accumulation over the years. A wide number of analytical approaches are currently available for the detection of cations, such as atomic absorption spectrometry[4], but most of them entail excessive costs and/or present technical limitations (impossibility of use for on-site detection). Precise understanding of complex processes established in nature, such as the efficient detoxification mechanisms for

---

[i] in this context, they are generally incorrectly referred to as "heavy metals", see IUPAC Technical Report, J. H. Duffus, *Pure Appl. Chem.* **74**, 793 (2002).

the regulation of metal ions, provides a rich source of inspiration for the elaboration of abiotic chemical sensors, or chemosensors. Rational design of systems fulfilling accurate metal ion detection requirements via the achievement of desired properties and functions, from molecular and supramolecular chemistry principles, however still proves to be a challenging task.

Defined as the "chemistry beyond the molecule"[5] or "chemistry of molecular assemblies and of the intermolecular bond" by one of its main instigators J.-M. Lehn[ii], supramolecular chemistry is fundamentally based on the concepts of receptor[6], i.e. that molecules do not act if they do not bind, recognition[7] (lock and key), and coordination[8]. Molecular recognition, which has emerged as an highly active domain of chemical research, relies on the specific binding of a guest (analyte) by a given host (receptor), the event being characterised by the associated amount of energy and information brought into play[9]. Optimal recognition can then be regarded as being achieved when the free energy difference for binding of a given guest largely differs as compared to other guests.

In a molecular chemical sensor, the recognition unit, responsible for the selective binding of the metal ion, can be covalently linked, via a spacer or not, to a chromophore to build a so-called *chromoionophore* (figure below, adapted from ref 10). When designing such sensing compounds, one has to account for both moieties to achieve the expected functionalities and properties, and for the possible spacer for interactions and geometry modulations. While the *ionophore* binds the analyte, "storing" the information that for instance a metal ion is present, the

---

[ii]J.-M. Lehn was awarded the Nobel Prize in Chemistry 1987 jointly with D.J. Cram and C.J. Petersen *"for their development and use of molecules with structure-specific interactions of high selectivity"*.

chromophore translates the complexation event into an optical signal, the detection being generally based on modifications of light absorption or fluorescence.
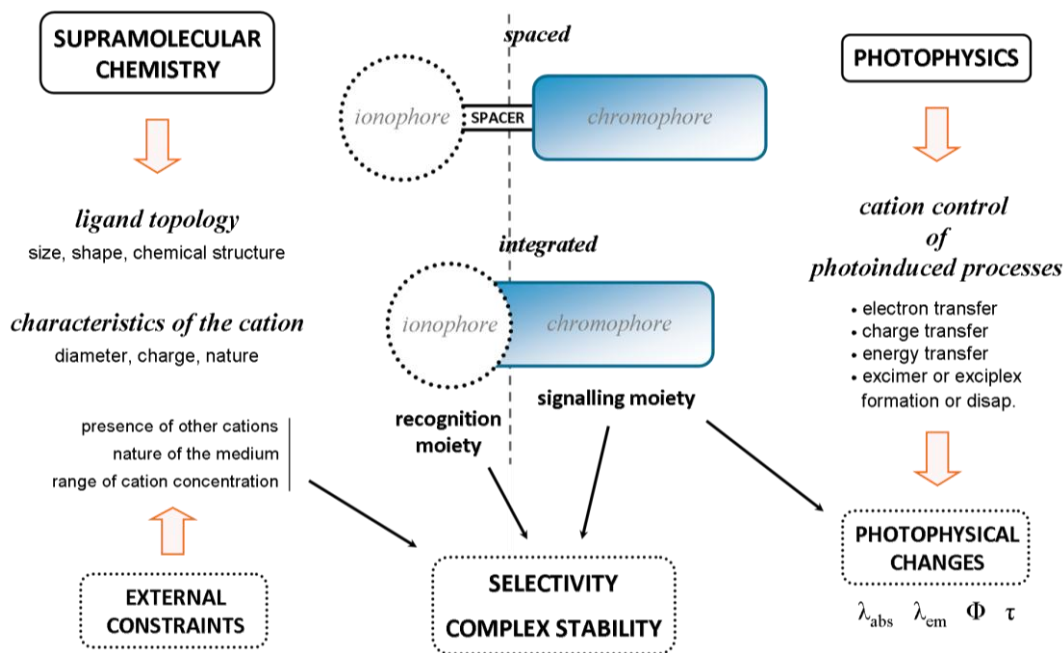
An efficient chromoionophore sensor can thus be defined as a molecule that selectively, and ideally reversibly, binds a given ion, inducing changes in the photophysical properties of the system (spectral displacement, change of quantum yields..). Such systems are inherently attractive given the multiple advantages they provide, from both their selectivity and sensitivity, to the ability of performing continuous monitoring or in situ remote sensing when combined with optical fibres[11].

The present research aims at the rational development of chromoionophores for the complexation of cations, using computational chemistry methods in combination with basic spectroscopic

characterisation. Two main aspects are treated, namely the molecular structure-optical properties relationships of the chromophore and the complexation phenomenon. More specifically, we focus on the detection of Zn^{2+}, which is the ion of interest when monitoring the corrosion of galvanised steel, and account for the future integration of the chemical sensor in an optical fibre device.

In the first chapter, a detailed introduction to the major photophysical processes that take place upon interaction of light with an organic molecule is given. In a second step, we recall the cation sensing principles on which chromoionophore design is based, and present the main photophysical changes associated to the cation complexation event. Basic concepts of quantum chemistry and computational methods employed in this work are reviewed in Chapter 2. The next chapter is dedicated to the chromophore unit, which constitutes the signalling element of our molecular chemical sensor. Four series of BODIPY dyes are studied to get insight into how their optical properties can be modulated by substitution and appropriate structural modifications. Chapter 4 reports the comprehensive study of a zinc ion molecular sensor. The perylene monoimide derivative we investigated is decorated by an appropriate ionophore and the complexation of Zn^{2+} is characterised in terms of signalling optical response by quantum chemical methods and experimental measurements. In order to demonstrate the detection of the zinc ion with optical fibre sensor technology, a series of experiments have been performed. Starting from deposition of pure films on glass substrates and the spectroscopic characterisation of the Zn^{2+} detection, the chromoionophore is then encapsulated in a sol-gel that constitute the active layer on a modified optical fibre.

References

[1]   B. L. Vallée, K. H. Falchuk, *Physiol. Rev.* **73**, 79 (1993).

[2]   G. J. Fosmire, *Am. J. Clin. Nutr.* **51**, 225 (1990).

[3]   P. C. Nagajyoti, K. D. Lee, T. V. M. Sreekanth, *Environ. Chem. Lett.* **8**, 199 (2010).

[4]   A. P. S. Gonzáles, M. A. Firmino, C. S. Nomura, F. R. P. Rocha, P.V. Oliveira, I. Gaubeur, *Anal. Chim. Acta.* **636**, 198 (2009).

[5]   J.-M. Lehn, *Angew. Chem. Int. Ed. Engl.* **27**, 89 (1988).

[6]   P. Ehrlich, *Studies on Immunity.* John Wiley and Sons, New York (1906).

[7]   E. Fischer, *Ber. Deutsch. Chem. Ges.* **27**, 2985 (1894).

[8]   A. Werner, *Zeitschr. Amorg. Chem.* **3**, 267 (1893).

[9]   J.-M. Lehn, *Struct. Bonding* **16**, 1 (1973).

[10]   B. Valeur, *Molecular Fluorescence: Principles and Applications*, Wiley-VCH (2001).

[11]   O. S. Wolfbeis, *Anal. Chem.* **76**, 3269 (2004).

Chapter 1

Photophysics of cation detection

To ensure that complexation of a metal ion yields the desired optical response, one has to efficiently tailor the optical properties of the chromophore moiety. A chromophore is defined by the IUPAC as "the part (atom or group of atoms) of a molecular entity (...) responsible for the dye's colour", this colour arising from the ability of the molecule to interact with light. To define how and to what extent optical properties can be modulated, it is of utmost importance to understand the interaction of light with a molecule and its consequences on the optical properties.

1.1   Absorption

Light is a transverse electromagnetic radiation that can be characterised by its frequency ν or wavelength λ but is also quantised in discrete packets of energy E called photons (wave-particle duality).

$$E = h\nu = \frac{hc}{\lambda} = hc\bar{\nu} \qquad (1.1)$$

with h the Planck constant, c the speed of light and $\bar{\nu}$ the wavenumber.

Depending on the wavelength of the radiation interacting with matter (Figure 1.1), different phenomena can be observed. Our work deals with the optical spectral range comprising the UV, visible and NIR regions.
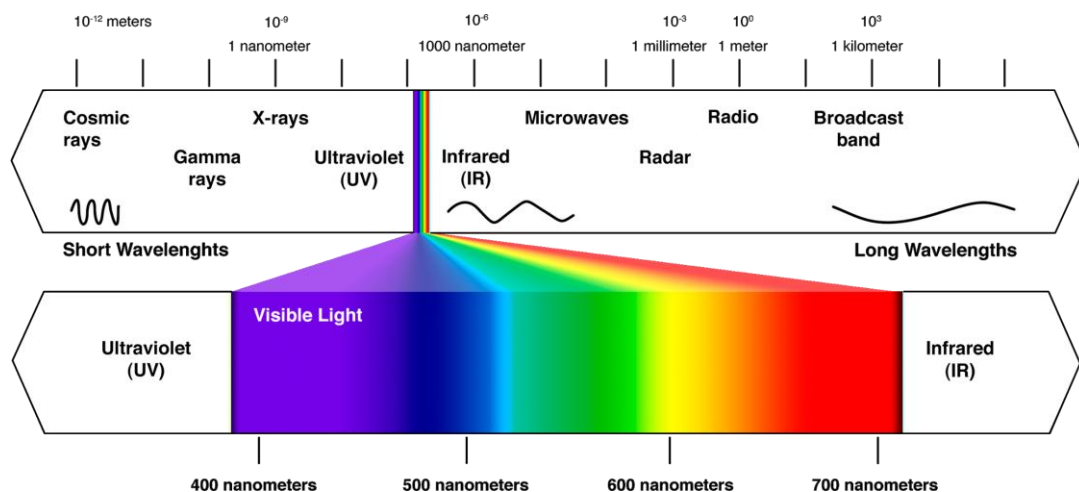
Figure 1.1 Spectrum of electromagnetic radiation.[0]

1.1.1 How does light "physically" interact with molecules ?

The typical "size" of the organic molecules we investigate is way smaller than any wavelength in this UV-Vis-NIR range, but such radiation can interact with the electrons of the molecule by its electric field component ξ (the magnetic field having only a negligible effect). The oscillating nature of the incident electric field results in the setting into motion of the electron cloud that will in turn behave as an oscillating electric dipole,

i.e. some energy has been transferred from the electromagnetic wave to the material. A pictorial description of the interaction is that as ξ passes through the molecule, its electron cloud will somehow move back and forth as a consequence of the attractive and repulsive forces it experiences as a function of time, generating a *transient dipole moment* in the molecule. When oscillations of light and electrons are synchronised at the same frequency ν, i.e. at resonance, the maximum amount of energy is exchanged, satisfying the concept of energy conservation that implies:

$$\Delta E_{molecule} = E_1 - E_2 = h\nu = E_{photon} \tag{1.2}$$

with E_1 and E_2 the respective energies of two quantised electronic states of a molecule separated by $\Delta E_{molecule}$, and ν the frequency of oscillation of light. In other words, when the frequency of the oscillating electric field (the energy of a photon) is resonant with the oscillation frequency of the electrons (the energy gap between two electronic states), *absorption* occurs, depending thus on the frequency of light but also on the electronic structure of the molecule, i.e. its energy levels. The visible region of the electromagnetic spectrum corresponds to photons spanning energies from about 1.8 to 3.1 eV, a range matching the $\Delta E_{molecule}$ of organic chromophores.

1.1.2 Electronic structure of molecules and the role of π-conjugation

The electronic structure of a molecule is described within the quantum theory by probability density functions involving eigenstates associated with discrete eigenvalues (see chapter 2). Absorption of a photon will bring the molecule from its electronic ground state to an electronic

excited state higher in energy (while light emission consists in the inverted process).

In a molecular orbital picture, atomic orbitals (AO) are combined to obtain molecular orbitals (MO), electronic wavefunctions describing the probability of finding an electron in any given region of the molecule in a certain electronic state. The electronic ground state thus corresponds to the case in which all the electrons are filling the molecular orbitals of lowest possible energy while respecting the Pauli principle. Excited states are described by a combination of transitions from occupied to unoccupied molecular orbitals, generally involving mainly the highest occupied molecular orbital (HOMO) and the lowest unoccupied molecular orbital (LUMO). Depending on the type of AOs combined, the resulting MOs can be of σ, n or π nature and different energies are associated with the possible electronic transitions between them. Contrary to the σ-MOs, which are oriented along the internuclear axis, the π-MOs lie above and below the latter, and π-electrons are consequently only loosely bound by atoms. When several atomic p-orbitals are combined along a sequence of adjacent atoms in sp^2-hybridisation, in such a way that a pattern of alternating single and multiple bonds is formed, a so-called π-conjugated system is formed in which the electrons are delocalised over the atoms of the molecule. The molecular energy levels are affected by π-conjugation: the larger the extent of conjugation, the smaller the energy gap between the frontier orbitals (Figure 1.2).
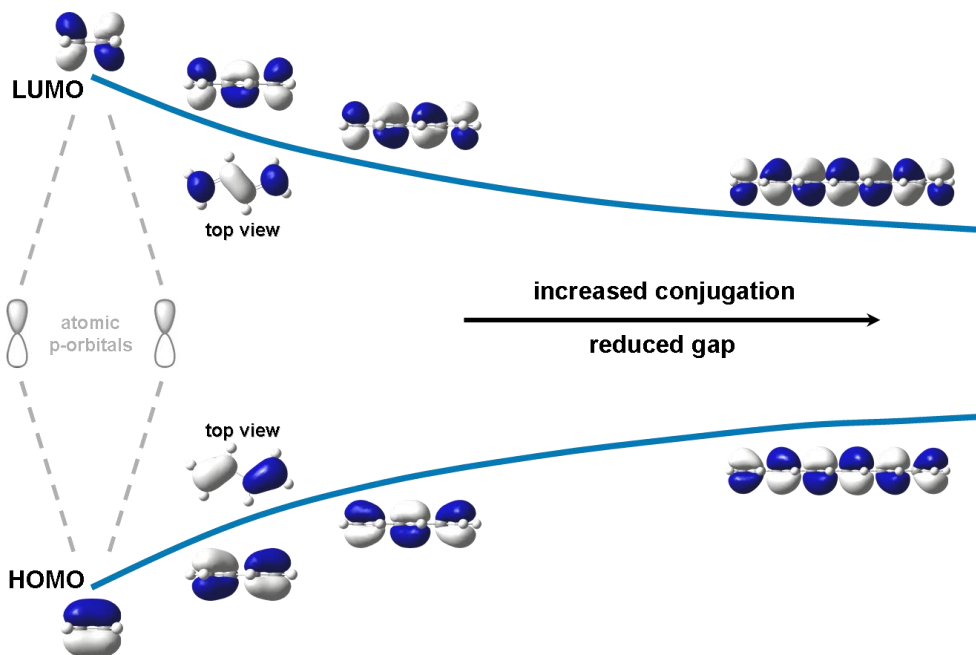
Figure 1.2 Schematic evolution of the HOMO/LUMO energy gap as a function of increased conjugation in a series of linear polyenes.

The (un)occupied MOs that matter in the determination of electronic and optical properties of an organic molecule are generally of π-type nature (less energetically stable than the deeper σ orbitals) and absorption in the near UV, visible, and NIR regions corresponds to transitions between π-electronic states.

1.1.3 Transition probability

As mentioned above, there are conditions for a transition to occur and the ability of a photon of specific energy to modify the electronic structure of the molecule will govern the probability of the transition. The changes in

charge distribution and electronic structure consequent to the interaction, i.e. the transitory moment relative to the field induced oscillation of the electron cloud, is described by the so-called transition dipole moment:

$$\mu_{ij} = \left\langle \psi_i \left| \hat{\mu} \right| \psi_j \right\rangle \tag{1.3}$$

with ψ_i and ψ_j the electronic wavefunctions of the molecule in the initial and final states, respectively, and $\hat{\mu}$ the electric dipole moment operator. For a transition to be allowed, the transition dipole moment, the magnitude of which directly determines the intensity of spectroscopic absorption/emission, should be nonzero, and symmetry selection rules can be derived (e.g. Laporte's rule for centrosymmetric molecules). The second important selection rule concerns the spin multiplicities of the initial and final states, which should be equal for the transition to be allowed. The probability of an allowed transition is proportional to the squares of μ_{ij} and electric field intensity and is thus the highest when the transition dipole moment is parallel to the polarisation vector of the oscillating electric field.

The transition dipole moment can be related to the oscillator strength f:

$$f = \left(\frac{8\pi^2 m\nu}{3he^2} \right) \mu_{ij}^2 \tag{1.4}$$

It is a dimensionless quantity which links the quantum and classical approaches and can be interestingly expressed as a function of an experimental quantity, namely the molar extinction coefficient $\varepsilon(\overline{\nu})$:

$$f = 4.3 \times 10^{-9} \int \varepsilon(\overline{\nu}) d\overline{\nu} \tag{1.5}$$

with $\int \varepsilon(\bar{\nu})d\bar{\nu}$ the area under the curve of the extinction coefficient plotted against wavenumber. A value of f of ~0 represents a forbidden transition, while a value close to unity indicates a strong transition.

Having discussed the types, probability and intensity of transitions, we can finally consider the shape of an absorption spectrum, which will depend both on the vibrational sublevels of the molecular states and on the interaction with the surrounding medium (see section 1.3), causing homogeneous and inhomogeneous broadening.

Absorption of a photon not only results in a 'pure' electronic transition since the molecule also acquires some extra vibrational energy giving rise to a vibrational structure in the absorption band. The intensities of the vibronic transitions (simultaneous electronic and vibrational excitation) are described by the Franck-Condon principle, based on the premise that electrons are so much lighter than the nuclei that they respond to the excitation instantaneously compared to the time scale of nuclear motion (in analogy to the Born-Oppenheimer approximation, presented section 2.2). It states that an electronic transition is most likely to occur without changes in the positions of the nuclei in the molecular entity and its environment. The resulting state is called a Franck-Condon state, and the transition achieved, a vertical transition. The quantum chemical formulation of this principle is that the intensity of a vibronic transition is proportional to the square of the overlap integral between the vibrational wavefunctions of the two states that are involved in the transition.[1]

In other words, one can invoke the Franck-Condon principle to separate the transition dipole moment in equation 1.3 into electronic and nuclear terms:

$$
\begin{aligned}
\mu_{ij} &= \left\langle \psi_i^{tot} \left| \hat{\mu} \right| \psi_j^{tot} \right\rangle \\
&= \left\langle \psi_i^{el}, \nu_i \left| \hat{\mu} \right| \psi_j^{el}, \nu_j \right\rangle \\
&= \left\langle \nu_i \left| \nu_j \right\rangle \left\langle \psi_i^{el} \left| \hat{\mu} \right| \psi_j^{el} \right\rangle \right.
\end{aligned}
\tag{1.6}
$$

The probability of any transition thus depends on the electronic transition dipole moment times the square of the vibrational overlap integral (or Franck-Condon integral) that determines the relative intensity of each peak, known as the Franck-Condon factor:

$$
FC_{\nu_i \nu_j} = \left| \left\langle \nu_i \left| \nu_j \right\rangle \right|^2 \right.
\tag{1.7}
$$

Franck-Condon factors are governed by the relative positions of the ground-state and excited-state potential energy surfaces. This is illustrated in Figure 1.3 where two particular cases are depicted: namely, when equilibrium nuclear coordinates are the same in both S_0 and S_1 states, as opposite to the situation in which there is an offset in position of the excited state equilibrium geometry relative to the ground state.
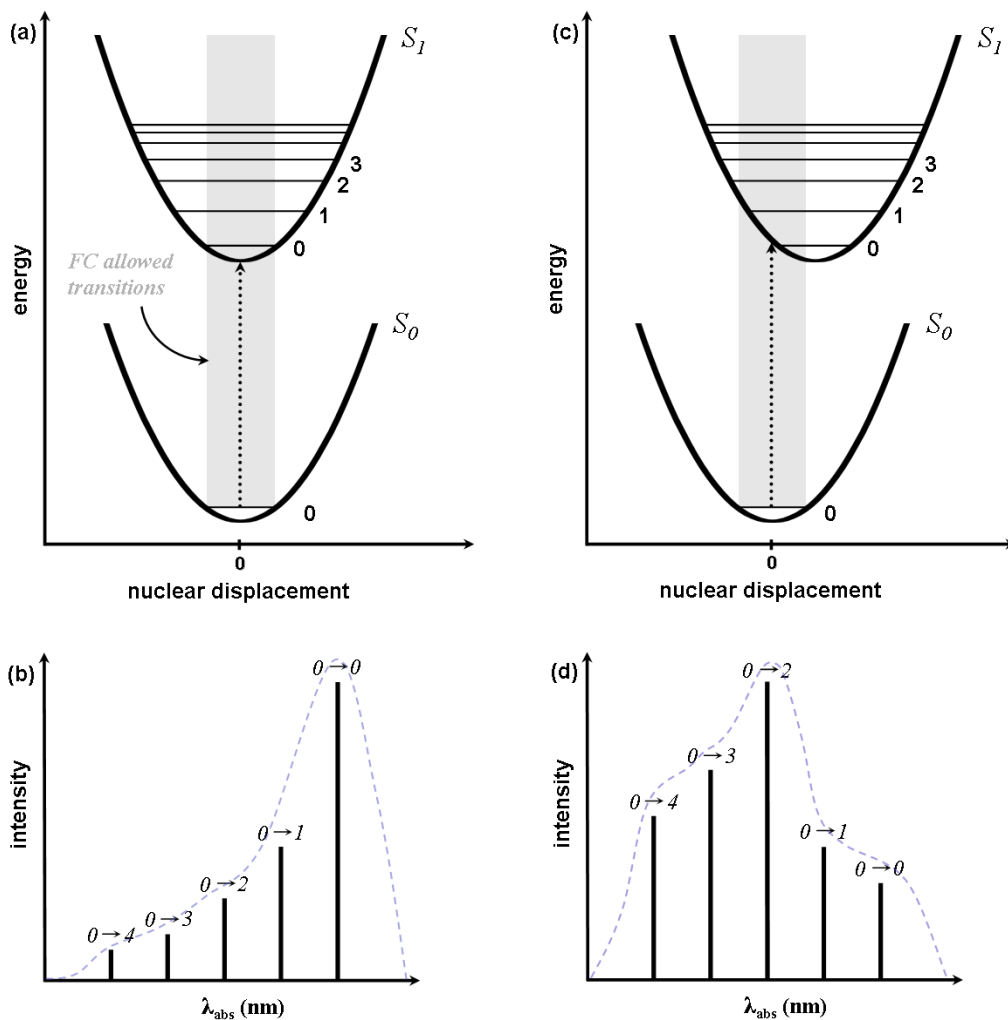
Figure 1.3 (a) and (c) depict the potential energy surfaces of two different molecules in the ground (S_0) and excited (S_1) states. (b) and (d) present the associated vibrational transitions probabilities and possible resulting shape of the absorption spectra, broadened by solvent effects (dashed curves).

In a molecule having similar equilibrium geometries in the S_0 and S_1 states (Figure 1.3 a and b), the ground-to-excited state electronic transition is not inducing vibrations and the largest overlap is found between the vibrational ground states $v_{S_0} = 0$ and $v_{S_1} = 0$. As a consequence, the 0→0 transition has the largest probability and the absorption spectrum presents a dominant band corresponding to this transition (Franck-Condon factor of unity). In a molecule where the equilibrium positions of the nuclei are displaced in the excited state (Figure 1.3 c and d), i.e. the S_1 potential curve is shifted relative to S_0 as a consequence of a significant geometry relaxation, the most likely transition is the $v_{S_0} = 0 \to v_{S_1} = 2$ one, as it corresponds to the transition for which the overlap between ν_i and ν_j is maximal (largest Franck-Condon factor), giving rise to a very different shape for the absorption spectrum.

1.2 Dynamics of the excited state

1.2.1 De-excitation pathways

Excitation from the ground state to an excited singlet state by absorption of a photon is a very fast process, occurring on the order of 10^{-15} seconds, which brings the molecule in one of the upper vibrational levels of the latter state. Once excited, the deactivation, either radiative or non-radiative, can take 10^{-14} to some seconds, and several pathways with varying probabilities are available for the molecule to dissipate the excitation energy and return to the ground state, such as fluorescence emission, internal conversion (IC), intersystem crossing (ISC) or phosphorescence.

Prior to any of the aforementioned processes, the excited molecule finds itself in a nonequilibrium state and undergoes quick *vibrational relaxation*

$(10^{-14}-10^{-11}$ seconds) down to the lowest vibrational level of the electronic state it reached, called a vibrationally-relaxed state. If initially a higher excited state $(S_2, S_3 ... S_n)$ is reached, a fast *internal conversion* (timescale of vibrational relaxation) into the lowest excited state S_1 takes place owing to the overlap existing between vibrational levels of excited states, also called horizontal transition[i]. Note that molecules with a high degree of rigidity are less likely to undergo internal conversion. From S_1 to the ground state, it is however an inefficient and very slow process due to large energy gap between the two states and other competing events might happen first. These vibrational relaxation and internal conversion processes are non-radiative (the excess energy is dissipated as heat) and when combined, they result in the molecule being in the lowest vibrational level of the first excited singlet state S_1. This is the basis of Kasha's rule, which states that "the emitting level of a given multiplicity is the lowest excited level of that multiplicity".[2] A corollary, known as the Kasha-Vavilov rule, says that the quantum yield of luminescence is independent of the wavelength of the exciting radiation. Both rules have exceptions.[3]

---

[i] When there is a small gap, i.e. no overlap, a tunnelling process takes place, with a probability governed by the difference in energy between the lower and upper vibrational levels of the initial and final electronic states, respectively.
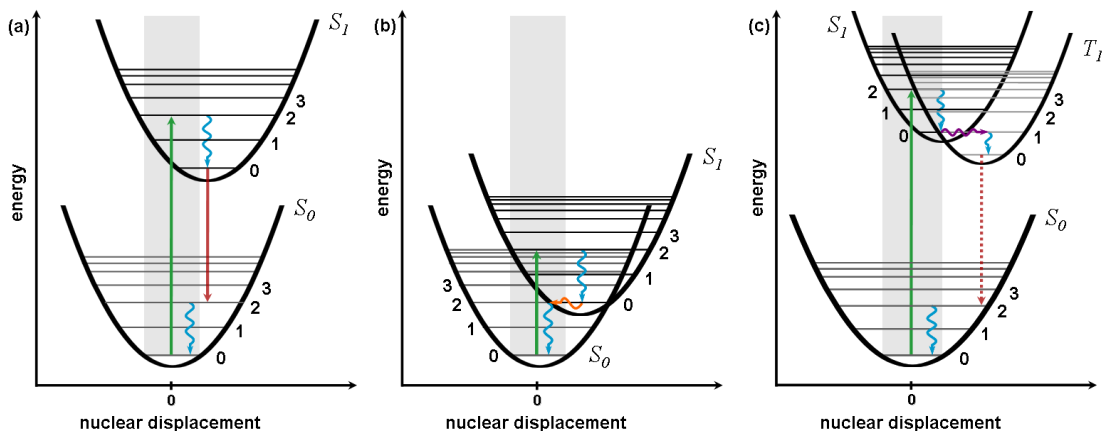
Figure 1.4 (a) fluorescence, (b) non-radiative deactivation via S_1-S_0 internal conversion, (c) intersystem crossing (triplet state formation) and subsequent phosphorescence emission.

From the zero[th] vibrational level of the first excited singlet state, the molecule can return to the ground state via photoluminescence. One can distinguish two radiative decay channels that depend on the multiplicity of the electronic states involved in the emission process.

When S_1 and S_0 have the same multiplicity, the spontaneous emission of a photon with an energy equal to the gap between the two states is called *fluorescence* (Figure 1.4 a). Just as for the absorption process previously described, the probability for a transition is proportional to the transition dipole moment associated and the emitted light is polarised parallel to it. As the Franck-Condon principle also applies for fluorescence, the vertical transition from the lowest vibrational level of S_1 leaves the molecule in excited vibrational levels of the ground state, the intensity of the vibronic transitions being proportional to the square of the overlap integral between the vibrational wavefunctions. Ultimately, vibrational relaxation occurs to let the molecule relax to the zero[th] vibrational level of the ground state. Clearly, as a consequence of the energy dissipation

subsequent to the absorption of light (vibrational relaxation in S_1) as well as the second relaxation occurring in the ground state, the emitted photon has less energy than the absorbed photon and the fluorescence spectrum is shifted to longer wavelengths. This phenomenon is referred to as the Stokes shift, which is defined as the difference between the 0-0 transition of the absorption and emission bands. Fluorescence emission takes place from the equilibrium distribution of vibrational level of S_1 to different vibrational levels of S_0 and, when the shapes of the potential curves are similar for both states with comparable vibrational features, the same transitions are favoured, resulting in a fluorescence spectrum that is a mirror image of the $S_0 \rightarrow S_1$ absorption, with a common transition between the lowest vibrational level of both electronic states ideally overlapping. However, charge redistribution in the excited state as well as interactions with solvent molecules generally affect the overall mirror image symmetry shape. As the energy gap between the ground state and the first singlet excited state decreases, the efficiency of the internal conversion process increases proportionally and fluorescence is less likely to be the dominant deactivation pathway (Figure 1.4 b).

Phosphorescence is the second radiative de-excitation that can take place, initiated via a radiationless process known as *intersystem crossing* (Figure 1.4 c). The crucial difference with all pathways already described is that it involves the formation of a triplet state and hence concerns states of different multiplicities, i.e. transitions of the $S_n \rightarrow T_n$ or $T_n \rightarrow S_n$ types. The probability for such S_n-T_n transition increases with the overlap of vibrational levels of the singlet and triplet excited states (for instance $v_{S_1} = 0$ and higher vibrational levels of T_1). However, unlike internal conversion, intersystem crossing requires a spin conversion, which is in principle forbidden, but can nevertheless take place due to spin-orbit coupling giving rise to weakly allowed transition. A quick vibrational

relaxation follows and leaves the molecule in a vibrationally-relaxed triplet state. Although intersystem crossing is a slow process compared to the similar internal conversion, it is able to compete with and dominate fluorescence in some cases, like in molecules containing heavy atoms, because of a more efficient spin-orbit coupling.

From the lowest vibrational level of the triplet state T_1, the molecule can end up in the ground state S_0 by a second intersystem crossing but it can also, depending on the conditions, lose its energy via phosphorescence emission, both processes involving a change in the spin multiplicity and thus exhibiting low probability. Similarly to fluorescence, phosphorescence consists of transitions to vibrational levels of the ground state by emission of a photon and the spectrum is often a mirror image of the ground state absorption. However, as it is characterised by a forbidden spin conversion, it occurs on such long time-scale (10^{-3}-10^2 seconds) that it is not so commonly observed, as other deactivation processes might compete and become dominant. Finally, due to the lower energy of the zero[th] vibrational level of the triplet state compared to that of S_1, the phosphorescence spectrum is shifted from the fluorescence spectrum towards longer wavelengths.

Note that when the energy gap between S_1 and a long-lifetime T_1 is small, *delayed fluorescence* can also occur, which consists in a reverse intersystem crossing to S_1 followed by fluorescence emission (thermal activation or triplet-triplet annihilation).

A very convenient way to summarise all the different excitation/de-excitation pathways is provided by the Perrin-Jablonski diagram (Figure 1.5).
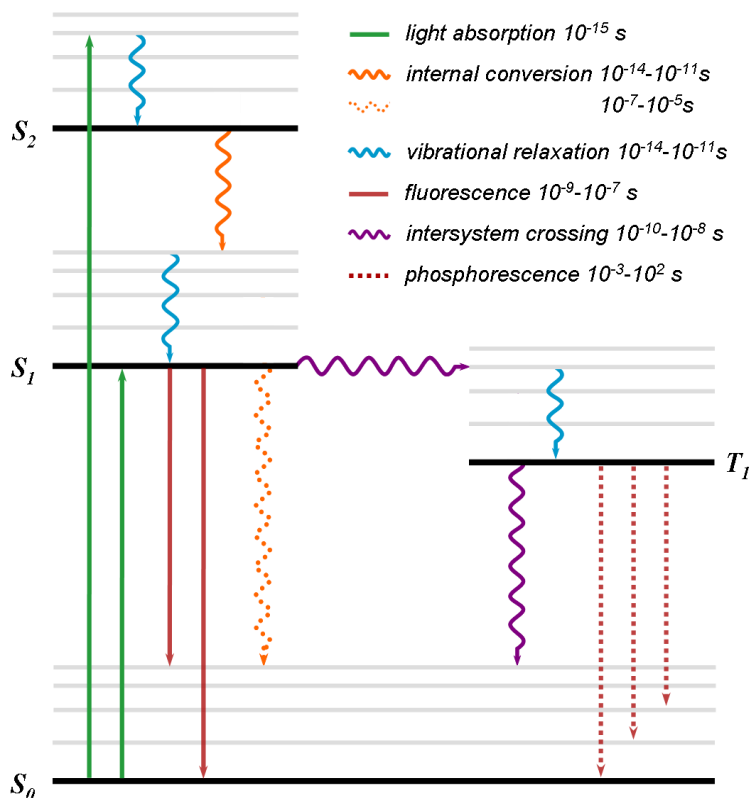
Figure 1.5 Perrin-Jablonski diagram of an organic molecule and characteristic lifetimes.

By convention, the various optical processes that can occur are depicted by arrows between electronic states and their respective vibrational levels, wavy arrows being associated with non-radiative events.

1.2.2 Decay characteristics

While the molar extinction coefficient ε reflects the ability of a molecule to absorb light at a certain wavelength, the efficiency of a given deactivation process can be estimated by its quantum yield $\Phi_{process}$, which is the ratio of quanta absorbed to the number of quanta that undergo

that process. It can also be expressed as a function of the relative excited state decay rates:

$$\Phi_{process} = \frac{k_{process}}{k_{process} + \sum k_{deact}}$$

(1.8)

where $\sum k_{deact}$ is the sum of the rate constants for all the deactivation processes that compete with the process of interest, to which $k_{process}$ is the associated rate constant.

Clearly, the fluorescence quantum yield decreases as the number of possible efficient deactivation pathways increases. For instance, the fluorescence quantum yield, given by the ratio of photons emitted to photons absorbed, can be calculated by:

$$\Phi_{fluo} = \frac{k_{fluo}}{k_{fluo} + k_{IC} + k_{ISC}}$$

(1.9)

As already mentioned, the extent of conjugation, reflected in the electronic structure of the molecule, constitutes a key parameter defining the absorption and emission spectra properties: the longer the π-conjugated system, the longer the wavelength of the absorption maximum. As for the geometrical constraints, fluorescence emission is favoured in molecules that exhibit a rather rigid structure, as they are less likely to undergo radiationless deactivation due to vibrational and rotational dynamics. However, not only the chemical and molecular structures are determining the nature and efficiency of the various de-excitation processes, many environmental parameters also come into play, such as the temperature, as the efficiency of thermal agitation-related non-radiative processes increases with it, or what usually receives the most attention, the solvent effects, known to greatly condition the photophysical properties of a molecule.

1.3   Solvent effects

Responsible for the inhomogeneous broadening of spectral bands, solvents can strongly affect the intensity and position of absorption and emission bands and thus constitute one origin of the Stokes shift.[4] Following the absorption of a photon, vibrational relaxation towards the zero[th] vibrational level of the excited state is accompanied by solvent relaxation. The excitation of the molecule brings about changes in the ground state charge density and results in a different dipole moment in the excited state, $\mu_{S_0} \neq \mu_{S_1}$, inducing a rearrangement of the surrounding solvent molecules that reorient to stabilise S_1, then known as thermally-relaxed excited state (the dynamical aspects of solvation are described in section 2.9.2 of Chapter 2). The extent of this stabilisation depends on the polarity of the solvent (Figure 1.6): assuming $\mu_{S_0} < \mu_{S_1}$, an increasing solvent polarity causes larger stabilisation of the excited state, so that the transition band experiences an increasing *bathochromic* shift (or red-shift). Conversely, when going from a more polar solvent to a less polar one, the band undergoes an *hypsochromic* shift (or blue-shift) ; this spectral dependence on the solvent polarity for a given molecule is called solvatochromism. Opposite behaviour is observed when $\mu_{S_0} > \mu_{S_1}$, or in the case of n-π transitions. Note that the intensity can also be affected and one talks about *hyper-* or *hypochromic* shifts for an increase or a decrease in the molar extinction coefficient, respectively. These spectral changes are evidently also determined by the polarity of the solute: while polar molecules are logically very sensitive to solvent polarity, apolar molecules exhibit a modest dependency. The absorption phenomenon happening on a very short timescale ($\sim 10^{-15}$ s), it is not much affected by the solvent polarity. For the excited state, solvent relaxation can occur (timescale 10^{-10} s), before fluorescence takes place.
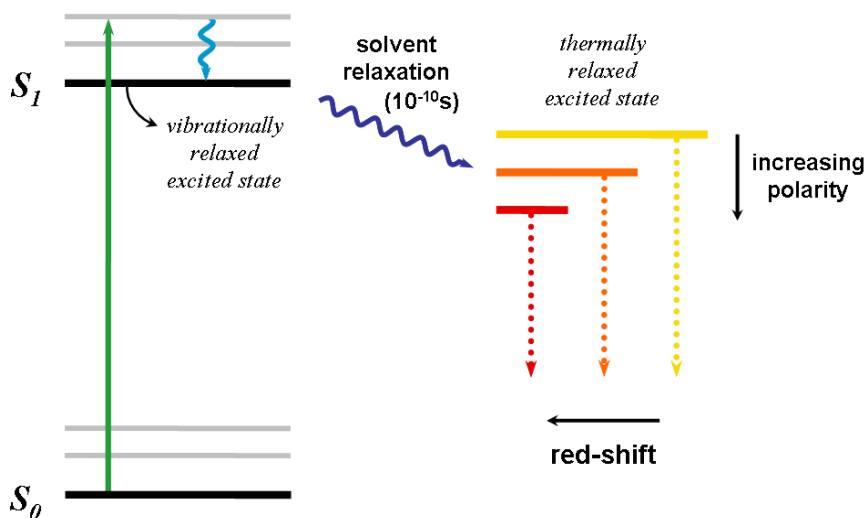
Figure 1.6 Perrin-Jablonski diagram of an organic molecule including the effect of solvent relaxation.

Solvents are roughly classified as polar or non-polar, the former being further subdivided into protic or aprotic. However, solvent polarity with related spectral shifts is a tricky concept encompassing nonspecific and specific solute-solvent interactions (inter- and intramolecular processes such as hydrogen bonding or charge-transfer..), and many alternatives to its primary expression in terms of dielectric constant have been proposed, leading to a large variety of "solvent polarity scales".[5] Among polar solvents, one can find water but also methanol or acetonitrile, while chloroform and toluene are considered as apolar. A protic solvent, or protogenic solvent, as preferentially defined by the IUPAC, is "capable of acting as a proton donor", as well as making specific hydrogen bonding.

1.4   Cation sensing principles

Chemical sensors have been developed to detect and monitor an extensive set of species and properties, ranging from ions to biochemical molecules and gases, as well as temperature or conductivity. Following the "recognition event", a sensor returns information by means of various transduction mechanisms, such as for instance, a modification of the optical properties (spectroscopic features, refractive index..) or the redox potential. The ever-growing interest that sensors have raised over the past decades has led to a jungle of compounds and devices based on various operative principles, and we refer the interested reader to several books and reviews that can provide a clear and detailed understanding of a given related issue.[6-9]

One has to be cautious while employing the term "chemical sensors", which according to the so-called "Cambridge definition"[10] are *miniaturized analytical devices that can deliver real-time and on-line information on the presence of specific compounds or ions in complex samples.* Clearly, we are not addressing fully the wide topic of chemical sensors which is beyond the scope of this manuscript but restrict our attention to optical chemical sensors, and more particularly chromogenic and fluorescent molecular sensor elements that allow for cation detection based on absorbance or luminescence of chromoionophores, respectively. Although from now on, we might use the term "sensor" in this manuscript to refer to the systems we are dealing with, it is however important to realise and keep in mind that there is a long way to go from the molecular design of an active compound to a functional final device.

1.4.1 Architecture of the chromoionophore

The classical design of a chromoionophore relies on the coupling of a receptor, achieving the recognition of the analyte with ideally the highest possible selectivity, to a chromophore acting as a transducer, whose changes in optical properties constitute the signalling of the recognition event. A spacer may provide further possibilities for modulation of the processes inherent to the detection of a given analyte (Figure 1.7). Great care has to be taken regarding each of these elements and their association, according to the principles of supramolecular chemistry.
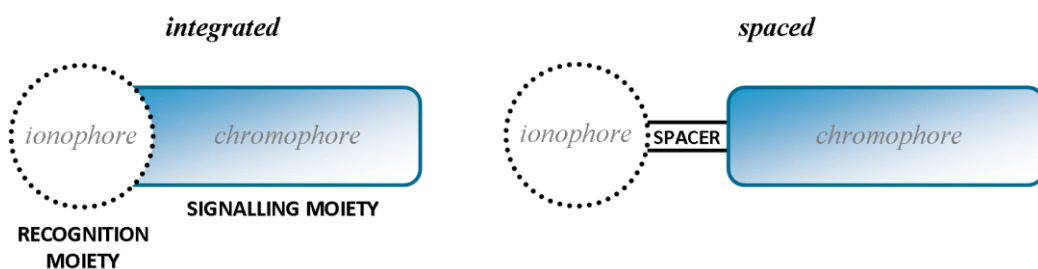
Figure 1.7 Schematic representations of the *spaced* and *integrated* architectures of a molecular sensor for cations. Note that in the integrated system, some atoms or the chromophore may participate into the complexation event.

1.4.1.1 Ionophore - Stability and selectivity

The ionophore moiety constitutes the key component of the sensor, governing its selective response to a particular analyte without interferences with other species. The preferential complexation of a given cation can be discussed in terms of thermodynamic stability constants of the complex, also known as the binding constant K_b, or its inverse, the dissociation constant K_d. These equilibrium constants can depend on

various environmental factors such as the temperature, the pH or the nature of the solvent.

Considering a 1:1 complex formation, one can write the complexation equation and associated equilibrium constants as:

$$ligand + cation \underset{K_d}{\overset{K_b}{\rightleftharpoons}} ligand \cdot cation$$
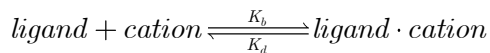
$$K_b = \frac{ligand \cdot cation}{ligand \ * \ cation} , K_d = \frac{1}{K_b}$$

The larger the binding constant, the larger the concentration of complexed cation. However, if high values for K_b (or small for K_d) reflecting more stable complexes are usually sought, selectivity, i.e. the relative affinity of a given ligand with one metal cation among other analytes, is defined as the ratio between the associated binding constants, not their absolute magnitude.

Many examples can be found in nature, which elegantly manages optimal complexation of metal ions for diverse purposes, such as biological ion transport and regulation.[11,12] However, to achieve with synthetic ionophores strong selectivity towards a given cation is a complicated task, as the interactions involved are ruled by the physical and electronic complementarity between ligand and cation: the ionophore structure (size, pre-organisation..) and the number and nature of the binding atom(s) should fit the cation characteristics (diameter, charge density, coordination number). The ionophore can be a simple chelator or possess a more complex architecture from macrocycles like crown ethers[13], to macrobicycles (cryptands)[14], or calixarene derivatives[15], to provide for example three-dimensional encapsulation, thus allowing more stable complexation. Crown ethers are particularly suitable for complexation of alkali metal cations, with selectivity depending on the size of the cavity

relative to the cation radius. Typical examples are the 18-crown-6 and dibenzo-18-crown-6, the first crown ethers synthesized by Pedersen[16], which present the strongest affinity for potassium cations among alkali metal cations (Figure 1.8).

18-crown-6   **dibenzo-18-crown-6**
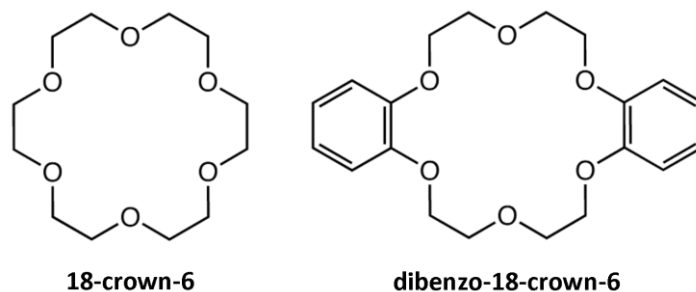
Figure 1.8 Structures of 18-crown-6 and dibenzo-18-crown-6.

Ionophores have also been developed for the complexation of transition metal cations such as the bis(2-pyridylmethyl)amine chelator presented in Figure 1.9, or more commonly dipicolylamine (DPA), first reported by Kabzinska in 1964[17]. It contains three nitrogen atoms that can strongly bind Zn^{2+} and has become very popular in the field of chemical sensors. Moreover, the availability of the nitrogen lone pair in the guest-free DPA allows for electronic processes with an appended chromophore and thus makes it a very appealing receptor subunit for the design of a zinc ion sensor.
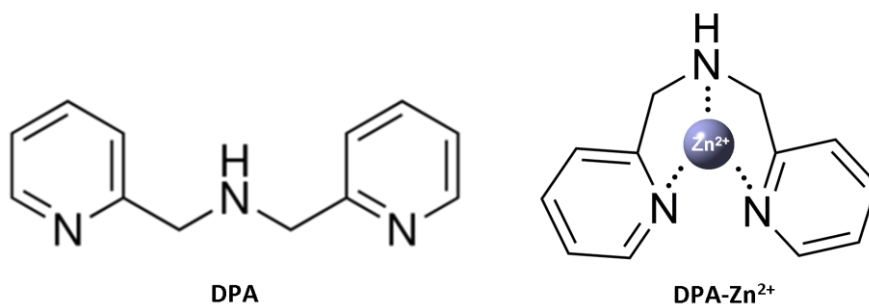
Figure 1.9 Structures of the guest-free DPA ligand and its complex with the zinc ion.

Denticity is defined by the number of binding atoms and a complex is referred to as monodentate when only one atom intervenes in the complexation, or multidentate when two or more atoms coordinate the ion (bidentate, tridentate, and so on). Note that for integrated-like architectures, the selectivity will not only depend on the ionophore but might involve the whole system. Finally, solvent effects are of major importance regarding both selectivity and stability. The rational design and development of ionophores are out of the scope of this work and the reader may find more information in the reviews, publications or textbooks that cover the topic.[18-20]

1.4.1.2 Chromophore and spacer

The properties of the signalling unit are ruled by the type of detection process selected and the kind of final device desired, so that the choice of the chromophore depends on many parameters. It is generally of utmost interest to work with tuneable compounds to obtain high molar extinction coefficients and quantum yields of fluorescence as a function of the nature and position of the substituent groups, and by extension a modulation of all properties to achieve a given photoinduced process upon complexation.

Ideally, the change in photophysical properties should be the largest possible to facilitate the detection. Moreover, the ease for substitution can allow the addition of anchoring groups, when for instance the chromoionophore has to be grafted directly on a substrate, and is also the key to modify the compound solubility. Finally, certain families of chromophores, like the rylene and BODIPY derivatives presented in section 1.4.3, allow for spanning a wide portion of the UV-Vis-NIR region and one can extensively change the wavelength working range of the sensor according to the needs; for instance, implementation on an optic fibre requires the ability for the chromoionophore to work at wavelengths for which the losses of transmitted signal are minimised (see chapter 4).[21] Further modulation can also be achieved with the inclusion of a spacer, which depending on its nature and its length[22], can greatly affect the electronic processes at stake in the detection event.

From the optimised selectivity of the ionophore moiety to the adapted photophysical properties of the chromophore, each part plays a crucial role in the detection process and rather than strictly being concerned by the design of one or more of them, we mainly focused our attention on their rational combination and the description of the cation-induced processes associated with the photophysical changes, in particular the photoinduced intramolecular charge transfer and photoinduced electron transfer.

1.4.2   Photophysical processes involved in cation detection[23-26]

1.4.2.1   Photoinduced intramolecular charge transfer (ICT)

ICT systems typically possess an integrated-like architecture, in which the receptor is conjugatively coupled to the chromophore without inclusion of

any spacer, and exhibit push-pull character arising from the nature of the terminal parts, one end being electron-donating (often an amino group), the other end being electron-withdrawing. Upon photoexcitation, the electron density is redistributed as the compound experiences an intramolecular charge transfer from the donor to the acceptor, which results in a significant change of the molecular dipole moment. It is expected that the presence and interaction of a metal cation with either the donor or acceptor site will modify the photophysical properties of the sensor, and thus by extension alter the intramolecular charge transfer subsequent to photoexcitation, inducing a displacement in both absorption and fluorescence spectra that constitutes the cation recognition transducer signal. One can modulate the strength of the ICT by substitution with more or less strong donor and acceptor groups, and thus the expected spectral shifts in the presence and absence of the analyte.
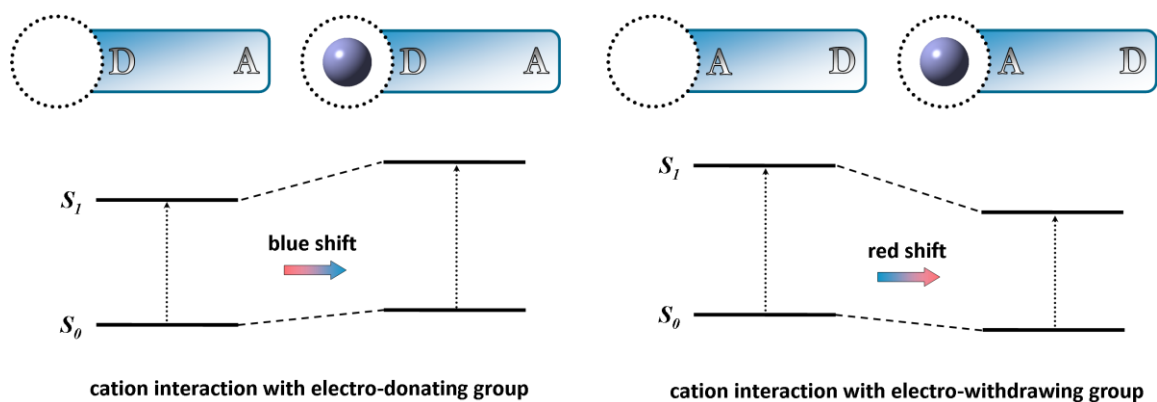
Figure 1.10 Spectral shifts arising from photoinduced charge transfer for cation interaction either with the donor or acceptor moiety of the sensor.

When the donor moiety of the chromoionophore interacts with a cation, its electro-donating character is reduced (since its electrons are involved in the binding), so that a blue-shift of the absorption spectrum relative to that of the cation-free compound is observed, accompanied by a lower molar extinction coefficient. The opposite behaviour, i.e. a bathochromic shift and an increase of $\varepsilon(\bar{\nu})$, is expected following the interaction with the acceptor, as its electro-withdrawing capacity will be enhanced and the push-pull effect strengthened. These effects can be illustrated by the evolution of the frontier orbitals, usually preponderantly involved in the transition of interest, as a function of the strength of the donor and acceptor parts of the system.[27]

Another rationalisation of the spectral displacements aforementioned is given by considering the state dipoles in the presence and absence of the cation. As previously noted, the initial electronic polarisation in the donor-acceptor system becomes larger upon photoexcitation: the electron density reorganisation leads to a substantial increase of the molecular dipole moment on going from S_0 to S_1. The interaction of a cation with the donor group causes an asymmetric destabilisation of the two states, with a stronger effect in the excited state due to the repulsive interaction with the positively charged donor in the charge transfer excited state, resulting in an hypsochromic shift. An inverse spectral behaviour is observed when the interaction takes place on the acceptor moiety as the excited state is more stabilised with respect to the ground state (Figure 1.10). Emission spectra generally experience the same kind of spectral displacements. However, not only the transition wavelengths are affected by the cation complexation, but also the quantum yield and lifetimes may change.

Finally, the ICT process is by nature clearly very sensitive to the solvent polarity (see section 1.3), and solvent effects may even favor the appearance of a twisted intramolecular charge transfer (TICT), in which

the donor and acceptor components of the push-pull system are rotated in the excited state, leading to the observation of extra-emission bands.[28]

The concept of photoinduced intramolecular charge transfer has been widely used in the design of cation sensors and numerous examples are reported in the literature.[29-33] For instance, the aza-crown based sensor from W. Qin and al. has proven to be sensitive to several metal cations, displaying large spectroscopic changes upon complexation as a result of an altered intramolecular charge transfer in the complexed form (Figure 1.11).[34]
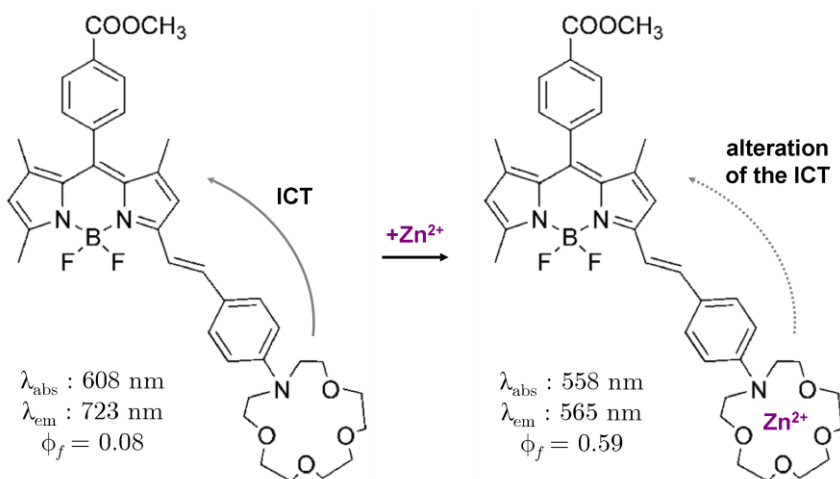
Figure 1.11 Working principle of the aza-crown ether based sensor from ref. 34.

1.4.2.2 Photoinduced electron transfer (PET)[35,36]

Photoinduced electron transfer requires an electron donor and an electron acceptor components and is based on the enhancement of the redox properties of a molecule upon absorption of light, which may result in an electron transfer. The photon absorption activates a donor or an acceptor

for an electron transfer process that occurs only if the excitation energy is sufficient for the molecule to undergo a redox reaction.[37,38] Figure 1.12 presents the molecular orbital representations of oxidative and reductive electron transfers, where the chromophore either plays the role of the donor or the role of the acceptor.
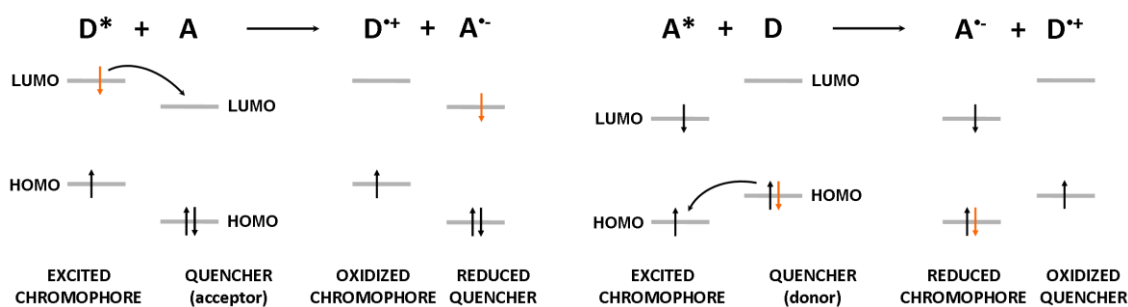
Figure 1.12 Molecular orbitals diagrams for oxidative (left) and reductive (right) PET between an excited chromophore and a ground state quencher.

Sensors based on the PET mechanism usually present a chromophore-spacer-ionophore architecture in which the receptor moiety contains an electron-donor group, and relies on the modulation of the fluorescence emission (ideally an off-on switching) as a transduction signal of the cation complexation event. Upon photoexcitation, an electron transfer occurs from the cation-free receptor to the excited chromophore resulting in a decrease or complete quenching of the fluorescence, as long as the process is thermodynamically favourable. Complexation of the cation affects the electron-donating strength of the ionophore subunit, decreasing its HOMO energy, and hence leads to higher oxidation potential. Under these conditions, PET is no longer possible and the fluorescence is enabled.
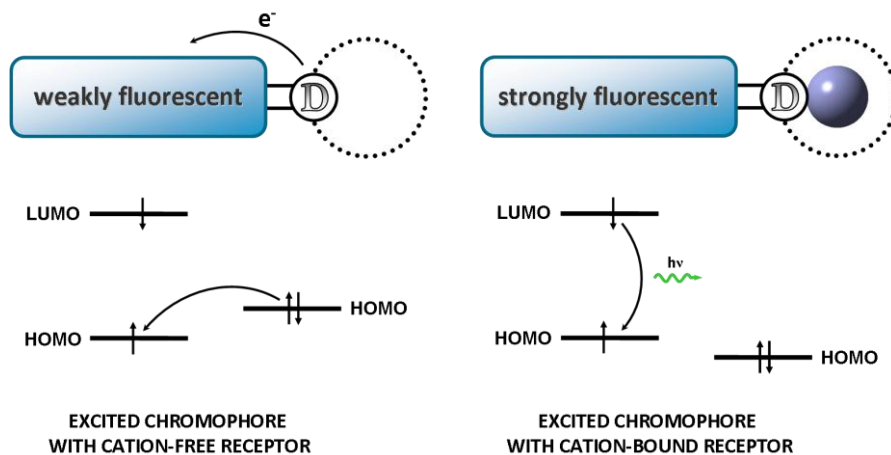
Figure 1.13 Principles of cation detection by PET sensor and associated frontier orbitals energy diagrams illustrating the electron transfer mechanism in the "on" and "off" states.

This can be illustrated within a frontier molecular orbitals picture as shown in Figure 1.13. Photoexcitation of the chromophore results in enabling an electron transfer from the HOMO of the guest-free ionophore to that of the chromophore and consequently a quenching of the fluorescence.

Whenever the oxidation potential of the chromophore is larger than that of the receptor, i.e. its HOMO is lower in energy, the PET process can occur and puts the chromophore in "off" state ; the opposite behaviour applies in the "on" state. Together with the choice of the right selective receptor for a given analyte as well as the choice of an appropriate spacer, this criterion on molecular orbitals energies and associated redox potentials guides the design of PET sensors for cations. The PET process in the framework of cation detection has been extensively studied over the last decades and numerous cation PET sensors have been developed.[39-42]

1.4.3 Chromophores studied in this work

1.4.3.1 Rylene derivatives

The rylene family of dyes is based on the highly functionalisable perylene core, which provides an ideal platform for further modulation.[43] Perylene (mono- and di-) imides are formed on the 3, 4, and/or 9, 10 positions and it is nowadays possible to introduce substituents at the bay and ortho positions (Figure 1.14).
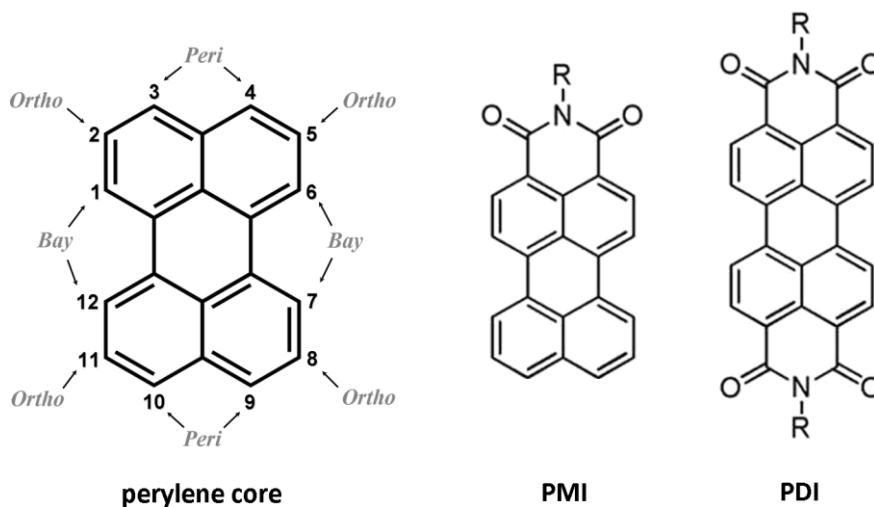
Figure 1.14 Chemical structures of the perylene core (with substitution positions) and perylenes mono- and diimide (PMI and PDI respectively).

Functionalised rylenes have been extensively studied since their discovery and owing to their exceptional chemical, thermal and photophysical properties (high molar extinction coefficient and fluorescence quantum yields among others) they are nowadays used in a broad range of domains, from industrial paints to electronic and optical applications such as

organic photovoltaic solar cells (OPVs), organic field-effect transistors (OFETs) or organic light-emitting diodes (OLEDs).[44-46]

The photophysical properties of perylene (di)imides can be modulated by expanding the aromatic system along the long molecular axis to obtain the higher order homologues terrylene (TDI), quaterrylene (QDI) and so on. The Absorption and emission spectra of these dyes are increasingly bathochromically shifted with the extension of the conjugated system, spanning a broad range of wavelengths in the Vis-NIR spectrum up to 950 nm in absorption for the hexarylenebis(dicarboximide)s. Substitution at the available bay positions (and peri position in the case of PMI) provides large possibilities for further improvement, for instance in terms of solubility or aggregation prevention as well as fine tuning of the optical properties.[47]

In the framework of chromoionophore design, PMI constitutes an advantageous platform with the electron-acceptor imide group to generate push-pull systems able to exhibit strong intramolecular charge transfer when coupled to electron-donor ionophores at the bottom peri position.

1.4.3.2 BODIPY derivatives

Discovered in 1968 by Treibs and Kreuzer[48], BODIPY dyes have ever since been the subject of numerous comprehensive investigations and are nowadays, owing to their remarkable properties, very popular in many different applications including photovoltaic and luminescent devices[49,50], fluorescent switches[51], laser dyes[52], and chemosensors, among others. BODIPY dyes possess indeed outstanding chemical, thermal and photochemical stability, high quantum yield and extinction coefficient, as well as quasi insensitivity to solvent polarity and pH. Their versatility

originates from the broad range of functionalisations possible on the BODIPY core (Figure 1.15), to generate a large variety of structures.
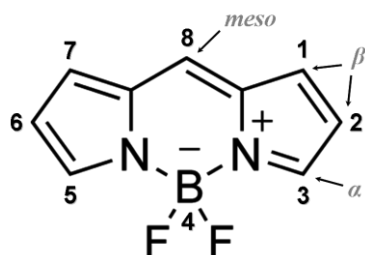
Figure 1.15 Structure and IUPAC numbering of the BODIPY core.

Chemical modification at the *meso*-position has no significant effect on the absorption and emission wavelengths but leads to an alteration of the fluorescence quantum yield. The presence for instance of an aryl group at the 8-position provides an efficient non-radiative de-excitation pathway due to the free rotation of the substituent. Fluorescence can be restored by the introduction of bulky groups at the 1,7-positions to prevent the rotation, leaving the BODIPY unit and the aryl ring conjugatively decoupled (Figure 1.16). Appropriate functionalisation at the *meso*-position constitutes also one of the strategies employed in the design of BODIPY-based chemosensors for cations relying on reductive or oxidative PET.[53]
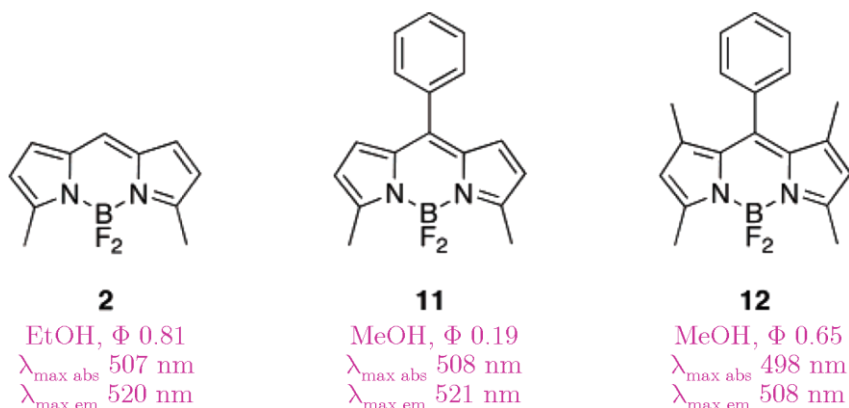
Figure 1.16 Illustration of the *meso*-substituent effect on spectroscopic properties (pictures taken from ref. 53).

3,5-substitution of the BODIPY core provides an efficient way to bathochromically shift the absorption and emission maxima, without significant effect on the extinction coefficient but with a negative impact on the fluorescence quantum yield arising from non-radiative energy dissipation via rotation of the substituent. The nature of the substitution can greatly modulate these effects and lead to larger spectral shifts together with increased quantum yields (Figure 1.17). Moreover, mono-substituted BODIPYs have blue-shifted absorption and emission compared to the di-substituted homologues. The decoration of the BODIPY core by functional groups at the 3,5-positions was also used to generate push-pull-like architectures and achieve the preparation of ICT-based cation sensors.[53]

83
CHCl$_3$, Φ 0.64
λ$_{max\ abs}$ 500 nm
λ$_{max\ em}$ 510 nm

85
CHCl$_3$, Φ 0.20
λ$_{max\ abs}$ 555 nm
λ$_{max\ em}$ 588 nm

87
CHCl$_3$, Φ 0.42
λ$_{max\ abs}$ 582 nm
λ$_{max\ em}$ 626 nm

88
CHCl$_3$, Φ 0.22
λ$_{max\ abs}$ 555 nm
λ$_{max\ em}$ 590 nm

89
CHCl$_3$, Φ 0.08
λ$_{max\ abs}$ 545 nm
λ$_{max\ em}$ 598 nm
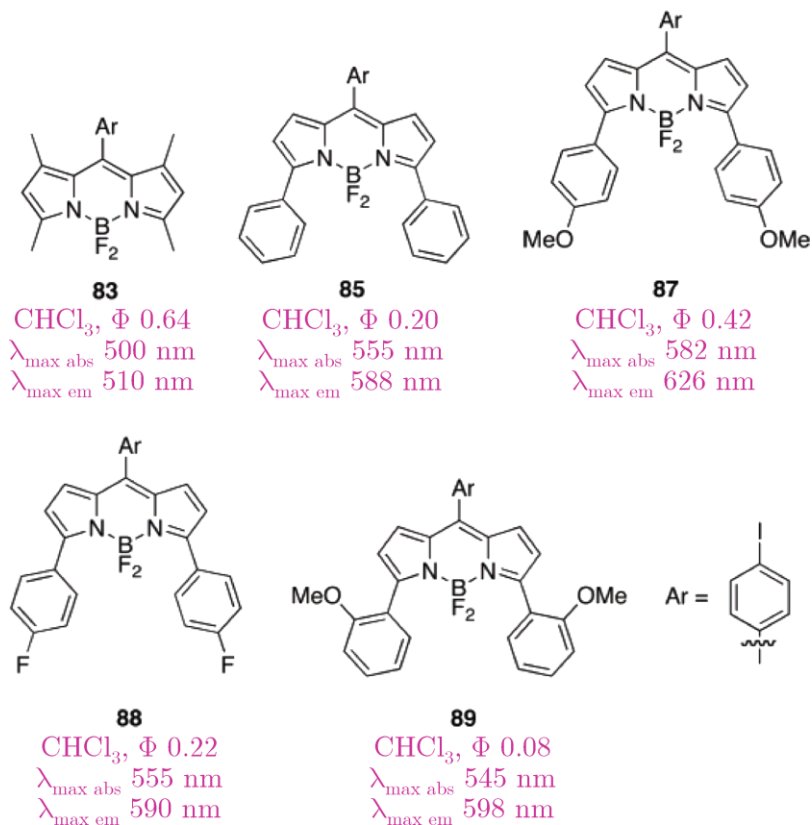
Figure 1.17 Illustration of the 3,5-substitution effects on the spectroscopic properties (figure taken from ref. 53).

More generally, spectral displacements towards longer wavelengths could be induced not only by the extension of the pi-conjugated system via substitution in all possible positions, but also by the rigidification of the structure, as it is presented in chapter 3, as well as the exchange of the carbon atom at the *meso*-position by a nitrogen atom (aza-BODIPYs).

References

[0]   modified from *http://infothread.org/Science/Physics/*, accessed 17/09/13.

[1]   J. W. Verhoeven, *Pure & Appl. Chem.* **68**, 2223 (1996).

[2]   M. Kasha, *Discuss. Faraday Soc.* **9**, 14 (1950).

[3]   N. Turro, V. Ramamurthy, W.Cherry, W. Farneth, *Chem. Rev.* **78**, 125 (1978).

[4]   C. Reichardt, *Solvents and Solvent Effects in Organic Chemistry*, 3rd Ed. Wiley- VCH (2003).

[5]   A. R. Katritzky, D. C. Fara, H. Yang, K. Tämm, T. Tamm, M. Karelson, *Chem. Rev.* **104**, 175 (2004).

[6]   F. Baldini, J.Homola, S. Martellucci, A. Chester, eds., *Optical Chemical Sensors*, *NATO Science Series*, **224**, Springer, the Netherlands (2006).

[7]   C. McDonagh, C. S. Burke, and B. D. MacCraith, *Chem. Rev.* **108**, 400 (2008).

[8]   G. Korotcenkov (ed.), *Chemical Sensors: Fundamentals of Sensing Materials.Vol.1,General Approaches*, Momentum Press, New York, USA (2010).

[9]   F.-G. Bănică, Chemical Sensors and Biosensors: Fundamentals and Applications, 1st Ed. John Wiley & Sons, Ltd. (2012).

[10]   K. Cammann, E. A. H. Hall, R. Kellner, H. L. Schmidt, O. S. Wolfbeis, *Cambridge Definition of Chemical Sensors, Cambridge Workshop on Chemical Sensors and Biosensors;* Cambridge University Press: New York (1996).

[11]   J. B. Neilands, *J. Biol. Chem.* **270**, 26723 (1995).

[12]   F. Tian, T. A. Cross, *J. Biol. Chem.* **285**, 1993 (1999).

[13] G. W. Gokel, W. M. Leevy, M. E. Weber, *Chem. Rev.* **104**, 2723 (2004).

[14] F. Fages, J. P. Desvergne, H. Bouas-Laurent, P. Marsau, J.-M. Lehn, F. Kotzyba-Hibert, A. M. Albrecht-Gary, M. Al-Joubbeh, *J. Am. Chem. Soc.* **111**, 8672 (1989).

[15] R. Ludwig, N. T. K. Dzung, *Sensors* **2**, 397 (2002).

[16] C. J. Pedersen, *J. Am. Chem. Soc.* **89**, 7017 (1967).

[17] S. Biniecki, S. Kabzinska, *Ann. Pharm. Fr.* **22**, 685 (1964).

[18] R. D. Hancock and A. E. Martell, *Chem. Rev.* **89**, 1875 (1989).

[19] D. J. Cram, *Science*, **240**, 760 (1988).

[20] J. L. Atwood, J. E. D. Davies, D. D. MacNicol, F. Vögtle, J.-M. Lehn, eds. *Comprehensive Supramolecular Chemistry* (Elsevier, Amsterdam), Vols. 1–11 (1996).

[21] M-J. Li, D. A. Nolan, *J. Lightwave Technol.* **26**, 1079 (2008).

[22] H. F. Ji, R. Dabestani, G. M. Brown, R. L. Hettich, *Photochem. Photobiol.* 1999, **69**, 513-516.

[23] A. P. de Silva, H. Q. N. Gunaratne, T. Gunnlaugsson, A. J. M. Huxley, C. P. McCoy, J. T. Rademacher, T. E. Rice, *Chem. Rev.* **97**, 1515 (1997).

[24] B. Valeur, *Molecular Fluorescence: Principles and Applications*, Wiley-VCH (2001).

[25] J. F. Callan, A. P. de Silva, D. C. Magri, *Tetrahedron*, **61**, 8551 (2005).

[26] Z. Liu, W. He, Z. Guo, *Chem. Soc. Rev.* **42**, 1568 (2013).

[27] J. Cornil, D. A. dos Santos, D. Beljonne, J. L. Brédas, *J. Phys. Chem.* **99**, 5604 (1995).

[28] W. Rettig, *Appl. Phys. B*, **45**, 145 (1988).

[29] J. Bourson, B. Valeur *J. Phys. Chem.* **93**, 3871 (1989).

[30] B. Valeur, I. Leray, *Coord. Chem. Rev.* **205**, 3 (2000).

[31] F. Qian, C. Zhang, Y. Zhang, W. He, X. Gao, P. Hu, Z. Guo, *J. Am. Chem. Soc.* **131**, 1460 (2009).

[32] V. Tharmaraj, S. Devi, K. Pitchumani, *Analyst*, **137**, 5320 (2012).

[33] K. Rurack, M. Kollmannsberger, U. Resch-Genger, J. Daub, *J. Am. Chem. Soc.* **122**, 968 (2000).

[34] W. Qin, M. Baruah, M. Sliwa, M. Van der Auweraer, W. M. De Borggrave, D. Beljonne, B. Van Averbeke, N. Boens, *J. Phys. Chem A*, **112**, 6104 (2008).

[35] R. A. Bissell, A. P. de Silva, H. Q. N. Gunaratne, P. L. M. Lynch, G. E. M. Maguire, C. P. McCoy, K. R. A. S. Sandanayake, *Top. Curr. Chem.* **168**, 223 (1993).

[36] A. P. de Silva, T. S. Moody, G. D. Wright, *Analyst*, **134**, 2385 (2009).

[37] A. Weller, *Pure Appl. Chem.* **16**, 115 (1968).

[38] M. A. Fox and M. Chanon (Eds.), *Photoinduced electron transfer*, Elsevier, Amsterdam, (1988).

[39] A.P. De Silva, S. A. de Silva, *J. Chem. Soc. Chem. Commun.* 1709 (1986).

[40] E. U. Akkaya, M. E. Huston, and A. W. Czarnik, *J. Am. Chem. Soc.* **112**, 3590 (1990).

[41] G. K. Walkup, S. C. Burdette, S. J. Lippard, R. Y. Tsien, *J. Am. Chem. Soc.* **122**, 5644 (2000).

[42] T. Hirano, K. Kikuchi, Y. Urano, T. Higuchi, T. Nagano, *Angew. Chem. Int. Ed.* **39**, 1052 (2000).

[43] T. Weil, T. Vosch, J. Hofkens, K. Peneva, K. Müllen, *Angew. Chem. Int. Ed.* **49**, 9068 (2010).

[44] C. Li, H. Wonneberger, *Adv. Mater.* **24**, 613 (2012).

[45] S. Schols, S. Verlaak, C. Rolin, D. Cheyns, J. Genoe, P. Heremans, *Adv. Funct. Mater.* **18**, 136 (2008).

[46] X. Zhan, A. Facchetti, S. Barlow, T. J. Marks, M. A. Ratner, M. R. Wasielewski, S. T. Marder, *Adv. Mater.* **23**, 268 (2011).

[47] C. Li, J. Schöneboom, Z. Liu, N. G. Pschirer, P. Erk, A. Herrmann, K. Müllen, *Chem. Eur. J.* **15**, 878 (2009).

[48] A. Treibs, F. H. Kreuzer, *Justus Liebigs Ann. Chem.* **718**, 208 (1968).

[49] T. Rousseau, A. Cravino, T. Bura, G. Ulrich, R. Ziessel, J. Roncali, *Chem. Comm.* **13**, 1673 (2009).

[50] L. Bonardi, H. Kanaan, F. Camerel, P. Jolinat, P. Retailleau, R. Ziessel, *Adv. Funct. Mater.* **18**, 401 (2008).

[51] T. A. Golovkova, D. V. Kozlov, D. C. Neckers, *J. Org. Chem.* **70**, 5545 (2005).

[52] T. López Arbeloa, F. López Arbeloa, I López Arbeloa, I. García-Moreno, A. Costela, R. Sastre, F. Amat-Guerri, *Chem. Phys. Lett.* **299**, 315 (1999).

[53] A. Loudet, K. Burgess, *Chem. Rev.* **107**, 4891 (2007).

Chapter 2

Quantum chemistry methods

At the end of the 19th century, electromagnetism and classical mechanics were successful in rationalising all physical phenomena. However, it became soon clear that the behaviour of elementary particles was not governed by classical laws. The Planck "quantisation" (1900)[1] being the first crack of the classical edifice, it was not long before Newton's old suggestion of light consisting in particles revived through Einstein's key experiment of the photoelectric effect (1905)[2] and subsequent avant-garde light quantum hypothesis. Unravelling the schizophrenic behaviour of light paved the way for the ground breaking proposition of De Broglie who postulated that matter was also subject to the so-called wave-particle duality (1924)[3]. The need for a wave equation to support a wave theory of matter was fulfilled two years later when Schrödinger came up with the most fundamental equation of quantum mechanics.

2.1 The Schrödinger equation and the wavefunction

As a consequence of the probabilistic aspect of the quantum theory, a new mathematical tool is introduced to treat the possible positions of the particles, the wavefunction $\psi(x,y,z,t)$. Having no physical meaning itself, its square represents the probability density for the particle to be in a given point of space (x,y,z) at a time t. Moreover, it allows the calculation of all the electronic properties of the system.

To characterise the time evolution of a quantum state, the time-dependent Schrödinger equation has to be solved:

$$i\hbar \frac{\partial}{\partial t} \Psi(t) = \hat{H}(t)\Psi(t) \qquad (2.1)$$

with $\Psi(t)$ the wavefunction of the system, $\hbar$ the reduced Planck constant, and $\hat{H}(t)$ the Hamiltonian of the system. However, one is usually dealing with stationary states so that the $\hat{H}$ operator does not explicitly depend on time, but simply on the coordinates of the particles $(\boldsymbol{r},\ R)$. The Schrödinger equation reduces then to its time-independent formulation[4] :

$$\hat{H}_{tot}\Psi(\boldsymbol{r},R) = E_{tot}\Psi(\boldsymbol{r},R) \qquad (2.2)$$

where $\Psi(\boldsymbol{r},R)$ is the wavefunction of the system that depends on $\boldsymbol{r}$ and R, the electrons and nuclei spatial coordinates, respectively, E_{tot} is the total energy of the system, and $\hat{H}_{tot}$ the total Hamiltonian of a system of m nuclei and n electrons. The latter can be written as the sum of the kinetic and potential energies of the nuclei and electrons:

$$\hat{H}_{tot} = T_n + T_e + V_{ne} + V_{ee} + V_{nn} \qquad (2.3)$$

with T_n and T_e, the nuclear and electronic kinetic energy, V_{ne} the attractive interaction between nuclei and electrons, V_{ee} the repulsive electron-electron interactions, and V_{nn} the repulsive interaction between nuclei. It is defined in atomic units ($m_e = \hbar = 4\pi\varepsilon_0 = e = 1$) as:

$$\hat{H}_{tot} = -\sum_{a=1}^{m} \frac{1}{2m_a}\nabla_a^2 - \sum_{i=1}^{n} \frac{1}{2}\nabla_i^2 - \sum_{i=1}^{n}\sum_{a=1}^{m} \frac{Z_a}{r_{ia}}$$
$$+ \sum_{i=1}^{n}\sum_{j>i}^{n} \frac{1}{r_{ij}} + \sum_{a=1}^{m}\sum_{b>a}^{m} \frac{Z_a Z_b}{r_{ab}} \tag{2.4}$$

where m_a is the mass of the atom a, Z_a and Z_b the nuclei charge of atom a and b respectively, r_{ab} the distance between the nuclei a and b, r_{ia} the distance between the nucleus a and electron i, and r_{ij} the distance between electrons i and j.

Because of the complexity associated with interdependency in the motion of the particles, exact solutions of the Schrödinger equation only exist for a small set of simple quantum systems such as the hydrogen atom or hydrogenoïd systems. Therefore, several approximations are typically used, as described below.

2.2   The Born-Oppenheimer approximation

Considering that the nuclei are moving much more slowly than the electrons (they are more than 1800 times lighter in mass than neutrons and protons), one can assume that the electronic cloud somehow instantaneously adapts to the molecular geometry. Born and Oppenheimer proposed in 1927 to decouple the electronic and nuclear motions[5]. This approximation, referred to as the Born-Oppenheimer approximation (or adiabatic approximation), results in neglecting the kinetic energy of the nuclei (T_n) and considering the interactions between

nuclei (V_{nn}) to be a constant for a given geometry. The electronic Hamiltonian depends explicitly on the electron coordinates (only parametrically on the nuclear positions) and is defined as:

$$\hat{H}_{el} = T_e + V_{ne} + V_{ee} \qquad (2.5)$$

It is then reasonable to factorise the total molecular wavefunction as follows:

$$\Psi_{BO}(\boldsymbol{r}, R) = \Psi_{elec}(\boldsymbol{r}, R)\,\Psi_{nuc}(R) \qquad (2.6)$$

with Ψ_{elec} the electronic wavefunction and Ψ_{nuc} the nuclear wavefunction, and solve the Schrödinger equation for the electrons alone in the field of the fixed nuclei. In this picture, nuclei are moving on a potential energy surface (PES) that is solution of the electronic Schrödinger equation.

In the framework of the Born Oppenheimer approximation, one still cannot find solutions to the electronic Schrödinger equation for polyatomic systems containing more than one electron and further approximations have to be introduced.

2.3   The independent model

Within this model, electrons of the system are supposed to be non-interacting. Neglecting the electron-electron interactions allows to "split" the electronic Hamiltonian for N independent electrons into a sum of one-electron Hamiltonians, each describing the motion of the i*th* electron in the average field due the other electrons (and the potential of the nuclei). The electronic Schrödinger equation can be written as a set of N mono-electronic equations that can be solved independently:

$$h_i\varphi_i(r) = \varepsilon_i\varphi_i(r) \qquad (2.7)$$

with h_i the one electron Hamiltonian of the ith electron, containing its kinetic energy term T_e and the attractive interaction with the nuclei V_{ne}, and ε_i the energy of the one-electron state $\varphi_i(r)$. Eigenfunctions of $\hat{h}_i$ are known : the hydrogenoïd spin-orbitals, product of one-electron orbital and a spin function σ are the building blocks of the total electronic wavefunction. The total energy is then simply the sum of the individual energies and the total wavefunction the product of the spin-orbitals (or Hartree product). Thus, one just has to choose a set of spin-orbitals to describe the electrons and obtain the total electronic energy of the system. However, this model should be considered as a minimal description only and leads to mediocre results.

Moreover, one has to take into account the fact that electrons are indistinguishable to build a correct wavefunction. This property imposes that electrons must be described by wavefunctions that are antisymmetric with respect to particle exchange (spatial and spin coordinates). Such a many-electron wavefunction, satisfying the antisymmetry principle, can be, in the simplest case of a closed-shell system, written as a Slater Determinant[6] (SD) of the one-electron wavefunctions, antisymmetric by construction. In the general case of N electrons and N spin-orbitals, the SD is expressed as:

$$\Phi(1,2,...,N) = \frac{1}{\sqrt{N!}} \begin{vmatrix} \varphi_1(1)\sigma_1(1) & \varphi_2(1)\sigma_2(1) & ... & \varphi_N(1)\sigma_N(1) \\ \varphi_1(2)\sigma_1(2) & \varphi_2(2)\sigma_2(2) & ... & \varphi_N(2)\sigma_N(2) \\ ... & ... & ... & ... \\ \varphi_1(N)\sigma_1(N) & \varphi_2(N)\sigma_2(1) & ... & \varphi_N(N)\sigma_N(N) \end{vmatrix} \qquad (2.8)$$

Note that, any two of the spin-orbitals cannot be identical to avoid the determinant being equal to zero, in agreement with the Pauli principle

which states that two electrons cannot have all the same quantum numbers.

2.4 The Hartree-Fock formalism

2.4.1 The Hartree-Fock method

Based on the variational principle[7], which states that the energy of an approximate wavefunction is always an upper bound of the true energy, the Hartree-Fock model[8,9] allows the determination of the "best" electronic wavefunction Ψ, considering that it can be approximated by an antisymmetrised product of N one-electron wavefunctions, i.e., a unique Slater Determinant. In the HF framework, each electron is moving in the average electrostatic field created by all the other electrons.

From a trial SD, the variational principle can be applied to generate the "best" one that minimises the electronic energy, the expected energy being calculated as:

$$E_{approx} = \frac{\left\langle \Psi_{trial} \left| \hat{H} \right| \Psi_{trial} \right\rangle}{\left\langle \Psi_{trial} \middle| \Psi_{trial} \right\rangle} \geq E_0 \tag{2.9}$$

The HF energy is the expectation value of the electronic Hamiltonian operator on a Slater Determinant and is, for a closed shell system of N electrons, given by:

$$E = \sum_{i=1}^{N} 2H_{ii} + \sum_{i=1}^{N} \sum_{j=1}^{N} \left(2J_{ij} - K_{ij} \right) \tag{2.10}$$

where:

$H_{ii} = \langle \varphi_i(r_i) | \hat{h} | \varphi_i(r_i) \rangle$, is the average energy of an electron in the field of the nuclei (i.e., the sum of the kinetic energy of the electron and the attractive interaction)

$J_{ij} = \langle \varphi_i(r_i)\varphi_j(r_j) | \dfrac{1}{r_{ij}} | \varphi_i(r_i)\varphi_j(r_j) \rangle$, the Coulomb integral, is the electrostatic repulsion between two electrons with electronic density of $|\varphi_i(r_i)|^2$ and $|\varphi_j(r_j)|^2$, respectively,

$K_{ij} = \langle \varphi_i(r_i)\varphi_j(r_i) | \dfrac{1}{r_{ij}} | \varphi_j(r_j)\varphi_i(r_j) \rangle$, the exchange integral, arises from the antisymmetry condition imposed on the wavefunction and has no classical equivalent.

Minimising the expectation value of the energy via the variational method, one can show that the optimal spin-orbitals are eigenfunctions of the effective one-electron Fock operator $\hat{f}_i$ and satisfies the Hartree-Fock equations:

$$\hat{f}_i \varphi_i = \varepsilon_i \varphi_i \tag{2.11}$$

where ε_i is the energy of the spin orbital φ_i and the Fock operator is expressed as:

$$\hat{f}_i = \hat{h} + \sum_{j=1}^{N} 2\hat{J}_j - \hat{K}_j \tag{2.12}$$

with $\hat{h} = -\dfrac{1}{2}\nabla_i^2 - \sum_{a=1}^{m} \dfrac{Z_a}{r_{ia}}$, the one-electron Hamiltonian from the independent model,

$\hat{J}_j = \left\langle \varphi_j(r_j) \left| \dfrac{1}{r_{ij}} \right| \varphi_j(r_j) \right\rangle$, the Coulomb operator, which accounts for the interaction between an electron at position r_i and the average charge distribution of another electron in the spin orbital φ_j,

$\hat{K}_j \varphi_i(r_i) = \left(\left\langle \varphi_j(r_j) \left| \dfrac{1}{r_{ij}} \right| \varphi_i(r_j) \right\rangle \right) \varphi_j(r_i)$, the exchange operator defined with respect to the spin orbital upon which it is applied, and where occupied orbitals are considered.

Considering the HF energy equation, one can notice that the term i=j is allowed in the double summation, meaning that in this case, the Coulomb interaction of an electron with its own charge distribution will be taken into account. As a consequence, the Coulomb integral will not be equal to zero even if one computes the energy of a one-electron system (where there is obviously strictly no electron-electron repulsion). This physical nonsense, known as the self-interaction error, is well handled in the HF formalism as for i=j, Coulomb and exchange terms are equal and therefore exactly cancel. We will see that the treatment of exchange and correlation becomes a major issue in the Density Functional Theory (DFT) approach (see section 2.6).

As the Fock operator depends on the orbitals that themselves enter the expression of the Coulomb and exchange operators, the problem has to be solved by an iterative procedure referred to as the Hartree-Fock Self-Consistent Field (SCF). Starting from a set of N trial orbitals $\varphi_i^{(trial)}$, the energy $E^{(trial)}$ is calculated. In a second step, the Fock operator $\hat{F}^{(1)}$ is formed and the Hartree-Fock equations solved, giving a new set of orbitals $\varphi_i^{(1)}$ that is used in the next iteration and a new energy $E^{(1)}$ is calculated, as well as a new Fock operator $\hat{F}^{(2)}$. This cycle continues until the new set of orbitals differs by less than a predefined threshold from the

orbitals used to build the Fock operator, i.e., until the energy (or the electronic density) converges.

2.4.2 The Roothaan-Hall approximation

If the method briefly described above is sufficient in the case of atoms and some diatomic molecules, one has to rely on the Roothaan-Hall approximation[10,11] to solve the Hartree-Fock equations for non linear molecules. In this formalism, the molecular orbitals φ_i are expressed as a linear combination of a finite set (or basis set) of predefined basis functions χ_p, called atomic orbitals (Linear Combination of Atomic Orbitals, LCAO):

$$\varphi_i = \sum_p^K C_{pi}\chi_p \tag{2.13}$$

where C_{pi}, the LCAO coefficients, gives the weight of the p-th atomic orbital χ_p in the i-th molecular orbital φ_i, and K the dimension of the basis set (number of basis functions).

Note that the use of a complete basis set (i.e. $K=\infty$) leads to the wavefunction corresponding to the lowest possible Hartree-Fock energy, the Hartree-Fock limit.

Substituting the LCAO expansion in the Hartree-Fock equations yields:

$$\hat{f}_i\left(\sum_p^K C_{pi}\chi_p\right) = \varepsilon_i \sum_p^K C_{pi}\chi_p \tag{2.14}$$

Multiplying by χ_q on both side and integrating leads to the Roothaan-Hall equations:

$$\sum_{p}^{K} C_{pi} \left\langle \chi_p \left| \hat{f} \right| \chi_q \right\rangle = \varepsilon_i \sum_{p}^{K} C_{pi} \left\langle \chi_p \left| \chi_q \right\rangle \right. \tag{2.15}$$

or, in matrix form:

$$\mathbf{FC} = \varepsilon \mathbf{SC} \tag{2.16}$$

where $\mathbf{S}$ is the overlap matrix with elements $S_{pq} = \left\langle \chi_p \left| \chi_q \right\rangle \right.$, and $\mathbf{F}$ is the Fock matrix with elements F_{pq} given by :

$$F_{pq} = \left\langle \chi_p \left| -\frac{1}{2}\nabla^2 - \sum_{a}^{m}\frac{Z_a}{r_{ia}} \right| \chi_q \right\rangle + \sum_{j}^{N} 2 \left\langle \chi_p \left| \hat{J}_j \right| \chi_q \right\rangle - \left\langle \chi_p \left| \hat{K}_j \right| \chi_q \right\rangle \tag{2.17}$$

Recalling the expressions of the Coulomb and exchange operator and using the LCAO expansion of $\varphi_j(r_j)$,

$$\begin{aligned} F_{pq} &= \left\langle \chi_p \left| -\frac{1}{2}\nabla^2 - \sum_{a}^{m}\frac{Z_a}{r_{ia}} \right| \chi_q \right\rangle \\ &+ \sum_{j}^{N}\sum_{r}^{K}\sum_{s}^{K} C_{jr} C_{js} \left[2\left(pq \middle| rs \right) - \left(pr \middle| qs \right) \right] \end{aligned} \tag{2.18}$$

where the first term accounts for the one electron part while the $(pq|rs)$ and $(pr|qs)$ terms corresponds to the two electrons Coulomb and exchange integrals, respectively, that can be written as:

$$\left(pq \middle| rs \right) = \left\langle \chi_p(r_1)\chi_q(r_1) \left| \frac{1}{r_{12}} \right| \chi_r(r_2)\chi_s(r_2) \right\rangle \tag{2.19}$$

The orbitals χ_p and χ_q associated to the electron n°1 are centered on the atoms p and q, and equivalently, the orbitals χ_r and χ_s associated to the electron n°2 are centered on the atoms r and s.

The LCAO coefficients obtained by solving the Roothaan-Hall equations also appear in the definition of the Fock operator, so that a SCF procedure is adopted. Given a defined basis set, an initial guess is made for the C_{pi} coefficients and the F_{pq} elements are calculated. By diagonalisation of the $F_{pq} - \varepsilon_i S_{pq}$ matrix, one can determine the ε_i and generate a new set of LCAO coefficients, used in turn to define a new Fock operator, and so on. The procedure stops when a predefined convergence criterion is reached (generally comparing the difference in the "new" and "old" energies).

2.4.3   Semi-empirical methods

In an *ab initio* Hartree-Fock calculation, all the one- and two-electrons integrals are explicitly calculated in the Roothaan-Hall SCF procedure with a specified basis set. One can easily foresee the main practical limitations of such an approach : as the number of atoms increases, the number of atomic functions used to build the Fock matrix rapidly grows as well as the number of bi-electronic integrals (N^4, with N basis functions) and the computational cost quickly becomes prohibitive. To tackle this issue, semi-empirical methods have been developed, which rely on several approximations to make the calculation more tractable without sacrificing the accuracy of the results.

First, usually only valence (sometimes only π) electrons are considered, and it is assumed that they are affected by a constant electrostatic potential due to the core electrons. The molecular orbitals are thus developed in the LCAO approximation using only the valence atomic orbitals. Secondly, some of the two-electron integrals and other Hamiltonian matrix elements are neglected or parameterised against experimental data. The different levels of approximation lead to a large

variety of methods, among which we have used in our work the AM1 model[12], as implemented in the AMPAC software[13].

Based on the NDDO approximation[14] (Neglect of Diatomic Differential Overlap) that mainly consists in neglecting the overlap matrix **S** (approximated as a unit matrix) and the two-electrons integrals $(pq|rs)$ containing a product of two orbitals centred on two different atoms, the Austin Model 1 method includes a modified nuclear repulsion term to account for hydrogen bonds and mimic van der Waals interactions via non-physical attractive forces. It has been parameterised to reproduce several physical quantities such as heats of formation, dipole moments, geometries and ionisation potentials of molecules in their ground-state.

2.4.4   The electron correlation and post Hartree-Fock methods

By considering that each electron is moving in the average electrostatic field created by all the other electrons, the Hartree-Fock method improperly treats the correlation between the motion of the electrons, as the instantaneous repulsion between them is neglected. Consequently, electrons virtually get "too close" to one another and the electron-electron repulsion energy is overestimated, so is the electronic energy. The difference between the HF limit E_{HF} and the exact energy E_{exact} is the so-called electron correlation energy:

$$E_{corr} = E_{exact} - E_{HF} \qquad (2.20)$$

Two contributions to the correlation are generally distinguished: the Fermi correlation, that deals with same spin electrons, and the Coulomb correlation, that accounts for interactions between electrons with opposite spins. While the HF approximation accounts exactly for exchange

interactions (inherent to the antisymmetric nature of the wavefunction, i.e. the SD), electrons with opposite spins are not correlated.

Provided one is using an extended basis set to solve the HF equations, 99% of the total energy can be accounted for. However, the missing ~1% may turn out to be determining in the description of certain chemical phenomena (dissociation of molecules, H_2 for example). Using HF method as starting point, several post Hartree-Fock methods[15] have been developed to improve E_{corr} to various extents and, among these, the Configuration Interaction (CI) used in this thesis is reviewed in detail in the following section. Note that other approaches are also available such as Møller-Plesset Perturbation Theory (MPx), Multi-Configuration Self-consistent Field (MCSCF), and Coupled-Cluster Theory (CC).[15,16]

2.5   Configuration interaction

If the Hartree-Fock method can account for the stability of a molecule, it is unable to describe properly the formation or dissociation of a bond. This limitation is inherent to the mono-determinantal expression of the wavefunction that does not provide enough flexibility: electrons are assigned to a given set of orbitals and the resulting constraints on the wavefunction restrict their spatial correlations.

The obvious solution to tackle this problem is to express the trial wavefunction as a linear combination of multiple determinants, each one corresponding to a given electronic configuration, so that the drawback inherent to "residential electrons" unable to move from one orbital to the other can be overcome. The aim of the configuration interaction is then to determine the best approximate N-electron wavefunction Ψ_{CI} as a linear combination of SD associated to all possible occupations possible of the HF orbitals that are held fixed:

$$\Psi_{CI} = a_0 \Phi_{HF} + \sum_{i=1} a_i \Phi_i \qquad (2.21)$$

As already mentioned, the HF solution account for ~99% of the energy and the HF wavefunction Φ_{HF} can thus reasonably be taken as the reference determinant and starting point. The a_i are the configuration interaction coefficients that have to be optimised so that the energy is minimum and Φ_i all the possible electronic configurations resulting from the promotion of electrons from occupied to virtual orbitals.

The CI wavefunction can be conveniently rewritten according to the order of excitations considered:

$$\Psi_{CI} = a_0 \Phi_{HF} + \sum_i^{occ} \sum_m^{virt} a_{i \to m}^S \Phi_{i \to m}^S$$
$$+ \sum_{i<j}^{occ} \sum_{m<n}^{virt} a_{ij \to mn}^D \Phi_{ij \to mn}^D + \sum_{i<j<r}^{occ} \sum_{m<n<s}^{virt} a_{ijr \to mns}^T \Phi_{ijr \to mns}^T + ... \qquad (2.22)$$

A full CI corresponds to a calculation where all the possible excitations are allowed, and is generally way too demanding to be achieved. Thus, one has to select the excitations that have to be considered (single and double -CISD- generally allow to recover a significant part of the correlation energy) as well as the molecular orbitals that will constitute the active space.

The variational principle is applied to find the best wavefunction that minimises the energy of the system with respect to the configuration interaction coefficients a_i and one has to solve the following matrix eigenvalue equation:

$$(\mathbf{H} - E)\mathbf{a} = 0 \qquad (2.23)$$

Note that in the MCSCF method, not only the a_i are optimised but also the molecular orbitals, allowing to account for a larger fraction of the correlation energy compared to the CI technique.

Although post Hartree-Fock correlated methods give more accurate results owing to the inclusion of electron correlation, they are computationally expensive and not very practical once the system studied becomes large and complex. Density Functional Theory provides an interesting alternative that includes electron correlation at a relatively low computational cost, so that larger systems can be treated.

2.6   Density Functional Theory

Although the wavefunction Ψ is the key to all information one would like to obtain about a particular system, this rather unintuitive quantity that depends on three spatial and one spin coordinates for each electron quickly becomes very complicated to treat. Recalling that the Hamiltonian only depends on the positions and charges of the nuclei and the number of electrons in the system, the electron density of the system, which is not a function of the number of electrons, appears to be a good candidate among the various physical observables of a system, since its integration over all space gives the total number of electrons N of the system:

$$\int \rho(r)\,dr = N \qquad (2.24)$$

The position of the nuclei corresponds to local maxima of $\rho(r)$ while the atomic charges can be obtained from the electronic density at the position of the nuclei. Intuitively, the electron density could thus in principle be used to form an Hamiltonian operator and solve the Schrödinger equation.

The year 1927 marks the very first step of electron density based approaches (rather than wave-function based theories) with the work of Thomas[17] and Fermi[18]. In their model, a classical expression is used for the nuclear-electron and electron-electron potentials while the kinetic energy of electrons, based on an uniform electron gas (i.e. constant electron density), is derived from a quantum statistical model; the Thomas-Fermi expression of the energy is given by:

$$E_{TF}[\rho] = \frac{3}{10}(3\pi^2)^{2/3} \int \rho^{5/3}(r)dr - Z\int \frac{\rho(r)}{r}\,dr$$
$$+ \frac{1}{2}\iint \frac{\rho(r_1)\rho(r_2)}{r_{12}}\,dr_1 dr_2$$

(2.25)

Improvement was attempted by Dirac[19] who included an exchange term in the expression (first derived by Bloch[20]), yielding the Thomas-Fermi-Dirac model, which proved to be still not satisfactory[21]. Although these models are not showing themselves to be reliable and practically useful, as they predict molecules to be unstable relative to their separated constituents (no chemical bonds !), they constituted the first attempts to express the energy solely from the electron density of the system.

Decades later, Hohenberg and Kohn were to lay the foundations of modern density functional theory[22].

2.6.1   The Hohenberg-Kohn theorems

The first Hohenberg-Kohn theorem, often referred to as the "proof of existence", states that, considering a system of electrons moving in an external field $v_{ext}(\boldsymbol{r})$, "*the external potential $v_{ext}(\boldsymbol{r})$ is (to within a constant) a unique functional of $\rho(\boldsymbol{r})$; since, in turn $v_{ext}(\boldsymbol{r})$ fixes $\hat{H}$ we see that the full many particle ground state is a unique functional of $\rho(\boldsymbol{r})$*". In other terms, a given electron density $\rho(\boldsymbol{r})$ uniquely determines the

Hamiltonian operator and consequently the wavefunction and all electronic properties of the system.

In this framework, the electronic energy is expressed as a functional of $\rho(\boldsymbol{r})$:

$$E[\rho] = \underbrace{T_e[\rho] + E_{ee}[\rho]}_{F_{HK}[\rho]} + E_{ne}[\rho] \qquad (2.26)$$

While the nuclear-electron attractive potential $E_{ne}[\rho]$ is system dependent, the Hohenberg-Kohn functional $F_{HK}[\rho]$, constituted by the kinetic energy term and the repulsion between electrons, is a universal functional.

According to the second theorem, "$E[\rho]$ *assumes its minimum value for the correct $\rho(\boldsymbol{r})$, if the admissible functions are restricted by the condition* $N = \int \rho(r)dr$". It is nothing but a statement of the variational principle, already used in the wavefunction models, for the density. It implies that any trial electron density ρ_{trial} will always give an energy larger than the true ground-state energy. Assuming that the $F_{HK}[\rho]$ functional is exact, it delivers the ground-state energy minimum of the system if and only if the input electron density is the true ground-state density.

2.6.2   The Kohn-Sham formalism

The main reason for the failure of Thomas-Fermi like approaches lies in the expression of the kinetic energy $T_e(\rho)$ within the homogeneous gas model as well as in the classical treatment of electron interactions (correlation, self-interaction error). On the basis of the cornerstone's theorems of DFT, Kohn and Sham[23] proposed in 1965 an approach to recast the equations into a solvable and practical form.

Considering a fictitious system of N non-interacting electrons moving in an external potential $v_{ext}(r_i)$, that can be exactly represented by a Slater Determinant of N spin-orbitals ϕ_i, the Kohn-Sham orbitals, one can express the kinetic energy:

$$T_{ni} = \sum_i^N \langle \phi_i | -\frac{1}{2}\nabla_i^2 | \phi_i \rangle \qquad (2.27)$$

and define its electronic density as:

$$\rho(r) = \sum_{i=1}^N |\phi_i(r)|^2 \qquad (2.28)$$

Even if, as already mentioned, the universal functional $F_{HK}[\rho]$ is unknown, one can define the effective potential $v_{eff}(r_i)$ that will render the density and energy of the fictitious non-interacting reference system identical to the one of the real interacting system such that the energy functional can be written as:

$$E[\rho] = T_{ni}[\rho] + E_{ee}[\rho] + E_{ne}[\rho] + \Delta T[\rho] \qquad (2.29)$$

with $T_{ni}[\rho]$ the kinetic energy of the non-interacting system,

$E_{ee}[\rho] = J[\rho] + E_{nc}[\rho]$, $J[\rho]$ the classical electron-electron repulsion and $E_{nc}[\rho]$ all the non-classical part of electron-electron repulsion (exchange, electrons correlation effects, self-interaction error), $E_{ne}[\rho]$, the nuclear-electron potential, and $\Delta T[\rho]$ the correction to the kinetic energy, necessary to account for the interacting nature of the electrons.

One can rewrite the DFT energy as:

$$E[\rho] = T_{ni}[\rho] + J[\rho] + E_{ne}[\rho] + E_{xc}[\rho] \qquad (2.30)$$

where $E_{xc}[\rho]$ is the so-called exchange-correlation term, that exists (HK theorem) but which exact expression remains unknown.

Assuming that $E_{xc}[\rho]$ is known, the problem can then be solved in a similar way as done for the HF model. The Kohn-Sham orbitals ϕ_i (linear combination of the basis functions) that minimise the energy satisfy the pseudo-eigenvalue equations:

$$\hat{f}_i^{KS}\phi_i = \varepsilon_i\phi_i \tag{2.31}$$

where the Kohn-Sham one-electron operator $\hat{f}_i^{KS}$ is defined as:

$$\hat{f}_i^{KS} = -\frac{1}{2}\nabla_i^2 + v_{eff}(r_i) \tag{2.32}$$

and $v_{eff}(r_i)$, the effective external potential,

$$v_{eff}(r_i) = \int \frac{\rho(r_2)}{r_{i2}}\,dr_2 - \sum_a^{nuclei}\frac{Z_a}{r_{ia}} + v_{xc}(r) \tag{2.33}$$

The KS potential depends explicitly on the density via the coulomb term and just like in HF, the problem has to be solved iteratively. Given a trial density, one can calculate the effective potential and solve the Kohn-Sham equations. The resulting orbitals ϕ_i give a new electron density (equation 2.28) that can be used to calculate a new effective potential and so on until a predefined threshold is reached. However, the exact expression $E_{xc}[\rho]$ is unfortunately not known and its approximate determination constitutes the key issue to DFT improvement.

2.6.3   Exchange-correlation functionals

If $E_{xc}[\rho]$ was exactly known, one would be able to calculate the true energy of a system, electron correlation included. It can be defined by making equivalent the energies of the real and fictitious system as:

$$E_{xc}[\rho] = (T_e[\rho] - T_{ni}[\rho]) + (E_{ee}[\rho] - J[\rho]) \qquad (2.34)$$

Its name might be a bit misleading as it does not only account for the non classical portion of the electron-electron interaction, but also includes the correction for the self-interaction error, and the missing part of the true kinetic energy arising from the non-interacting electrons approximation.

Up to now, its exact expression remains the holy grail of DFT and one has to rely on approximations, the quality of the resulting energy thus depending on the accuracy of the functional form chosen. There exists no systematic strategy to improve a functional, and even more dramatic, violation of required physical conditions in its expression does not necessarily lead to less accurate results. A set of precise reference data is used to estimate the accuracy of a given functional, the G2 thermochemical database[24] being the most common.

Several improvements have been achieved since exchange-correlation functionals started being developed, and each new level of approximation has been associated by John P. Perdew to the mythical Jacob's Ladder rungs[25], each one allowing to recover the results of lower rungs while adding capabilities.

The assumption is generally made that exchange and correlation contributions are separable and the exchange-correlation energy functional can conveniently be expressed as:

$$E_{xc}[\rho] = \int \rho(r)\varepsilon_{xc}[\rho(r)]dr = E_x[\rho] + E_c[\rho]$$
$$= \int \rho(r)\varepsilon_x[\rho(r)]dr + \int \rho(r)\varepsilon_c[\rho(r)]dr \qquad (2.35)$$

where $\varepsilon_x[\rho(r)]$ and $\varepsilon_c[\rho(r)]$ are the exchange and correlation energy densities (per particle).

2.6.3.1   The Local (Spin) Density Approximation (L(S)DA)

The local density approximation is based on the model that gave birth to DFT, the uniform electron gas, where the density is considered to be locally constant, and it is assumed that the exchange and correlation potentials at a certain position depend only on the local value of this density, so that the exchange-correlation energy functional can be written as:

$$E_{xc}^{LDA}[\rho] = \int \rho(r)[\varepsilon_{xc}^{LDA}(\rho)]dr \qquad (2.36)$$

where the exchange part (of a uniform electron gas) is exactly known and given by the Dirac formula[18] :

$$E_x[\rho] = -\frac{3}{4}\left(\frac{3}{\pi}\right)^{1/3}\int \rho^{4/3}dr \qquad (2.37)$$

while there is no explicit form known for the correlation energy. Monte Carlo simulations of the homogenous electron gas have been performed by Ceperley and Alder[26] to numerically determine the correlation energy at very high accruracy. From this work, correlation functionals have been developed by Vosko, Wilk, and Nusair[27] (VWN) or Perdew and Wang (PW)[28].

Explicit introduction of the spin is achieved by defining ε_{xc} respective to a sum of α and β densities:

$$E_{xc}^{LSDA}[\rho_\alpha, \rho_\beta] = \int \rho(r)[\varepsilon_{xc}^{LSDA}(\rho_\alpha(r), \rho_\beta(r))]dr \qquad (2.38)$$

Being based on the crude approximation of the uniform electron gas, which might be reasonable for metals, L(S)DA does not perform so well for molecules, notably overestimating the bond energies and describing very poorly breaking or forming of bonds.

2.6.3.2   The Generalized gradient Approximation (GGA)

In molecular system, the electronic density is far from being uniform and improvements over the L(S)D Approximation have to account for the non-homogeneity of the true density. This is done within the Generalized Gradient Approximation by considering a dependency for ε_{xc} not only on the density, but also on the gradient of the density, i.e. allowing the density to locally change.

$$E_{xc}^{GGA}[\rho, \nabla\rho] = \int \rho(r)[\varepsilon_{xc}^{GGA}(\rho, \nabla\rho)]dr \qquad (2.39)$$

The majority of the GGA exchange-correlation functionals are constructed by adding a correction term to the L(S)DA functional, treating separately exchange and correlation parts. Note that these functionals have a rather complicated mathematical form that is chosen upon the quality and accuracy of the results, not the physics behind. Two approaches for their development have to be distinguished: a semi-empirical one, with parameters fitted to reproduce experimental data, among which the popular BLYP functional (Becke exchange functional[29]

and Lee, Yang, Parr correlation functional[30]), and the non-empirical like PW91[31] (Perdew and Wang) and PBE[32] (Perdew-Becke-Ernzenhof).

A step further is achieved with the meta-GGA functionals that include a dependency over the second-order derivatives of the density, though the associated computational cost and numerical stability problems do not necessarily translate into improved results.

Although all these functionals constitute a great improvement over the L(S)DA method, some efforts are still to be made to reach better accuracy and this motivated the development of hybrid functionals.

2.6.3.3 Hybrid functionals

The first attempt for improvement was based upon the idea that, the exchange energy being exactly given by the Hartree-Fock method, one could directly include it, even partially, in the functional expression, the correlation energy being purely calculated by DFT. In the framework of the Adiabatic Correction Method, one can make an exact connection between the non-interacting reference system and the fully interacting one, and using the Hellmann-Feynman theorem, compute the exchange-correlation energy as:

$$E_{xc} = \int_0^1 \langle \psi(\lambda) | v_{xc} | \psi(\lambda) \rangle \, d\lambda \qquad (2.40)$$

where λ describes the range of the electronic interactions. When $\lambda=0$, the electrons are totally uncorrelated and, a single Slater Determinant of Kohn-Sham orbitals being the exact wavefunction of the system, the exchange energy that remains is given exactly by the HF theory. For $\lambda=1$, the fully interacting system can be approximated by L(S)DA or GGA

functionals. Finally, when $0 < \lambda < 1$, the exchange-correlation functional is not known and the integral has thus to be approximated as a sum:

$$E_{xc}^{hybrid} = E_x^{HF} + k(E_{xc}^{DFT} - E_x^{HF}) = (1-a)E_{xc}^{DFT} + aE_x^{HF} \qquad (2.41)$$

Several attempts have been made where additional parameters weighting the contributions of L(S)DA and GGA exchange and correlation are determined together with the parameter a. Among the wide panel of hybrid functionals available, the most famous and widely used B3LYP[33] functional has the following expression:

$$E_{xc} = (1-a)E_x^{LSDA} + aE_x^{HF} + b\Delta E_x^B + (1-c)E_c^{LSDA} + cE_c^{LYP} \qquad (2.42)$$

where the parameters a, b and c, set respectively to 0.2, 0.72 and 0.81, have not been optimised as they are simply taken from the B3PW91 functional without further fitting of experimental data. E_x^{LSDA} and E_c^{LSDA} are the exchange and correlation at the LSDA level, E_x^{HF} the Hartree-Fock exchange, E_x^B the Becke exchange and E_c^{LYP} the Lee, Yang, Parr correlation energy. As compared with the G2 database, the average absolute error on atomisation energies (using a large basis set) of the B3LYP functional is only of about 2 kcal.mol^{-1}.[34] Note the parameter-free hybrid functional PBE1PBE[35] (or PBE0) that shows very promising results for many important molecular properties. However, in practice, one always has to chose the functional as carefully as possible accordingly to the system treated and the properties investigated.

2.6.3.4 Long-range corrected functionals

Certain failures of the aforementioned functionals, such as the inability to deal with charge-transfer excitations, are understood to arise from the incorrect long-range behaviour of the exchange potential. One way to

achieve correct asymptotic behaviour, is to introduce a partitioning of the Coulomb operator, in the exchange interaction, into short- and long-range components:

$$\frac{1}{r_{12}} = \frac{1 - erf(\mu r_{12})}{r_{12}} + \frac{erf(\mu r_{12})}{r_{12}} \quad (2.43)$$

The first term accounts for the short-range part of the Coulomb operator by DFT exchange while the second term describes long-range interactions with the exact HF exchange.

Various LC functionals are available, and among them, we used the CAM-B3LYP functional, which combines the widely used B3LYP functional with a Coulomb-attenuating method (CAM) potential. Within the CAM approach, two parameters are introduced in equation 2.43, to control the degree of mixing of DFT and exact HF exchange:

$$\frac{1}{r_{12}} = \frac{1 - \alpha + \beta erf(\mu r_{12})}{r_{12}} + \frac{\alpha + \beta erf(\mu r_{12})}{r_{12}} \quad (2.44)$$

with $0 \leq \alpha + \beta \leq 1$ and $0 \leq \beta \leq 1$.

CAM-B3LYP functional corresponds to values of $\alpha=0.19$ and $\beta=0.46$, with a value of $\mu=0.33$ a_0^{-1}.[36]

2.7   Time-Dependent Density Functional Theory

While limited to the ground state and thus not strictly applicable to excitation energies calculations, static DFT can be extended to investigate properties of a given system subject to an external time-dependent potential, i.e. an electric field. At the origin of TD-DFT, the Runge-Gross theorem[37] is the analogous of the first HK theorem and states that there is a one-to-one mapping between the time-dependent external potential

$v_{ext}(\boldsymbol{r},t)$ and the time-dependent density $\rho(\boldsymbol{r},t)$, the later allowing to determine all the observables of the system. Following the philosophy employed in the DFT approach, a reference system of N non-interacting electrons moving in an effective time-dependent potential $v_{eff}(\boldsymbol{r},t)$ is described by a Slater Determinant $\Psi(r,t)$ of mono-electronic orbitals $\phi_i(r,t)$ yielding the same charge density as the interacting system:

$$\rho(r,t) = \sum_{i=1}^{N} |\phi_i(r,t)|^2 \tag{2.45}$$

and satisfies the time-dependent Kohn-Sham (TDKS) equations:

$$i\frac{\partial}{\partial t}\phi_i(r,t) = \left(-\frac{1}{2}\nabla_i^2 + v_{eff}(r,t)\right)\phi_i(r,t) \tag{2.46}$$

where the effective potential is written as follow:

$$v_{eff}(r,t) = \int \frac{\rho(r',t)}{|r-r'|}\,dr' - \sum_{a}^{nuclei}\frac{Z_a}{r_{ia}} + v_{xc}(r,t) \tag{2.47}$$

$v_{xc}(\boldsymbol{r},t)$ the unknown time-dependent exchange-correlation potential is defined as:

$$v_{xc}(r,t) = \frac{\delta A_{xc}[\rho(r,t)]}{\delta\rho(r,t)} \tag{2.48}$$

where $A_{xc}[\rho(r,t)]$ is the time-dependent counterpart of the energy in static DFT and the exact density of the system is given at its stationary point.

As in DFT, the determination of the xc functional requires to introduce approximations, the first and simplest being the adiabatic approximation in which the ground-state exchange-correlation functional is evaluated at time-dependent densities.

$$v_{xc}[\rho(r,t)] \simeq \left. \frac{\delta E_{xc}[\rho(r)]}{\delta\rho(r)} \right|_{\rho=\rho(t)} = v_{xc}[\rho(r)]|_{\rho=\rho(t)} \qquad (2.49)$$

It is thus a local approximation in time expected to be valid provided that the perturbation on the system varies slowly in time, i.e. when the time dependence is small.

Within the TD-DFT approach, a second approximation based on the linear response theory is introduced for the calculation of excitation energies. If the time-dependent external perturbation of the system in its stationary ground state is considered to be small, one can retain only the linear response of the density of the system, referred to as LR-TD-DFT[38].

Considering a system in its ground-state $(\rho^{(0)}(r))$ subject to a small perturbation $v^{(1)}(r,t)$ at a time t_0, so the total external potential reads $v_{ext}(r,t) = v^{(0)}(r) + v^{(1)}(r,t)$, the concomitant linear change of the density with time as $\rho(r,t) = \rho^{(0)}(r) + \rho^{(1)}(r,t)$ will be described by the response function χ. It is however easier to calculate the response function of a Kohn-Sham system (that gives the density of the interacting system from a fictitious non-interacting one) than a fully interacting one.

The linear change $\rho^{(1)}(r,t)$ of such a system can be expressed in the frequency domain as:

$$\rho^{(1)}(r,\omega) = \int dr' \chi_{KS}(r,r',\omega) v_{eff}^{(1)}(r',\omega) \qquad (2.50)$$

with the non-interacting density response χ_{KS} expressed as:

$$\chi_{KS}(r,r';\omega) = \sum_{i,j} (f_i - f_j) \frac{\phi_i^*(r)\phi_j(r)\phi_j^*(r')\phi_i(r')}{\omega - (\varepsilon_j - \varepsilon_i) + i\delta} \qquad (2.51)$$

The KS effective potential reads:

$$v_{eff}^{(1)}(r,t) = \int \frac{\rho^{(1)}(r',t)}{|r-r'|} \, dr' + v_{ext}^{(1)}(r,t) + v_{xc}^{(1)}(r,t) \tag{2.52}$$

with the exchange-correlation part given as:

$$v_{xc}^{(1)}(r,t) = \int dt' \int dr' \underbrace{\frac{\delta v_{xc}(r,t)}{\delta \rho(r',t')}}_{f_{xc}} \rho^{(1)}(r',t') \tag{2.53}$$

where f_{xc} is the exchange-correlation kernel that depends on the unperturbed ground-state density and explicitly relates the response function of the interacting system χ to the KS one χ_{KS} (as a consequence of the requirement that the change of the density for both description is the same).

Combining the results with some mathematics, the relationship between χ and χ_{KS} is given by a Dyson-like equation:

$$\begin{aligned}
\chi(r,r';\omega) &= \chi_{KS}(r,r';\omega) \\
&+ \int d^3 r_1 \int d^3 r_2 \, \chi(r,r_1,\omega) \left[\frac{1}{r_1 - r_2} + f_{xc}(r_1,r_2;\omega) \right] \chi(r_2,r';\omega)
\end{aligned} \tag{2.54}$$

From this equation, one can find the excitation energies of the interacting system by searching for the poles of the response function (χ_{KS} has poles at the Kohn-Sham orbital energy differences). One must keep in mind that an accurate TD-DFT calculation relies on a good description of the ground-state density (exchange-correlation functional, basis set..).

2.8 Basis sets and pseudopotentials

2.8.1 Basis sets

As presented in section 4.4.2. and 4.6.2., the LCAO expansion of molecular orbitals yields the best result within a given method when an infinite basis set is used. However, achieving this optimal description of the system is beyond the computational capacities available and various basis sets have been developed, constituted by a limited number of mathematical functions, Slater-type orbitals[39] (STOs) or Gaussian-type orbitals[40] (GTOs), to reach accurate results as efficiently as possible. The STOs, although physically more attractive (directly deduced from the hydrogenoïd orbitals), suffer from calculatory complexity when dealing with poly-atomic molecules as multi-center integrals cannot be efficiently treated. To circumvent this issue, Boys proposed to use GTOs instead.[40] Computationally convenient as they ensure analytical solutions for all integrals, they are, however, not so well adapted to the description of the shape of the orbital : no discontinuity for $r = 0$ (i.e. at the nucleus) and too fast decay for $r \to \infty$. For these reasons, GTOs are used in a linear combination to reproduce as close as possible a STO. As an example, the STO-nG minimal basis sets combine n *primitive* GTOs into a contracted GTO to fit an STO, the most used and optimal being for n=3. Clearly, the more primitives combined, the better will be the fit with the STO, but the larger the computational effort associated. However, one can reasonable assume that from a chemical point of view, a correct description of the valence orbital is more determining than of the core ones. As a consequence, more flexibility to assess properly for different molecular environment was achieved by Pople and coworkers[41,42] with the so-called split-valence basis sets of the type $C\text{-}v_1v_2G$. The core orbitals are described by one contracted GTO from C primitives, while two

contracted functions are used for the valence orbitals, developed over v_1 and v_2 primitives respectively, for instance as in the 6-31G basis set. One can add diffuse or polarisation functions for better flexibility and reach a more accurate description.[43]

2.8.2   Pseudopotentials

The fundamental concept of distinguishing core and valence electrons, illustrated by the structure of the periodic table, becomes even more crucial when dealing with heavy elements. The number of electrons increasing with the atomic number, systems containing one or more heavy atoms turn to be rather complex and computationally costly to treat, as a large number of basis functions are needed to describe properly the electron-electron interactions. Simplification of this problem is achieved by the introduction of pseudopotentials, in which only the valence electrons are explicitly treated, while the core electrons (and the nucleus), considered chemically inert but still influencing the reactivity of an atom, are modelled by a suitable effective (core) potential (ECP). Not only do they reduce the number of electrons, rendering the calculation computationally more feasible, but they also allow accounting for the relativistic effects arising from the high velocities of core electrons. Among the currently available pseudopotentials, the LANL2DZ combination of ECP from Hay and Wadt[44] and valence basis set (double zeta) have been used in this thesis.

2.9   Solvent effects: the polarizable continuum model

The vast majority of chemical reactions as well as experimental measurements take place in solutions. Molecular properties may be

greatly affected by the surrounding condensed phase and it is therefore of utmost importance to take properly into account these effects. The most straightforward approach to mimic a solution is to simply add explicitly the solvent molecules around the system investigated. However, as a single solvation shell would clearly be insufficient (absence of long-range effects), it is evident that the system constituted of the solute surrounded by explicit solvent molecules will quickly become enormous and computationally impossible to treat. To cope with this problem, one usually resorts to the use of implicit solvent models in which the solute is treated explicitly, while the solvent molecules are replaced by a continuous medium characterised by the properties of the solvent and surrounding the cavity occupied by the solute. Specific solute-solvent interactions can be accounted for by introducing solvent molecules in the explicit system to give a more reliable and accurate picture. Two types of continuum approaches are commonly used : dielectric PCM or conductor-like PCM. Implicit solvation has been extensively reviewed and further details are to be found in references 45 and 46. In this work, we have used the Polarizable Continuum Model in its integral equation formulation (IEFPCM) developed by Tomasi and co-workers[47], which falls into the category of dielectric continuum methods.

2.9.1   Basic   considerations   on   the   polarizable continuum solvation model

Within a continuum approach of solvation, the total Hamiltonian can be written as:

$$\hat{H}_{eff} = \hat{H}_{solute} + \hat{V}_{int} \tag{2.55}$$

with $\hat{H}_{solute}$ the Hamiltonian of the isolated solute and $\hat{V}_{int}$, the interaction term describing the solute-solvent interactions, which is a sum of different operators each accounting for a physical contribution.

Solvation is the process by which solvent molecules interact with the solute they surround and is characterised by the free energy of solvation ΔG_{sol} that corresponds to the change in free energy associated with the transfer of a molecule from the gas phase to the solvent environment. This free energy is partitioned into different contributions as follows:

$$\Delta G_{sol} = \Delta G_{cav} + \Delta G_{rep} + \Delta G_{disp} + \Delta G_{elec} \qquad (2.56)$$

and the interaction potential is equivalently a sum of operators each corresponding to a term of this partition.

Here, ΔG_{cav} is the cavitation free energy necessary to create a cavity for the solute in the continuous dielectric medium with an appropriate shape for the solute, which should reproduce as well as possible its molecular shape while excluding the solvent. Many definitions have been proposed for the cavity, reflecting compromises between accuracy and computational cost, as well as the diverse physical requirements for a given system. In the PCM model, it is defined as a superposition of interlocked spheres centred on the solute nuclei assigned with suitable radii. The formation energy is not related to the electronic properties of the solute but only depends on its geometry (which does not change in the BO approximation) and is evaluated independently according to Pierotti's modified formula (details can be found in ref. 48 and 49).

ΔG_{rep} is associated to solute-solvent repulsion interactions arising from electron exchange contributions while ΔG_{disp} accounts for the dispersion contribution owing to the interactions between instantaneous multipoles due to electrons correlated motion. These quantities are computed in the PCM model according to expressions from Amovilli and Mennucci[50].

Finally, the last contribution ΔG_{elec} is the free energy associated to the solute-solvent electrostatic interactions and is at the heart of the self-consistent reaction field (SCRF) procedure. Bringing in solution a solute characterised by a given charge distribution in the gas phase will cause a polarisation of the charges in the surrounding (dielectric) medium, inducing in turn an extra electric field, the so-called *reaction field*[51], in the vicinity of the solute, that will affect its electronic structure. The electrostatic problem relative to a charge distribution inside a cavity surrounded by a dielectric continuum can be solved by considering the Poisson equation and associated boundary conditions:

$$-\Delta V = 4\pi\rho_{sol} \qquad \textit{within the cavity}$$

$$-\varepsilon\Delta V = 0 \qquad \textit{outside the cavity}$$

$$V_{in} = V_{out} \qquad \textit{on the cavity surface}$$

$$\left(\frac{\partial V}{\partial n}\right)_{in} = \varepsilon\left(\frac{\partial V}{\partial n}\right)_{out} \qquad \textit{on the cavity surface}$$

with the total electrostatic potential V, sum of the electrostatic potential generated by the solute's charge distribution ρ_{sol} and the solvent reaction potential, ε the dielectric constant of the solvent, n the unit vector perpendicular to the cavity surface and pointing outwards, and the subscript *in* and *out* to indicate the regions inside and outside the cavity.

Several approaches are available to solve this electrostatic problem such as the apparent surface charge (ASC) method used in the PCM model. Here, the second contribution to the total electrostatic potential aforementioned is the interaction potential of the solute electrons with an apparent surface charge due to the polarisation of the dielectric medium spread on the cavity surface. In practice, this surface is divided into a number of finite triangular non-overlapping elements of known area, called *tesserae*, at the centre of which is placed a punctual charge. By

definition, there is a mutual polarisation between the solute and surrounding solvent, as the solvent reaction field acting upon the solute results from the polarisation it induces in the solvent, and the problem has to be solved iteratively (Poisson equation coupled to Schrödinger equation for the solute). Basically, starting from ρ_{sol}^0 the charge density of the solute without solvent, one can obtain a set of apparent charges by solving the electrostatic problem at the cavity surface. These charges are used to define the interaction potential in $\hat{H}_{eff}$ and solve the corresponding Schrödinger equation, leading to a new ρ_{sol}^1 for the solute that will be used to solve the new electrostatic problem, and so on, until self-consistency.

2.9.2   Dynamical aspects of solvation

When the solvated system is experiencing brutal changes such as the ones accompanying the vertical electronic transitions associated with UV-Vis optical absorption, it is necessary to extend the basic PCM model to account for the dynamics of solvation and properly describe time-dependent processes in solution.

Absorption is a very fast event that occurs on a time-scale of 10^{-15} seconds (see chapter 1), shorter than the associated solvent polarisation response, so that the dynamic effects commonly fall into two distinct time regimes known as the equilibrium (Eq) and non-equilibrium (NEq) solvation regime, in a picture analogous to the Franck-Condon principle presented in section 1.3 (Figure 2.1). The dielectric continuum response is generally approximated by a decomposition into a fast electronic component instantaneously in equilibrium with the excited state charge distribution of the solute, and a slow one, known as the inertial component, that remains in equilibrium with the ground state. In the non-equilibrium

regime, only the solvent electronic polarisation, i.e. the fast component, is in equilibrium with the solute excited state electron density while the inertial component remains equilibrated with the ground state; the equilibrium regime is reached provided a complete solvent relaxation is achieved (fast and slow components).
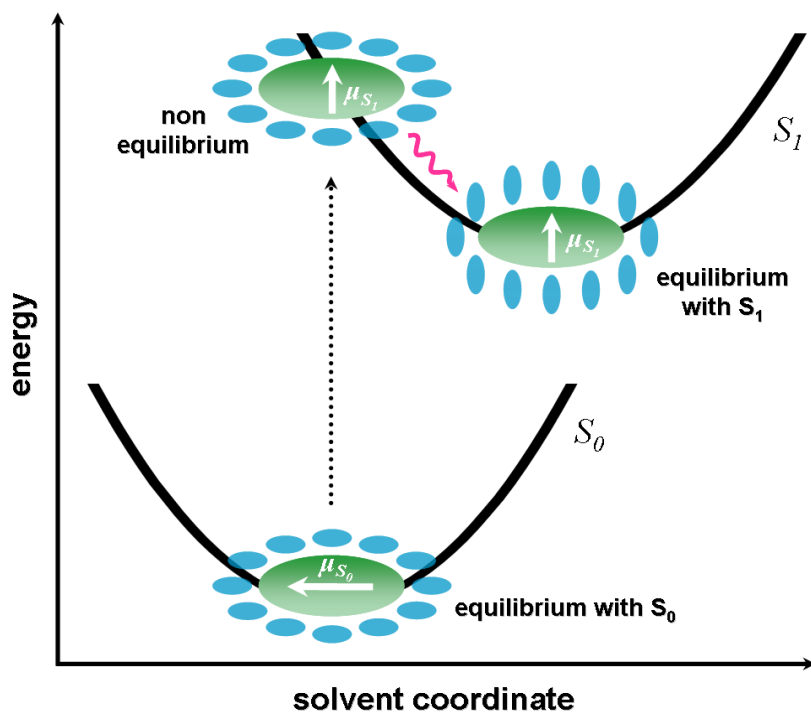
Figure 2.1 Solvation dynamics: schematic representation of the equilibrium and non-equilibrium regimes.

The description of excited states in solution can be done combining TD-DFT with PCM via two different approaches, the state-specific method[52] (SS) or the linear-response (LR). The latter consists in adding directly to the TD-DFT equations an additional PCM contribution and assessing the excitation energies without any explicit calculation of the excited state

electron density which, even if it allows to compute reasonably the solvent effect on the excited state energy, has to be compensated by a PCM correction. Although LR-PCM is the most widely used method to compute vertical energy excitations, one has to remember that in this approach, the solvent degrees of freedom are always equilibrated with the ground state density, preventing a proper treatment of the time-dependence of solvent effects and making it particularly not suitable for the description of light-emission (luminescence) processes. In contrast, the state-specific method gives the possibility of computing the solvent contribution to excitation energy according explicitly to the density of the state of interest considered in the relevant time regime involved in a given transition. For instance, in the absorption process, for which only the fast component is in equilibrium with the excited state density, the transition energy corresponds to the energy difference between the solute ground state equilibrium and excited state non equilibrium energies. For emission, the excited state equilibrium and ground state non equilibrium are considered instead. The determination of these quantities is basically achieved in a two-step procedure that starts with the calculation of the initial electronic state considering equilibrium solvation, after which slow and fast components of solvation charges are stored to be used in the second phase, i.e. the non-equilibrium solvation of the final state. SS-PCM approach obviously leads to more accurate energies regarding the emission process as it considers for the initial state the solvent reaction field relative to the excited state density.

2.10 Thermodynamic properties[53]

The partition function is the key to determine the thermodynamical properties of a system. In the following, we expose how these

thermodynamic quantities are calculated, assuming a set of non-interacting particles, along with other approximations mentioned when introduced.

Given that the energy of a molecule can be to a good approximation expressed as a sum of independent contributions from translational, rotational, vibration, and electronic motions, the partition function can be, in turn, written as a product of these contributions :

$$q = q_t q_r q_v q_e \tag{2.57}$$

The evaluation of each of these contributions allows to determine their respective entropy contributions, and thus the total entropy S of the system:

$$S = Nk_B + Nk_B \ln\left(\frac{q(V,T)}{N}\right) + Nk_B T \left(\frac{\partial \ln q}{\partial T}\right)_V \tag{2.58}$$

The expression used in the calculations is given in molar values and reads:

$$S = R\left[\ln(q_t q_r q_v q_e e) + T\left(\frac{\partial \ln q}{\partial T}\right)_V\right] \tag{2.59}$$

The internal thermal energy E and the heat capacity C_V are also obtained from the partition function:

$$\begin{aligned} E &= Nk_B T^2 \left(\frac{\partial \ln q}{\partial T}\right)_V \\ C_V &= \left(\frac{\partial E}{\partial T}\right)_{N,V} \end{aligned} \tag{2.60}$$

Several approximations are done in the calculation of the components of the partition function:

- the translation contribution q_t is calculated according to the following expression (ideal gas):

$$q_t = \left(\frac{2\pi m k_B T}{h^2}\right)^{3/2} \frac{k_B T}{P} \qquad (2.61)$$

- the following rotational partition function for nonlinear polyatomic molecules is used:

$$q_r = \frac{\pi^{1/2}}{\sigma_r}\left(\frac{T^{3/2}}{(\Theta_{r,x}\Theta_{r,y}\Theta_{r,z})^{1/2}}\right) \qquad (2.62)$$

- each vibrational mode provides a contribution to the vibrational partition function, except those with imaginary frequency:

$$q_v = \prod_K \frac{e^{-\Theta_{v,K}/2T}}{1 - e^{-\Theta_{v,K}/T}} \qquad (2.63)$$

with K=1,3N-6 and $\Theta_{v,K}$ the characteristic vibrational temperature of each mode. Zero point vibrational energy is also computed and included in the internal energy E.

- the energy of the ground state is set to be zero, while the *first and higher excited states are assumed to be inaccessible*, reducing the electronic partition function to the electronic multiplicity of the molecule:

$$q_e = \sum_i \omega_i e^{-\varepsilon_i/kT} = \omega_0 \qquad (2.64)$$

From the total entropy S_{tot} and the internal thermal energy E_{tot}, thermal corrections to enthalpy and Gibbs free energy are calculated:

$$\begin{aligned} H_{corr} &= E_{tot} + k_B T \\ G_{corr} &= H_{corr} - TS_{tot} \end{aligned} \qquad (2.65)$$

References

[1]   M. Planck, *Ann. Physik* **309**, 564 (1901).

[2]   A. Einstein, *Ann. Physik* **322**, 132 (1905).

[3]   L. de Broglie, *Ann. Physique* **3**, 22 (1925).

[4]   E. Schrödinger, *Ann. Physik* **79**, 361 (1926).

[5]   M. Born, J. R. Oppenheimer, *Ann. Physik* **84**, 457 (1927).

[6]   J. C. Slater, *Phys. Rev.* **34**, 1293 (1929).

[7]   A. Szabo, N. S. Ostlund, *Modern Quantum Chemistry: Introduction to Advanced Electronic Structure*, McGraw-Hill Publishing Company, New-York   (1989).

[8]   V. Fock, *Z. Phys.* **61**, 126 (1930).

[9]   D. R. Hartree, *Proc. R. Soc. (London)* **A113**, 621 (1928).

[10]   C. C. J Roothan, *Rev. Mod. Phys.* **23**, 69 (1951).

[11]   G. G. Hall, *Proc. Roy. Soc. (London)* **A205**, 541 (1951).

[12]   M. J. S. Dewar, E. G. Zoebisch, E. F. Healy, and J. J. P. Stewart, *J. Am. Chem. Soc.* **107**, 3902 (1985).

[13]   AMPAC 9, 1992-2008 Semichem, Inc. 12456 W 62nd Terrace - Suite D, Shawnee, KS 66216.

[14]   J. A. Pople, D. P. Santry, G. A. Segal, *J. Chem. Phys.* **43**, 129 (1965).

[15]   F. Jensen, *Introduction to Computational Chemsitry*, Wiley, Chichester (1999).

[16]   C. J. Cramer, *Essentials of computational chemistry*, Wiley, Chichester (2004).

[17]   L. H. Thomas, *Proc. Camb. Phil. Soc.* **23**, 542 (1927).

[18]   E. Fermi, *Z. Phys.* **48**, 73 (1928).

[19]   P. A. M. Dirac, *Proc. Camb. Phil. Soc.* **26**, 376 (1930).

[20]   F. Bloch, *Z. Phys.* **57**, 545 (1929).

[21]   E. Teller, *Rev. Mod. Phys.* **34**, 627 (1962).

[22]   P. Hohenberg and W. Kohn, *Phys. Rev.* **136**, B864 (1964).

[23]   W. Kohn, L. J. Sham, *Phys. Rev.* **140**, A1133 (1965).

[24]   L. A. Curtiss, K. Raghavarachari, G. W. Trucks, J. A. Pople, *J. Chem. Phys.* **94**, 7221 (1985).

[25]   J. P. Perdew and K. Schmidt, *Density Functional Theory and Its Applications to Materials*, edited by V. E. Van Doren, C. Van Alsenoy, and P. Geerlings, *AIP Conference Proceedings*, **577**, 1 (2001).

[26]   D. M. Ceperley and B. J. Alder, *Phys. Rev. Lett.* **45**, 566 (1980).

[27]   S.H. Vosko, L. Wilk, and M. Nusair, *Can. J. Phys.* **58**, 1200 (1980).

[28]   J. P. Perdew, Y. Wang, *Phys. Rev. B* **45**, 13244 (1992).

[29]   A. D. Becke, *Phys. Rev. A*, **38**, 3098 (1988).

[30]   C. Lee, W. Yang, and R. G. Parr, *Phys. Rev. B*, **37**, 785 (1988).

[31]   J. P. Perdew, in *Electronic Structure of Solids '91*, Ed. P. Ziesche and H. Eschrig (Akademie Verlag, Berlin, 1991) 11.

[32]   J. P. Perdew, K. Burke, and M. Ernzerhof, *Phys. Rev. Lett.*, **77**, 3865 (1996).

[33]   A.D. Becke, *Phys. Rev. A* **33**, 2786 (1986).

[34]   C. W. Bauschlicher, *Chem. Phys. Lett.* **246**, 40 (1995).

[35]   C. Adamo and V. Barone *J. Chem. Phys.* **110**, 6158 (1999).

[36]   T. Yanai, D. Tew, N. Handy, *Chem. Phys. Lett.* **393**, 51 (2004).

[37]   E. Runge and E. K. U. Gross, *Phys. Rev. Lett.* **52**, 997 (1984).

[38]   E. K. U. Gross and W. Kohn, *Phys. Rev. Lett.* **55**, 2850 (1985).

[39]   J. C. Slater, *Phys. Rev.* **36**, 57 (1930).

[40]   S. F. Boys, *Proc. R. Soc. London* **A200**, 542 (1950).

[41]   J. S. Binkley, J. A. Pople, W. J. Hehre, *J. Am. Chem. Soc.* **102**, 939 (1980).

[42] M. S. Gordon, J. S. Binkley, J. A. Pople, W. J. Pietro, W. J. Hehre, *J. Am. Chem. Soc* **104**, 2797 (1982).

[43] M. J. Frisch, J. A. Pople, J. S. Binkley, *J. Chem. Phys.* **80**, 3265 (1984).

[44] W. R. Wadt, P. J. Hay, *J. Chem. Phys.* **82**, 270 / 284 / 299 (1985).

[45] J. Tomasi, B. Mennucci and R. Cammi, *Chem. Rev.* **105**, 2999 (2005).

[46] C. J. Cramer and D. G. Truhlar, *Chem. Rev.* **99**, 2161 (1999).

[47] J. Tomasi, B. Mennuci, E. Cancès, *J. Mol. Struct. (Theochem)* **464**, 211 (1999).

[48] R. A. Pierotti, *Chem. Rev.* **76**, 712 (1976).

[49] J. Langlet, P. Claverie, J. Caillet, and A. Pullman, *J. Phys. Chem.* **92**, 1617 (1988).

[50] C. Amovilli and B. Mennucci, *J. Phys. Chem.* **101**, 1051 (1997).

[51] L. Onsager, *J. Am. Chem. Soc.* **58**, 1486 (1936).

[52] R. Improta, V. Barone, G. Scalmani and M. J. Frisch, *J. Chem. Phys.* **125**, 054103: 1-9 (2006).

[53] *Thermochemistry in Gaussian (white paper)*, J. W. Ochterski. http://www.gaussian.com/g_whitepap/thermo.htm

Chapter 3

Tailoring the optical and electronic properties of BODIPY dyes

BODIPY derivatives have been synthesised and characterised in terms of crystallographic structure and spectroscopic properties as a function of solvent in the group of Prof. Noël Boens at the Laboratory of Photochemistry and Spectroscopy of the Katholieke Universiteit Leuven. Our contribution consists in a quantum-chemical study performed to unravel the relationships between the molecular structure and the optical properties for series of BODIPY derivatives.
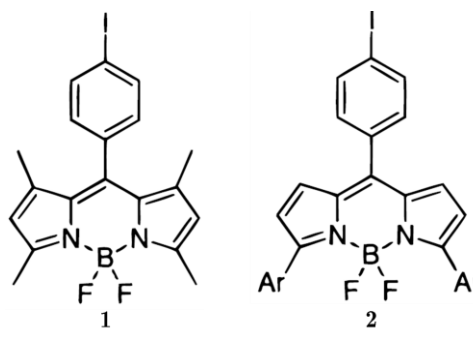
D iscovered in the late 60's and extensively studied in the past three decades, boron-dipyrromethene dyes, hereafter abbreviated to BODIPY, have become a very popular class of chromophores and are nowadays among the most versatile dyes in use (cf. Chapter 1). Combining strong UV absorption and sharp fluorescence emission with high extinction coefficient and high fluorescence quantum yield, they constitute an ideal platform for dye development owing to the numerous possibilities to modify the BODIPY core (Figure 3.1). Unsubstituted BODIPY shows absorption and emission around 500 nm[1,2,3], and attaching suitably chosen substituents at the pyrrole ring and/or central *meso*-position and/or the boron atom can lead to large changes in the spectra. Moreover, they tend to be relatively insensitive to the environment properties (solvent, pH) and are stable in physiological conditions. All these very attractive features explain the intensive investigations on the tuning of their optical properties to develop new better-performing derivatives for given applications.
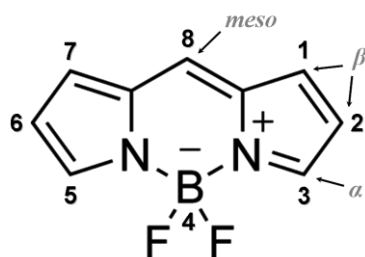
Figure 3.1 Structure and IUPAC numbering of the BODIPY core.

In the quest for NIR absorbing and fluorescent dyes with high performance, BODIPY derivatives constitute attractive potential candidates and much effort has been devoted to the modulation of their

spectroscopic properties, notably in shifting their absorption and emission maxima. Extension of the π-conjugated system is the most straightforward and commonly used method to obtain BODIPY dyes with bathochromically shifted absorption and emission spectra. In particular, appropriate functionalisation by aryl groups at the 3,5-positions has been shown to significantly shift both the absorption and emission maxima to longer wavelengths (Figure 3.2)[4,5,6]. Electron-donating groups (e.g., methoxy groups) provide an extra red-shift, as can be seen comparing **2a** and **2c**.
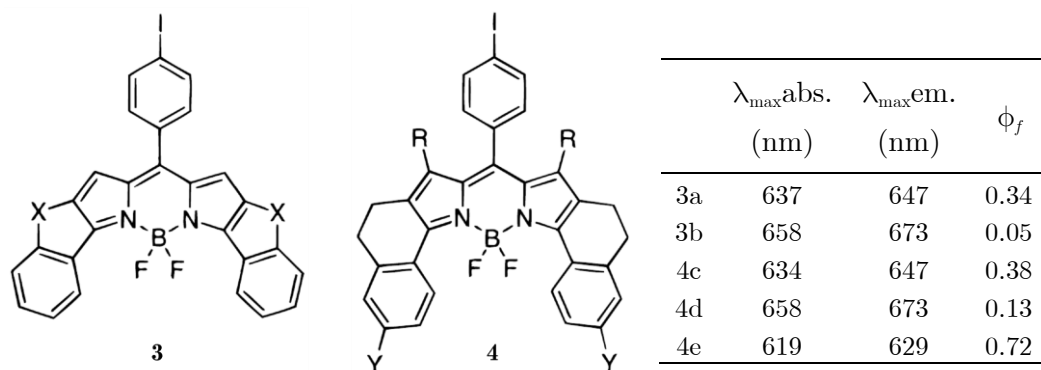

	λ_{max}abs. (nm)	λ_{max}em. (nm)	ϕ_f
1	500	510	0.64
2a	555	588	0.20
2b	542	607	0.38
2c	582	626	0.42
2d	555	590	0.22
2e	545	598	0.08

Figure 3.2 3,5-disubstituted BODIPY derivatives, with *Ar : a.Ph, b.1-Naph, c.4-MeOC$_6$H$_4$, d.4-FC$_6$H$_4$, e.2-MeOC$_6$H$_4$ (in CHCl$_3$).* ϕ_f is the fluorescence quantum yield.

However, although bathochromic shifts of more than 100 nm can be achieved, these derivatives suffer from low to moderate fluorescence quantum yields due the possible rotation of the substituents, which results in efficient non-radiative decay pathways. The strategy employed to circumvent this drawback and enhance the fluorescence consists in rigidifying the structure of the system, as described by Burgess et al.[7].

The more rigid BODIPY derivatives they reported (Figure 3.3), in which the free rotation of 3,5 substituents is prevented, exhibit absorption and emission at longer wavelengths as well as generally higher quantum yields (except for 3b). In this context, we investigated a series of BODIPY dyes with increasing rigidity caused by benzofuran ring formation, as well as related ring-fused BODIPY dyes (section 3.1).

	λ_{max}abs. (nm)	λ_{max}em. (nm)	ϕ_f
3a	637	647	0.34
3b	658	673	0.05
4c	634	647	0.38
4d	658	673	0.13
4e	619	629	0.72

Figure 3.3 Rigidified BODIPY derivatives, with X : *a.O, b.S, c.Y=R=H, d.R=H;Y=OMe, e.R=Me;Y=H (in CHCl₃).*

Aromatic ring-fusion has proven to be an efficient strategy in the search for improvement as it allows an extension of the conjugation leaving open the possibility for further functionalisation at the *meso* and 3,5-positions[8]. Further steric constraints for improved fluorescence can be achieved via methyl substitution at the 1,7-positions to lock the *meso*-substituent. Apart from the possible modulation of the quantum yield, the *meso*-substitution actually does not directly affect the absorption and emission maxima and can thus be performed to impart another function to the molecule. It has given rise to a large variety of compounds from redox active molecules to pH probes as well as metal chelators[9].

Another route towards NIR dyes consists in replacing the carbon atom in *meso*- position by a nitrogen atom to obtain the aza-BODIPY analogues, which can exhibit very large bathochromic shifts compared to their BODIPY counterparts. Their remarkable spectral properties can be successfully tuned by the same kind of modifications used on the BODIPY core, with a very strong dependence of the absorption and emission maxima on the nature of the substitution[10,11,12,13].

3.1 Conformational restrictions

Together with extended π-conjugation, the rigidification of the BODIPY structure, via for instance annulation, i.e., the building of homo- of heterocyclic rings onto the aromatic rings attached to the BODIPY core, allows for further expansion of the conjugated ring system and constitutes an efficient strategy to obtain spectral displacements towards longer wavelengths together with an enhancement of the fluorescence.

3.1.1 Heterocyclic ring annulation

Many rigid BODIPY dyes, decorated by various substituents, have already been reported in the literature[7,8,14,15,16,17,18,19]. An alternative synthetic strategy, proposed by V. Leen et al., has proven to be a powerful and facile method for the formation of ring-annulated BODIPY dyes with bathochromically-shifted visible absorption and fluorescence spectra with considerably higher molar absorption coefficients ($\varepsilon(\lambda)$), and fluorescence quantum yields (ϕ_f) values.

We investigated three BODIPY derivatives prepared according to the aforementioned synthetic route and characterised by increasing conformational restrictions along the **1 → 2 → 3** series (Figure 3.4).
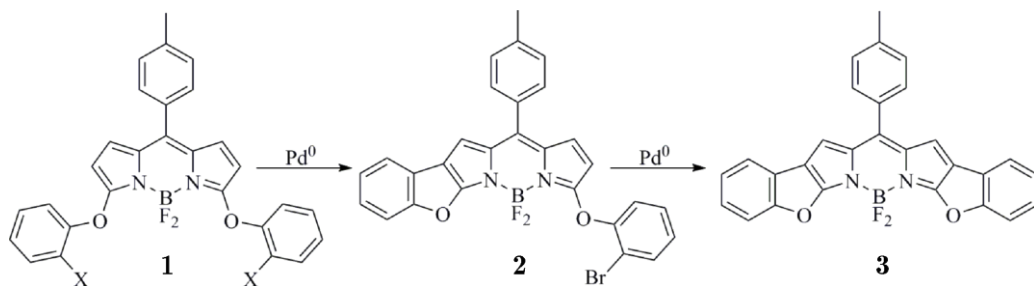
Figure 3.4 Structures of the BODIPY dyes series with reaction conditions of transition metal catalyzed annulation.

3.1.1.1 Experimental characterisation

Crystallographic structure

As shown in Figure 3.5, the BODIPY ring system of **2** is remarkably planar, and the benzofuran fragment also lies in the BODIPY plane. The tolyl group at the *meso*-position makes an angle of 62.1° with the BODIPY plane, which is in the range of most BODIPY derivatives (40°-90°), while the 2-bromophenoxy substituent is tilted relative to the same plane, with a dihedral angle of 58.8°. In dye **3**, the entire aromatic system is flat: the deviation from planarity for the boron atom, when considering the entire aromatic system is 0.2 Å. The *p*-tolyl group makes an angle of 55.4° with the BODIPY core.
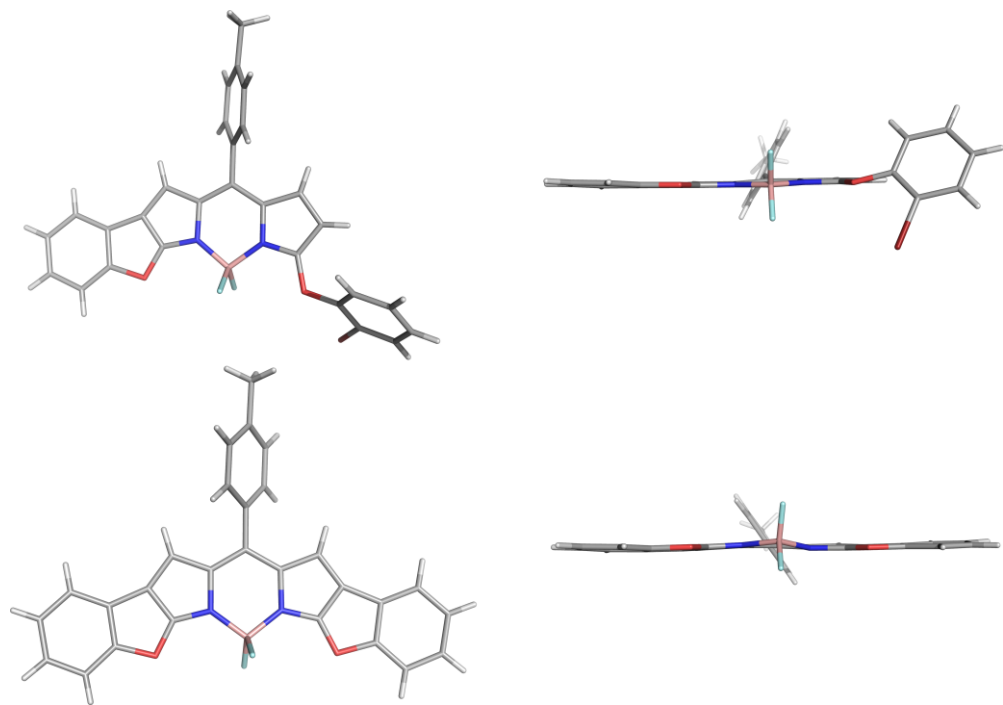
Figure 3.5 Stick representation of compound **2** (top) and compound **3** (bottom). To illustrate the planarity of the ring systems, a side view is placed at the right. Created with PyMol, (DeLano, W.L. The PyMOL Molecular Graphics System (2002) on http://www.pymol.org).

Spectroscopic properties

Dyes **1**–**3** are strongly coloured solids with a metallic luster. They form intensely coloured solutions with a bright fluorescence when irradiated (Figure 3.6). Compound **1** displays the typical absorption features of classic BODIPY dyes in all solvents studied, that is, a narrow absorption band with a maximum in the 511-518 nm range, irrespective of the solvent employed. This absorption band is assigned to the $S_1 \leftarrow S_0$ transition, while an additional, considerably weaker, broad absorption

band, observed at the short wavelength side, is attributed to the $S_2 \leftarrow S_0$ transition.
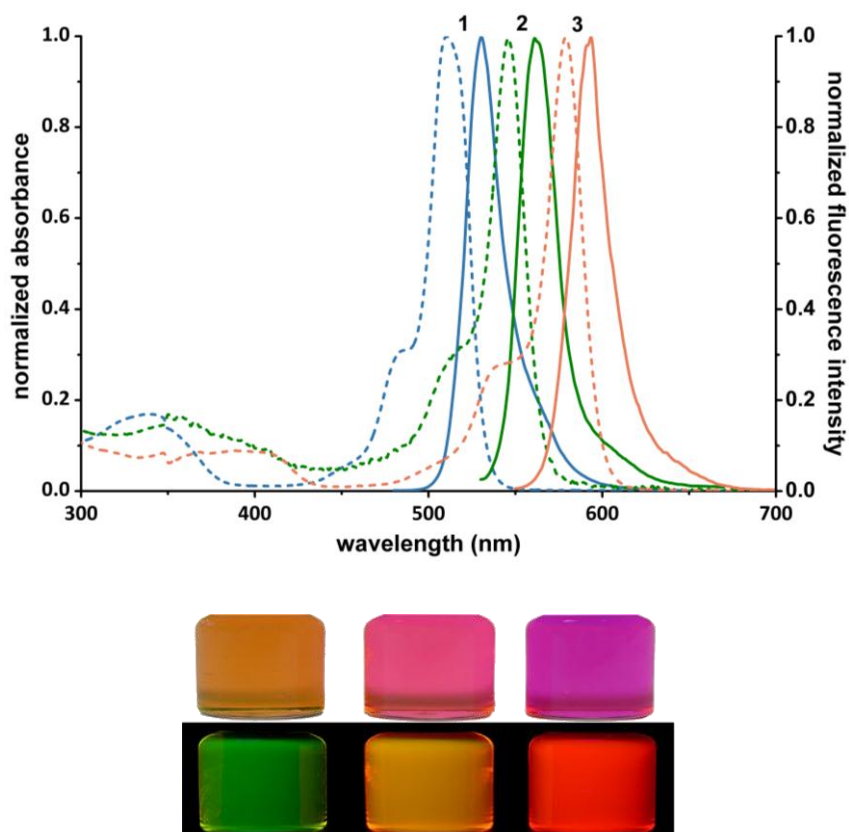
Figure 3.6 Normalised absorption (dashed lines) and fluorescence emission (full lines) profiles of **1** (blue), **2** (green) and **3** (orange) in diethyl ether. Absorption (upper row) and fluorescence (lower row) emission colours of **1–3** (from left to right) in diethyl ether.

The main absorption band of **1** is hardly affected by solvent polarity: the maximum being slightly blue-shifted when the solvent is changed from

toluene (518 nm) to acetonitrile or diethyl ether (511 nm), which is consistent with the general behaviour of BODIPY chromophores.[9] The same behaviour is observed for **2** and **3** and the fact that the absorption band positions of **1**–**3** do not show any particular trend as a function of solvent polarity suggests that the absorbing state of the dyes is weakly dipolar. The emission spectra also show the typical features of BODIPY: i.e., a narrow, slightly Stokes-shifted band that is a mirror image of the absorption and blue-shifts with decreasing solvent polarisability (from 537 nm in CCl_4 to 528 nm in methanol). The observation that the emission band positions of **1-3** do not exhibit any distinct trend as a function of solvent polarity implies that emission occurs from the weakly dipolar, relaxed Franck-Condon excited state of the dyes.

Table 3.1 Spectroscopic and photophysical properties of **1-3** in toluene.

	λ_{max} abs. (nm)	λ_{max} em. (nm)	$\Delta\bar{\nu}$ (cm^{-1})	ε_{max} $(L.mol^{-1}.cm^{-1})$	f	ϕ_f
1	518	536	648	35 000	0.248	0.47
2	553	569	508	42 000	0.390	0.48
3	587	602	424	155 000	0.802	0.58

Introduction of the benzofuran ring in **2** causes a large bathochromic shift in both the absorption and emission maxima, by 35 and 33 nm, respectively, compared to **1** (Table 3.1). The absorption and emission maxima of the most rigid structure **3** are further red-shifted by approximately 30 nm compared with **2**. The progressively more extended planarity of the chromophore in the series **1** → **2** → **3** accounts for the increasing bathochromic shifts of λ_{abs}(max) and λ_{em}(max). The conformational restriction that results in locking the bond rotation in the

ring-fused systems explains the noticeably higher quantum yields ϕ_f of **3**. Progressive reduction of the flexibility of the chromophore is also reflected by the considerably higher ε_{max} and corresponding f values. The oscillator strength f is calculated according to the following equation[20]:

$$f = \frac{4.32 \times 10^{-9}}{n} \int \varepsilon(\bar{\nu}) d\bar{\nu}$$ (3.1)

where n is the solvent index of refraction and $\bar{\nu}$ is the wavenumber (in cm^{-1}).

3.1.1.2   Quantum chemical calculations

For all compounds investigated, the ground-state geometry optimisation was first performed at the AM1[21] semi-empirical level, using the commercial package AMPAC 8.15.9[22]. These geometries were subsequently used as input for calculations at the AM1/SCI level (in the gas phase) to compute excited-state properties, including transition energies (Table 3.2), dipole moments and densities, with an active space of 60 molecular orbitals.

Compounds 1-3

To understand the effect of conformational constraints on the optical properties of BODIPY dyes, we performed calculations on molecules **1-3**. Starting from **1**, the structure of the system has been increasingly constrained by the introduction of benzofuran rings instead of bromophenoxy groups (**1** → **2** → **3**, see Figure 3.4), leading to a completely planar structure in compound **3**. This increase in rigidity results in an overall bathochromic shift of the absorption and emission maxima. A red shift of ~18 nm (~0.08 eV) is computed when one

bromophenoxy group is replaced by a benzofuran ring (in **2**). When a second benzofuran ring is introduced (in **3**), the bathochromic shift reaches ~24 nm (~0.10 eV) in comparison to **2**. The calculations thus reproduce well the observed spectral shifts, even though the AM1/SCI transition energies are systematically overestimated. The computed transitions are of HOMO→LUMO nature and the spectral displacement when going from **1** to **3** can be traced back to the changes in the shape of these orbitals with the geometrical constraints (Figure 3.7).
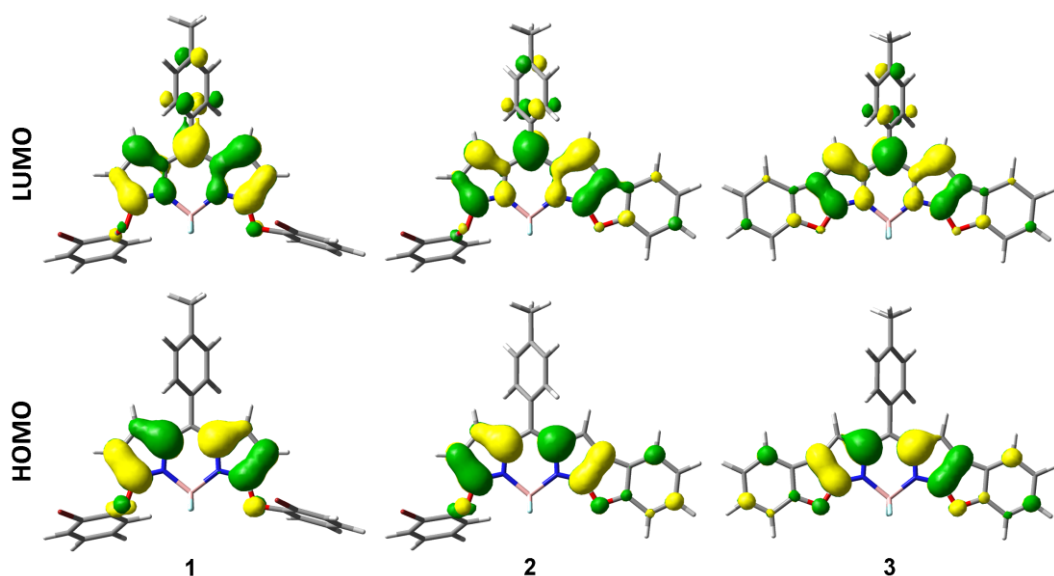
Figure 3.7 Graphical representations of the frontier orbitals of **1-3**.

Differences between the frontier orbitals of the three compounds are mostly noticeable in the case of the HOMO. For **1**, the HOMO has no weight on the substituents (bromophenoxy rings). If the bromophenoxy groups of **1** are replaced by either one or two benzofuran rings in **2** and **3**,

respectively, the HOMO shows significant contributions on the substituent moiety thereby explaining the predicted and measured bathochromic and hyperchromic shifts. Changes in the LUMO, although less pronounced, are along the same line.

The experimental oscillator strengths, f, extracted from equation 3.1, are in line with our theoretical findings: the oscillator strength f increases when the 3,5-substituents are frozen in a more rigid structure, as a result of the extended π-delocalisation.

Table 3.2 Calculated (AM1/SCI) (left) and measured (right) photophysical properties of compounds **1-7**. To convert the theoretical value of the oscillator strength f (for the gas phase) to values in a solvent with refractive index n, one has to multiply the theoretical f value by $n\left(\dfrac{n^2+2}{3}\right)^2$.[23]

	theoretical values (in the gas phase)			experimental values		
	transition energy (eV)	transition wavelength (nm)	oscillator strength f	transition energy (eV)	transition wavelength (nm)	oscillator strength f
1	2.382	521	0.7515	2.396[a]	518[a]	0.248[a]
2	2.303	538	0.8525	2.245[a]	553[a]	0.390[a]
3	2.206	562	1.0182	2.114[a]	587[a]	0.802[a]
4	2.069	599	0.7912	1.949[b]	637[b]	/
5	2.090	593	0.8995	1.933[c]	642[c]	/
6	2.152	576	0.8544	2.144[b]	579[b]	/
7	2.023	613	1.2316	1.904[b]	652[b]	/

a) Data in toluene. b) Data in chloroform. c) Data in cyclohexane.

The properties of these dyes can be compared to those of conformationally restricted BODIPY derivatives published in the literature (Figure 3.8 and Table 3.3)[4,7,16,17].
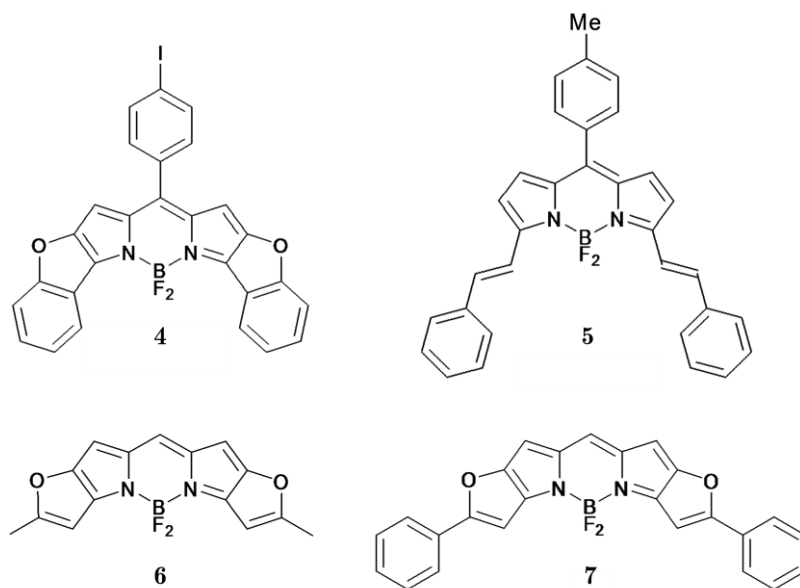
Figure 3.8 Chemical structures of (ring-fused) BODIPY dyes from the literature discussed here.

Table 3.3 Spectroscopic and photophysical properties of **4-7** in toluene.

	λ_{max} abs. (nm)	λ_{max} em. (nm)	$\Delta\bar{\nu}$ (cm^{-1})	ε_{max} (L.mol^{-1}.cm^{-1})	ϕ_f	solvent
4[7]	637	647	243	151 000	0.34	CHCl$_3$
5[4]	630	642	297	138 000	0.96	cyclohexan
6[16]	579	583	118	202 000	0.96	CHCl$_3$
7[17]	652	661	209	314 000	0.96	CHCl$_3$

Compound 3 and 4

It is instructive to compare **3** with the symmetrically constrained dye **4** of Burgess and co-workers, which only differs by the position of the benzofuran rings: compound **3** presents 3,5-dioxy benzofuran rings whereas **4** features 2,6-dioxy benzofuran rings (Figure 3.8). Experimentally, **4** has been found to absorb and emit light ~50 nm more to the red relative to dye **3** (Table 3.3), reflecting its improved conjugation. Theoretical transition wavelengths were simulated and frontier orbitals as well as transition densities analyzed to confirm this observation. An absorption maximum located at 562 nm is computed for **3**, which is 25 nm less than the experimental result (587 nm). in the case of **4**, the difference with the experimental transition is even bigger with a transition calculated at 599 nm, 38 nm less than the measured one. Again, although the theoretical values of the absorption maxima and of the spectral shifts are underestimated for both compounds, the qualitative trend is nicely reproduced by the calculations, with **4** showing a calculated bathochromic shift of ~37 nm (~0.14 eV) compared to **3** (against the experimental value of ~50 nm).
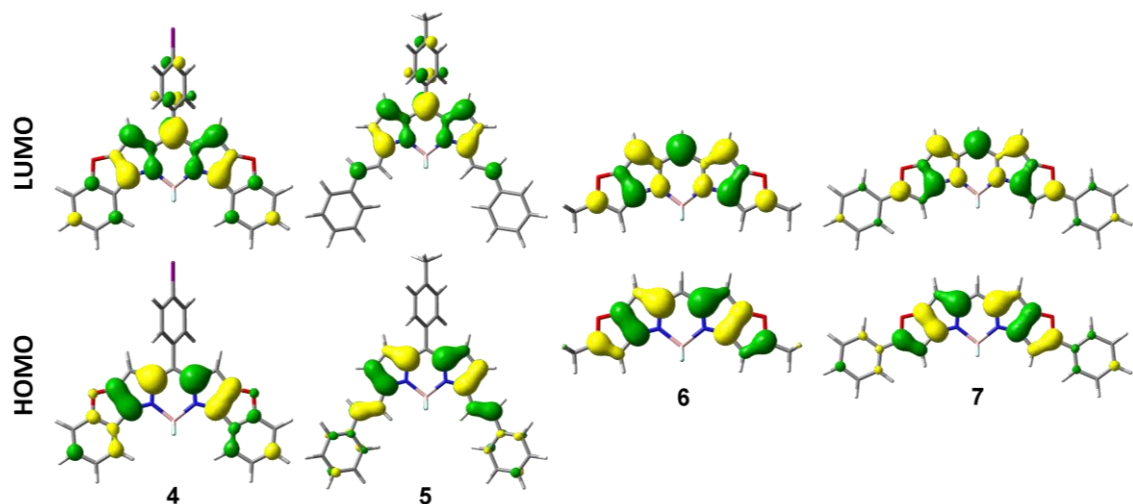
Figure 3.9 Graphical representations of the frontier orbitals of **4**-**7**.

When comparing the frontier orbitals, a major visible difference can be noticed for the LUMO: in **3**, the LUMO has a vanishingly small weight on the benzofuran rings, while these contribute more significantly to the LUMO wavefunction in **4** (Figure 3.9). This is confirmed by the computed transition densities for the lowest electronic excitation, which provide a local map for the transition dipole and the excited-state localisation (Figure 3.10). The transition density is almost completely localised on the BODIPY core in **3**, but one can see small but non-negligible contributions on the benzofuran rings in **4**, consistent with the extended conjugation. In a simple valence bond picture, the phenyl units in **4** are connected to the central pyrrole rings of the BODIPY core in '*N*-β' positions, while they are grafted in '*N*-α' positions for **3**, thereby explaining the more efficient delocalisation in **4**.

Compound **5-7**

The Keio Fluors (KFL) **6** and **7** of Suzuki et al.[16] have, like **4**, 2,6-dioxy furan rings, but differ from each other in that a single methyl is added on the furan rings of **6** where phenyl rings are present in **7**. The latter can be regarded as a 3,5-distyryl substituted BODIPY such as **5**, but with oxygen atom bridge linkers that preclude free rotation of the ethenyl fragments. Note that the absence of a *meso*-substituent and hence limited conformational flexibility in **6** and **7**, which exhibit extremely high ε_{max} and very small Stokes Shift $\Delta\bar{\nu}$, leads to very high quantum yields ϕ_f.

Except for **6**, for which the computed absorption maximum is in very good agreement with the experimental value as only underestimated by ~3 nm, the computed transition wavelengths for **5** and **7** are underestimated by a larger amount, of about 40 nm, compared to the experimental results (652 and 630 nm, respectively). However, the increase in the oscillator strength associated to the presence of O-linked bridges to prevent rotation of the 3,5-distyryl substituents is in agreement with the observed experimental trend.
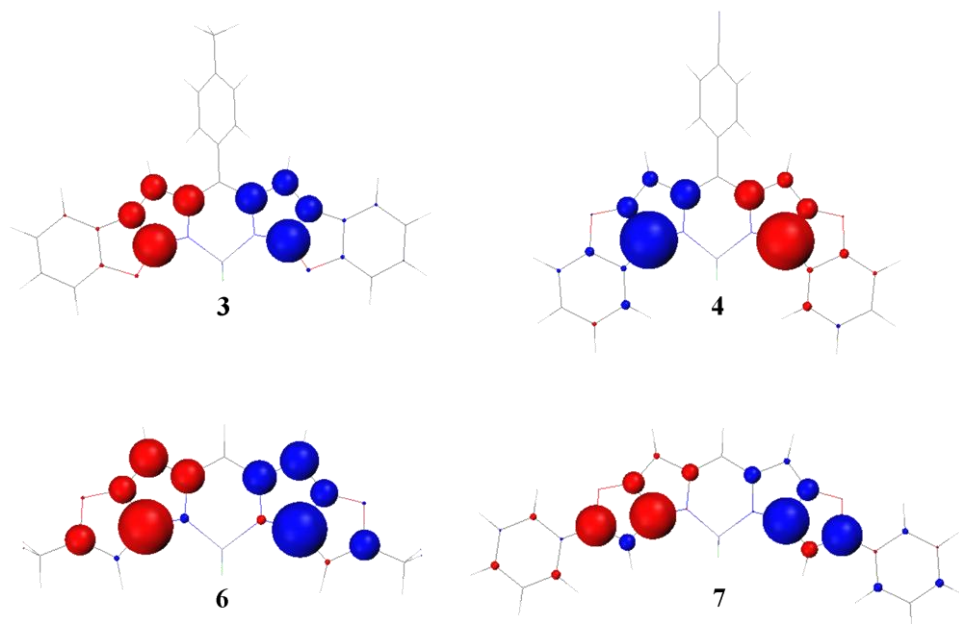
Figure 3.10 Transition densities of compounds **3**, **4**, **6** and **7** (electron density is shifting from the red to the blue region). Atomic transition densities are given as: $q_m = \sum_K C_K C_m^a C_m^b$ where C_m^a and C_m^b are the LCAO coefficients on site m in the molecular orbitals a and b involved in the singly excited configuration K.

We compare the frontier orbitals of these compounds, as well as the transitions densities, in Figure 3.10, in order to evaluate the impact of the nature of the substituent on the furan rings (**6** and **7**) and disentangle the influence of the presence of O-linked bridges (**5** against **6** and **7**).

There are no obvious differences between the HOMO and LUMO orbitals of **5** and **6**. It thus appears that extending the conjugation from **6** to **5** through substitutions at the 3,5 positions of the BODIPY core is not in this case very effective in raising the oscillator strength and/or in lowering

the excitation energy. We attribute this to the fact that the extension of the π-system then occurs along a direction that is almost perpendicular to the polarisation of the lowest electronic excitation. By far, a much more dramatic improvement is seen in **7**. Although the frontier molecular orbitals of **6** and **7** look very similar and are in both cases mostly confined on the central BODIPY core, the transition densities extend significantly over the external phenyl rings in **7** (Figure 3.10), which explains the largest oscillator strength computed for that compound. This effect arises from multi-configurational mixing of the HOMO–LUMO excitation with electronic configurations involving deeper molecular orbitals with large weights on the outer phenyl rings.

3.1.2   Homocyclic ring annulation

Just as annulation with an hetero atom has been shown to give BODIPY derivatives with bathochromically shifted absorption and emission maxima, fusing the BODIPY core to rigid π-conjugated carbocycles can also lead to NIR emitting dyes. Both symmetrically[5] and asymmetrically[24] ring-fused systems have been reported. To understand the spectral behaviour and associated photophysical properties of such dyes depending on the symmetry of the substitution as well as on the presence or absence of conformational constraints, we investigated the series of BODIPY derivatives presented in Figure 3.11. The **8-11"u"** derivatives are the equivalent of compounds **8-11** with no rotational restriction around the single bond at position 3.
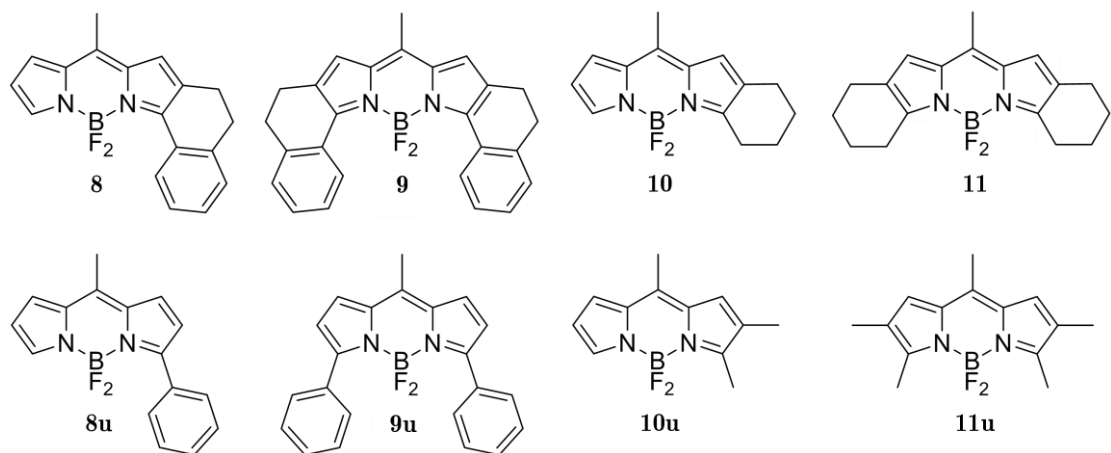
Figure 3.11 Chemical structures of the BODIPY derivatives studied.

Compounds **9(u), 11** and **11u** have been described in ref. 25, 26 and 27, respectively, while **8** and **10** have been newly synthesised by the group at KU Leuven. **8u** and **10u** have not been reported yet.

Experimental observations

Compounds **8** and **9** display the typical absorption features of classic BODIPY dyes, with a narrow first absorption band assigned to $S_0 \rightarrow S_1$, transition which is red-shifted with increasing solvent polarity, and an additional, considerably weaker, broad absorption band around 350 nm, attributed to the $S_0 \rightarrow S_2$ transition. The two systems also show the characteristic emission features of BODIPY, i.e., a narrow slightly Stokes-shifted band with a mirror image shape. Data for **8-11** measured in acetonitrile are compiled in Table 3.4.

Table 3.4 Spectroscopic and photophysical properties of **8-11** in acetonitrile.

	λ_{max} abs. (nm)	λ_{max} em. (nm)	$\Delta\overline{\nu}$ (cm⁻¹)	ϕ_f
8	546	560	458	0.72
9	613	625	313	0.91
10	508	520	454	0.83
11	534	543	310	0.76

Computational method

All calculations were performed with the Gaussian (G09) program package[28]. Density functional theory (DFT) was used with the CAM-B3LYP[29] hybrid functional and 6-31G* basis set for geometry optimisations. From these equilibrium structures, UV-Vis absorption and emission spectra were computed in the framework of time-dependent density functional theory (TD-DFT), with the same functional and the same basis set. To take the solvent effect into account (acetonitrile), the polarised continuum model (IEFPCM formalism[30]) was adopted using linear response[31] (LR) or state-specific[32,33] (SS) approaches available in G09.

Optical properties computed with the LR and SS aproaches

Absorption and emission wavelengths/energies of systems **8**, **9**, **10** and **11** and their unconstrained counterparts, calculated with the LR-PCM and SS-PCM approaches, are compiled in Table 3.5 and Table 3.6, respectively.

Table 3.5 Computed wavelengths/energies of the first absorption and emission vertical transitions with the LR-PCM approach and associated vertical transition energy differences for **8-11** and their corresponding unrestricted forms.

	absorption			emission			$\Delta E_{abs/em}$
	transition energy (eV)	transition wavelength (nm)	oscillator strength f	transition energy (eV)	transition wavelength (nm)	oscillator strength f	energy (eV)
8	2.74	452	0.7786	2.34	530	0.96	0.40
8u	2.88	430	0.7002	2.45	505	0.89	0.43
9	2.42	511	0.8509	2.07	599	1.03	0.35
9u	2.71	457	0.7600	2.25	552	0.96	0.46
10	2.98	415	0.6320	2.62	473	0.76	0.36
10u	3.01	412	0.5859	2.64	469	0.74	0.37
11	2.81	440	0.7084	2.52	493	0.84	0.29
11u	2.85	435	0.6226	2.54	488	0.76	0.31

Table 3.6 Computed wavelengths/energies of the first absorption and emission vertical transitions with the SS-PCM approach and associated vertical transition energy differences $E_{abs/em}$ for **8-11** and their corresponding unrestricted forms[a].

|	absorption		emission		$\Delta E_{abs/em}$		Stokes shift
	transition energy (eV)	transition wavelength (nm)	transition energy (eV)	transition wavelength (nm)	(eV)	(cm^{-1})	(cm^{-1})
8	2.89	430	2.70	459	0.19	1465	169
8u	3.03	409	2.83	438	0.20	1638	181
9	2.55	487	2.40	517	0.15	1199	138
9u	2.85	436	2.59	479	0.26	2068	128
10	3.12	397	2.97	418	0.15	1245	209
10u	3.15	394	2.99	415	0.16	1245	226
11	2.94	422	2.83	438	0.11	836	151
11u	2.97	417	2.86	433	0.11	879	155

[a]The Stokes shifts are based on solvent relaxation (see below).

Inner- and outer-sphere relaxations occur upon electronic transition from the ground state to the singlet excited state of the dye (in absorption) and vice versa (in emission). The intramolecular relaxation is substantial, it involves high-frequency vibrations and largely contributes to the energy difference between vertical transitions. It manifests itself as a vibrational progression in the experimental spectra and has not been modelled further here. We have rather focused on the Stokes shift between the 0-0 energy transitions in absorption and emission that mostly originates from solvent relaxation. Thus, we have computed the vertical transition energies in absorption and emission successively based on the solvent reaction fields produced in the ground state and the lowest singlet excited state (and using the ground- or excited-state optimised geometry).

3.1.2.1 Symmetry of the substitution

The computed electronic absorption spectra of **8** and **9** both present a low-lying HOMO→LUMO transition band, at 430 and 487 nm, respectively (Table 3.6). Although these values are underestimated with respect to the experimental results (Table 3.4 and Figure 3.12), the red-shift measured upon disubstitution of the BODIPY core, namely, when going from **8** to **9**, is properly reproduced with a calculated value of ~57 nm (compared to a measured value of ~67 nm). The origin of the bathochromic shift can be better appreciated by looking at the frontier orbitals involved in the transitions (Figure 3.12). The rigidisation of two 3,5-phenyl groups in **9** is accompanied by a more extended conjugation, illustrated by the clear delocalisation of both HOMO and LUMO over the two phenyl rings, which accounts for the observed spectral displacements.
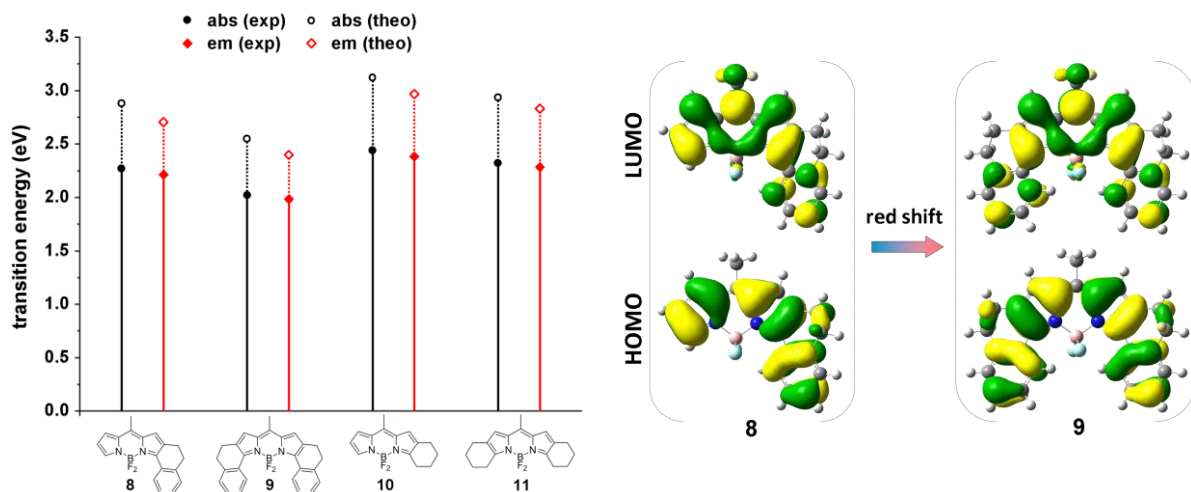
Figure 3.12 Experimental (solid lines) and theoretical (dashed lines) vertical transition energies for absorption and emission of **8-11** (left). Graphical representations of the frontier orbitals of **8** and **9** (right).

Regarding the fluorescence emission process, the computed values of the transition wavelengths are again underestimated. However, the general trends are well reproduced. Namely, the vertical transition from the relaxed excited-state geometry shows a large red-shift of about 58 nm for **9** compared to **8**, in line with the experimental data (bathochromic shift of 65 nm).

As expected and measured in solution, we compute blue-shifted absorption and emission transitions for **10** and **11** (compared to **8** and **9**), the latter, in which two cyclohexane rings have been fused to the pyrrole fragments at the α,β-positions, presenting the least hypsochromically shifted band. The disubstitution of the BODIPY core (**10**→**11**) is responsible for a red-shift of the first absorption band by ~25 nm, in excellent agreement with the experimental findings (26 nm). Just as for **8**

and **9**, this change is corroborated by the larger delocalisation of the frontier orbitals of **11** compared to the monosubstituted compound **10**. In these two systems, delocalisation arises from the favourable orientation of the cyclohexane σ-orbitals with respect to the π-orbitals of the BODIPY core. The same trend is measured and computed for the emission band, with comparable values.

Molar absorption coefficients ε_{max} of **8** and **9** have been measured in methanol and the corresponding oscillator strengths f calculated[20]. In agreement with the measurements that give ε_{max} and f values of 71600 L.mol^{-1}.cm^{-1} and 0.52, respectively, for **9** (versus 48600 L.mol^{-1}.cm^{-1} and 0.34, respectively, for **8**), the computed oscillator strengths are higher in the disubstituted compounds **9** and **11** (0.85 and 0.71, respectively, versus 0.78 and 0.63 in compounds 8 and 10).

### 3.1.2.2   Effects of the conformational restriction

The effect of conformational restriction on the optical properties of **8-11** has been investigated by studying the corresponding unrestricted dyes, **8u-11u**. As expected, the absence of conformational restriction in **8u** and **9u**, in which the phenyl group substituents are free to rotate, leads to an hypsochromic shift of the absorption band by ~21 nm and ~51 nm, respectively (Table 3.6 and Figure 3.13). These spectral changes arise from an increased planarity of the system together with the extended delocalisation of the HOMO orbital over the ethylene bridge linker in **8** (Figure 3.13). Constriction leads to a more rigid compound and partly prevents the rotation of the phenyl group at the 3-position: the value of the dihedral angle between the BODIPY core and the substituent decreases from ~40° to ~23° when passing from **8u** to **8**.
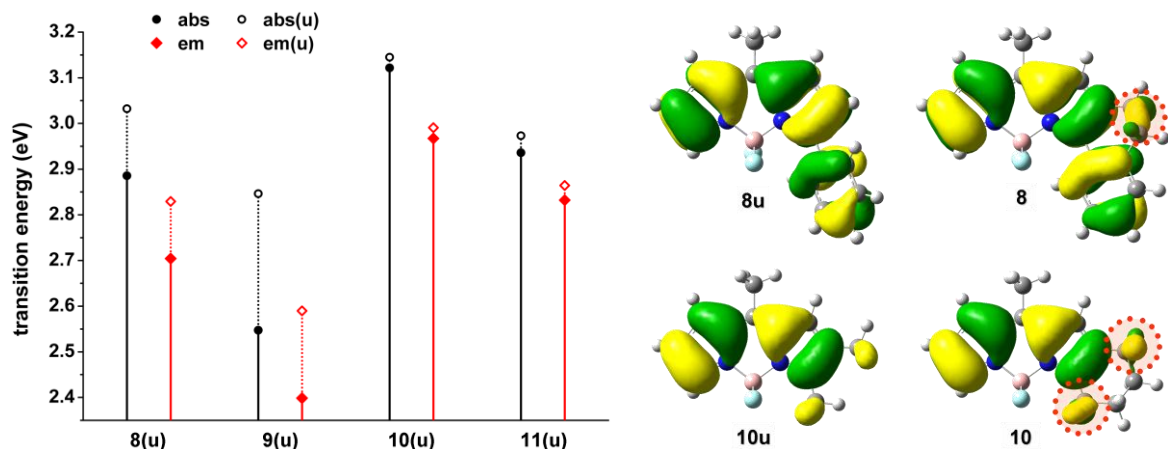
Figure 3.13 Experimental (solid lines) and theoretical (dashed lines) vertical transition energies for absorption and emission of **8(u)-11(u)** (left). Graphical representations of the HOMO of **8** and **10** and their unconstrained counterparts (right).

Because the phenyl rings have some rotational freedom in the unrestricted conformation, we have investigated the sensitivity of the calculated optical transitions to the dihedral angle between the BODIPY core and the substituent. In contrast to **8**, which has a rather steep minimum at ~19°, **8u** indeed presents a quite flat ground-state potential energy surface (with only ~1.4 kcal/mol between 15° and 37°, and one can thus expect conformationally broadened absorption bands. Yet, the spectra, simulated using either the optimised geometry or by considering a Boltzmann distribution of conformers, are quasi-superimposable (Figure 3.14).
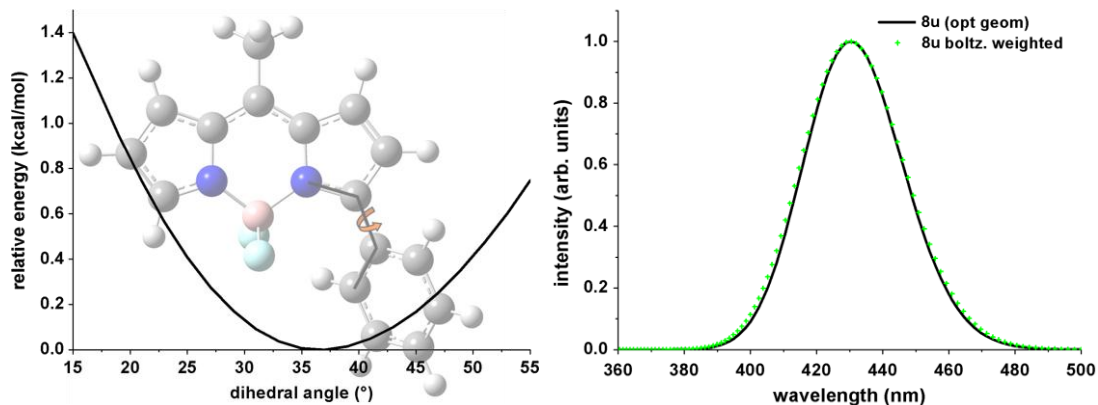
Figure 3.14 Scanned dihedral angle and associated ground-state PES of **8u** (left) and computed absorption spectra (right) - equilibrium geometry (black curve) and Boltzmann-weighted (green crosses).

Consistently with the conclusions of section 3.1.2.1., the same behaviour is observed for **9**, at higher wavelengths. The calculated spectral displacements of the absorption and emission maxima upon conformation restriction as well as the oscillator strengths are in good agreement with the only experimental data available, which report a clear bathochromic effect in both absorption and emission (in CH_2Cl_2, 77 and 53 nm, respectively). Moreover, the increase in the oscillator strength value upon constriction is consistent with the hyperchromic shift observed when going from **9u** to **9** (ε_{max}(544 nm) = 57000 L.mol^{-1}.cm^{-1} for **9u** vs ε_{max}(621 nm) = 134000 L.mol^{-1}.cm^{-1} for **9**). However, this effect may also arise from a decreased bandwidth due to the conformational restriction, resulting in an increase in the maximum extinction coefficient without changes in the oscillator strength.

Although no change in the absorption spectra is expected when passing from **10u** to **10**, it is most likely that the very small increase in transition

wavelength (3 nm) predicted upon going from the unconstrained to the restricted form arises from enhanced hyperconjugation effects associated with the methyl groups in **10u** (see Figure 3.13, where small weights are circled). Likewise, there is no significant spectral displacement upon conformational restriction of **11u**. The computed absorption wavelengths for **11u** and **11**, ~417 nm and ~422 nm, respectively, present only a small red shift (~5 nm), expectedly slightly larger than for **10(u)** as the BODIPY core is disubstituted. The same features are observed for the emission wavelengths.

3.2   Influence of the substituent nature and position

The variety of (hetero)atomic groups that can be grafted on the BODIPY core provides an outstanding opportunity to investigate the spectroscopic and photophysical characteristics of these dyes as a function of the substituents. Moreover, functionalisation at the α and β positions may result in distinct effects on the spectroscopic properties. To assess how these two effects (nature of the substituent and position of the substitution) affect the optical and electronic properties, we studied a series of 3-aryl-BODIPY derivatives with various substituent groups (**13a-15a**) and their 2-isomers (**13b-15b**) together with a reference compound **12** (Figure 3.15).
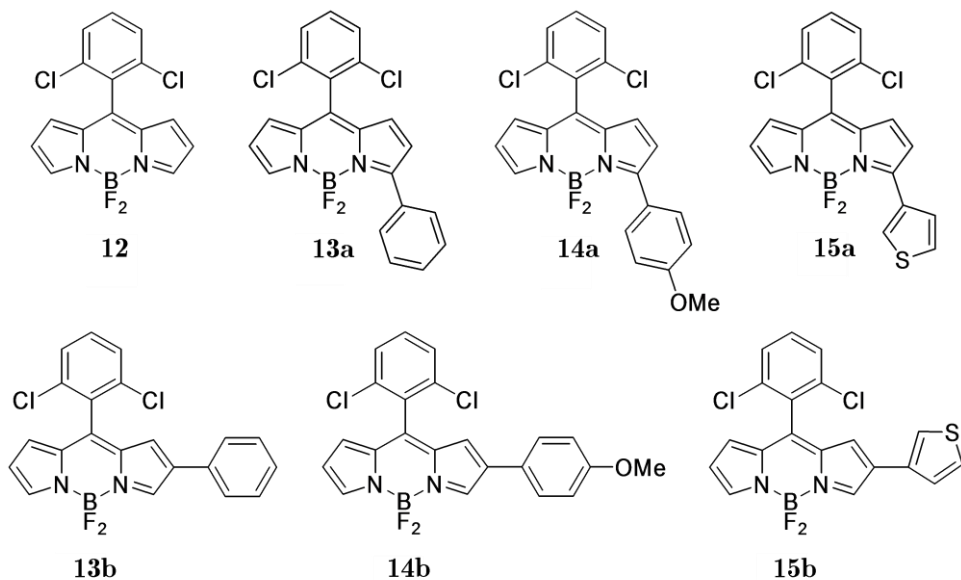
Figure 3.15 Structure of the 3-aryl and 2-aryl substituted BODIPY derivatives (and reference compound **12**).

Computational method

Ground-state geometries were optimised in the framework of the density functional theory (DFT) at the CAM-B3LYP/6-31G(d) level[29]. The equilibrium structures were subsequently used as input for the time-dependent DFT (TD-DFT) calculations of the vertical transition energies and oscillator strengths. Solvent effects were accounted for by using the polarizable continuum model (IEFPCM formalism[30]). The Gaussian G09 package[28] was used for all calculations.

3.2.1   Influence of the substituent nature

The effect of the nature of the substituent on the optical properties is investigated through the **13a-14a-15a** series in which the electro-donating

strength of the 3-aryl group is varying (Phenyl, 4-MeOPhenyl, and Thiophene, respectively). As the reference compound **12**, all three asymmetrically substituted systems display the typical absorption and emission features of BODIPY already encountered in the previous sections of this chapter (narrow bands, small Stokes shifts, weak solvent dependence). Their theoretical absorption wavelengths are compared to the experimental values in acetonitrile in Table 3.7.

Table 3.7 Computed wavelengths/energies of the first absorption vertical transition and associated oscillator strengths. Experimental absorption maximum is measured in acetonitrile.

	theoretical values				experimental values in MeCN	
	trans. energy (eV)	λ_{abs} (nm)	oscillator strength f	shift vs **12** (eV / nm)	λ_{abs} max (nm)	shift vs **12** (eV / nm)
12	3.01	412	0.5363	-	508	-
13	2.78	446	0.7046	0.23 / 34	536	0.13 / 28
14	2.71	458	0.7998	0.30 / 46	552	0.19 / 44
15	2.73	454	0.6938	0.28 / 42	549	0.18 / 41
13	2.79	444	0.6546	0.22 / 32	-	-
14	2.70	460	0.6295	0.31 / 48	-	-
15	2.74	452	0.6063	0.27 / 40	-	-

As is typically the case for BODIPY derivatives, the TD-DFT λ_{max} are underestimated, but the overall trend across the whole series of compounds is well reproduced by the calculations. More specifically, the introduction of one phenyl group at the 3-position (**13a**) is characterised by an expected bathochromic shift in absorption of 34 nm compared to

the reference **12**, in very good agreement with experimental measurement (28 nm), as a result of the extended conjugation. Replacing the 3-phenyl substituent in **13a** by electron donating groups (*p*-anisyl in **14a** and 3-thienyl in **15a**) results in red-shifted absorption of about ~10 nm (against ~15 nm experimentally). Globally, the overall spectral displacements towards longer wavelengths of the absorption maximum going from **12** to **13a**, **14a** and **15a** (of 34, 46 and 42 nm, respectively) are in very good agreement with the experimental findings.
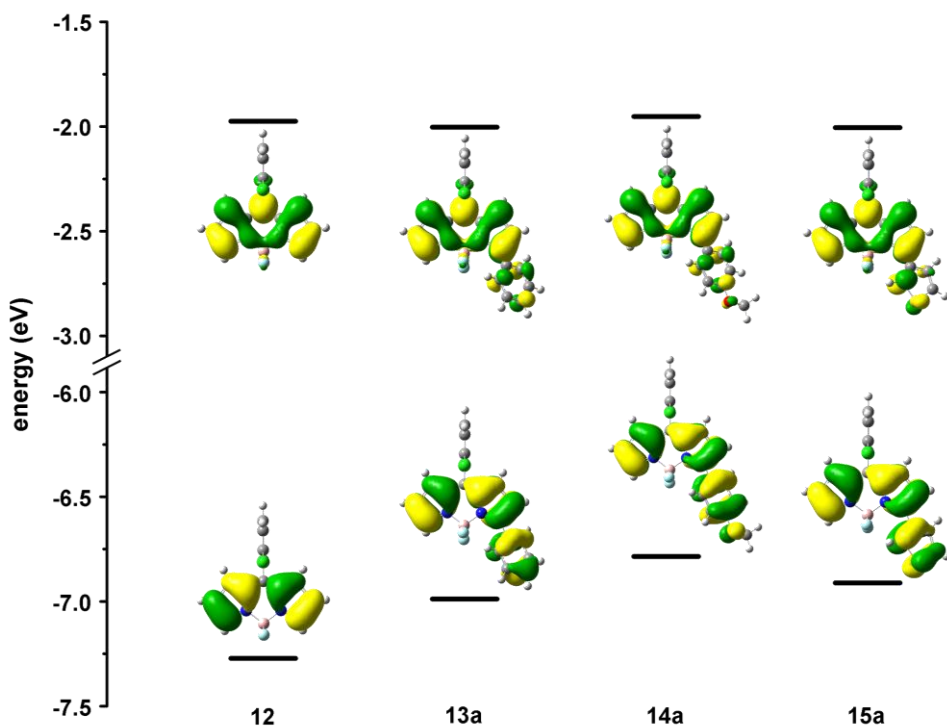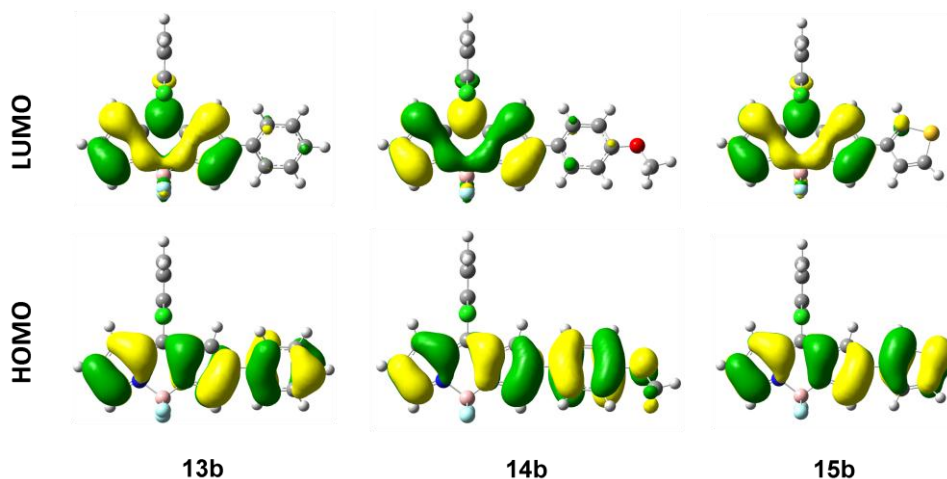

Figure 3.16 Graphical representation of the frontier orbitals of **12-15a** and evolution of their energies.

The lowest optical transition in all molecules is dominated by a HOMO-to-LUMO transition, so it suffices to discuss the shape and changes in the energetic position of the frontier orbitals upon substitution (Figure 3.16). The reference compound **12** possesses frontier orbitals that are strictly localised on the BODIPY core, with only vanishingly small contributions on the *meso*-substituent in the LUMO. The measured and computed bathochromic shift of the first absorption band upon adding a substituent at the 3-position is well illustrated by the frontier orbital representation of **13a**, **14a** and **15a**, which present the same bonding-antibonding pattern as **12** but spread out substantially over the conjugated arm (phenyl, *p*-anisyl and 3-thienyl, respectively). Compared to **12**, the larger spectral displacements obtained for **14a** and **15a** with respect to the 3-phenyl analogue **13a** can be rationalised by the shift in energy of the HOMO and LUMO orbitals upon substitution. The presence of electron-donating groups leads to an overall destabilisation of the frontier levels, which is larger for the HOMO as a consequence of the donor character of the substituents, and this translates into a reduced HOMO/LUMO energy gap, and thus a spectral shift towards the red.

3.2.2   Influence of the position of the functionalisation

The isomers resulting from the same substitutions of **12** in the 2-position (instead of the 3-position) were also studied (compounds **13b**, **14b**, **15b**, Table 3.7). The absorption maximum computed for **13b** is very close to the value calculated for the corresponding compound **13a**, suggesting that the conjugation extends equally over the phenyl side arm in 2- and 3-positions. This is borne out by the shape of the frontier orbitals involved in the transition, which reveal a similar delocalisation over the HOMO for

the two systems, yet a more confined (over the BODIPY core) character of the LUMO in **13b** (Figure 3.17) *versus* **13a** (Figure 3.16).
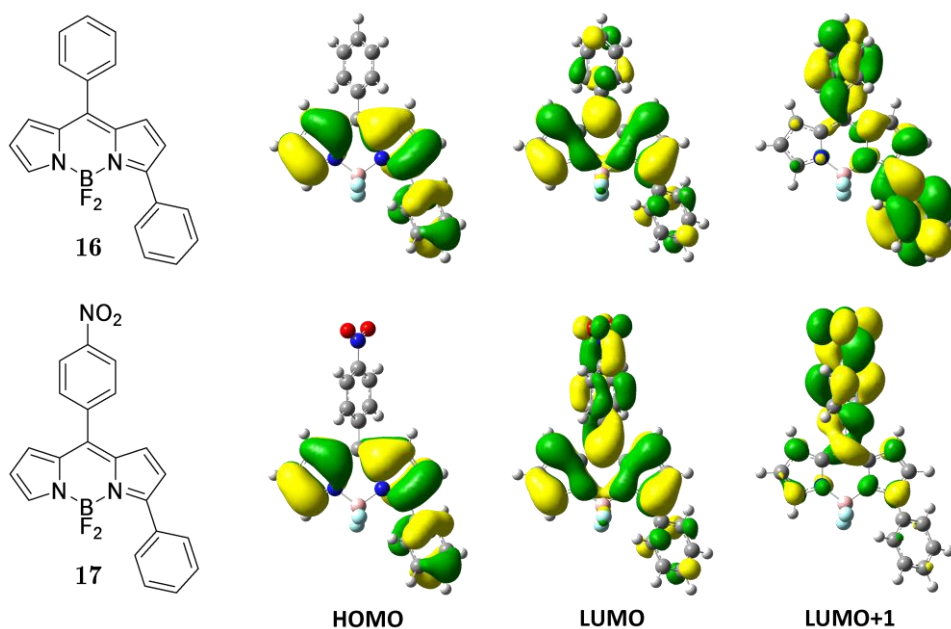

Figure 3.17 Graphical representations of the frontier orbitals
of **13b-15b**.

The spectral shifts computed for the 2-isomers **14b** and **15b** closely follow the trend observed for the 3-isomers (**14a** and **15a**, respectively), again associated with the improved conjugation across the side groups (although, as for **13b**, the LUMO wave function of **14b** and **15b** has a larger weight on the BODIPY units). The oscillator strengths computed for the 2-isomers compared to their 3-substituted homologues are in line with experimental observations reported by V. Leen et al[34].

3.2.3   *meso*-substitution of the BODIPY core

All the chlorinated derivatives investigated so far present a 90° dihedral angle between the *meso*-substituent and the mean plane of the BODIPY core, which can be attributed to the strong steric hindrance associated

with the presence of Cl atoms at the 2,6 positions of the *meso*-aryl group. We investigated the consequences of changing the *meso*-substituent nature of **13a** on its structural, optical and electronic properties, namely by studying **16** and **17** in which the 2,6-dichlorophenyl group is replaced by a phenyl and a p-nitrophenyl substituent, respectively (Figure 3.18). The absence of Cl atoms in **16** and **17** gives rise to smaller dihedral angles between the planes of the 8-aryl group and the BODIPY core, namely ~54° and ~57°, respectively, instead of 90° in the chlorinated derivatives in which rotation of the *meso*-substituent is locked.

Figure 3.18 Structure of **16** and **17** and graphical representation of their respective HOMO, LUMO and LUMO+1.

The first absorption transition of **17** is computed at 447 nm and involves mainly the frontier molecular orbitals (~93 %) but a higher charge-

transfer (HOMO→LUMO+1) excitation is also found to weakly contribute. While the HOMO orbital is strictly centred on the BODIPY core, the LUMO extends over the whole π-system whereas the LUMO+1 is localised mostly on the *meso*-substituent bearing the nitro group (Figure 3.18). The nature of the *meso*-substitution only has a small effect on the spectral position of absorption and emission maxima (λ_{abs}(max) of **13a** at ~446 nm), consistent with the absence of coupling between the two parts of the π-system, due to the twisting of the *meso*-aryl group out of the BODIPY plane. However, the removal of the chlorine atoms drastically reduces the quantum yield of fluorescence, with a measured value of 0.005 (against 0.884 for **13a**). This lowering is a consequence of the free rotation of the 8-aryl group that allows the molecule to lose its excited state energy via non-radiative molecular motions, while the rotation of the 8-(2,6-dichlorophenyl) group in the other dyes is obstructed by steric hindrance between the Cl atoms and the 1,7-hydrogen atoms of the BODIPY core.

Fluorescence quenching via photo-induced electron transfer has already been demonstrated for sterically hindered 8-substituted BODIPY derivatives bearing a nitro aromatic moiety[35,36]. Although the partial charge transfer character of the lowest excited state might have an impact on the overall emission efficiency, we think the main reason for the much lower values measured for **17** in comparison to **13a** has a conformational origin. Indeed, we expect that the conformational restriction brought by the bulky 2,6-dichlorophenyl substituent in **13a** slows down considerably nonadiabatic internal conversion to the ground state, thus favouring the radiative over non-radiative decay mechanisms. This is confirmed by the first excited state potential energy surface of compounds **13a** and **17** and their relative Boltzmann populations (as a function of the dihedral angle)

presented in Figure 3.19. From this figure, the much narrower distribution for **13a** compared to **17** is clear.
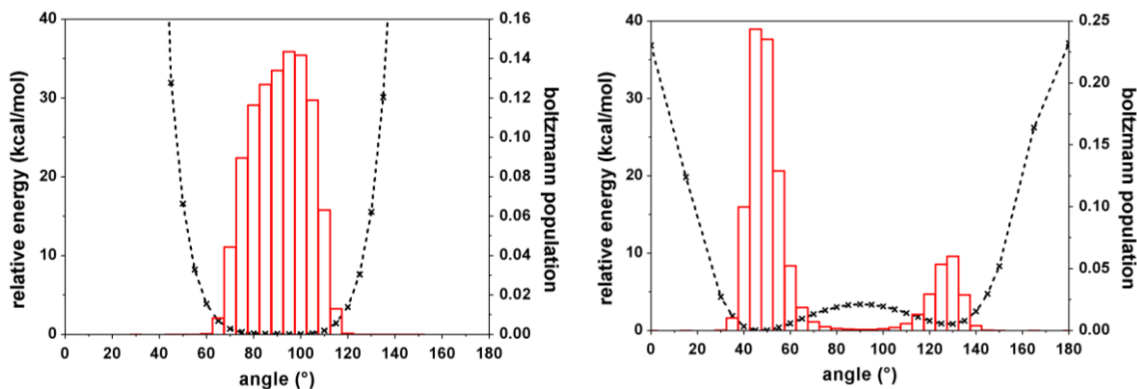

Figure 3.19 Potential energy surfaces of the first excited state (in black) and Boltzmann population histograms (in red), as a function of the dihedral angle between the BODIPY core plane and the *meso*-substituent, of **13a** (left) and **17** (right).

Calculations on compound **16** interestingly show that, despite the absence of a nitro group, the LUMO and LUMO+1 orbitals involved in the first absorption transition are delocalised over the *meso*-phenyl ring, as in **17** but in contrast to **13a**. The hypothesis of a more efficient non-radiative relaxation pathway as being the main cause for the reduced fluorescence quantum yield ϕ_f in **17** is supported by the fact that a similarly low ϕ_f value (0.015) has been measured for **16**, which differs from **17** only by the presence of the nitro group. *A fortiori*, the enhanced intramolecular charge-transfer character induced by grafting the nitro group at the *p*-position of the *meso*-aryl substituent must only have a weak impact on the decay mechanism.

3.3   Towards the blue side of the spectrum

In the search for dyes with absorption and emission maxima shifted towards ever longer wavelengths, many strategies have been developed to tune the optical properties of BODIPY and a substantial number of NIR-emitting derivatives were synthesised over the past decade. However, despite their outstanding thermal, photochemical and photophysical properties, only few BODIPY dyes optically active in the blue spectral region have been reported so far[37,38].

In this context, we investigated the electronic and optical properties of a series of 8-amino-BODIPY derivatives substituted with electron donating groups of various electro-active strengths (Figure 3.20). *Meso*-substitution of the BODIPY core can either result in a coplanar conformation in which the BODIPY core and the *meso*-substituent are in the same plane, or in a geometry with the two moieties in a perpendicular conformation (Figure 3.21), depending on steric repulsion effects. These two possible arrangements lead to very different photophysical properties.
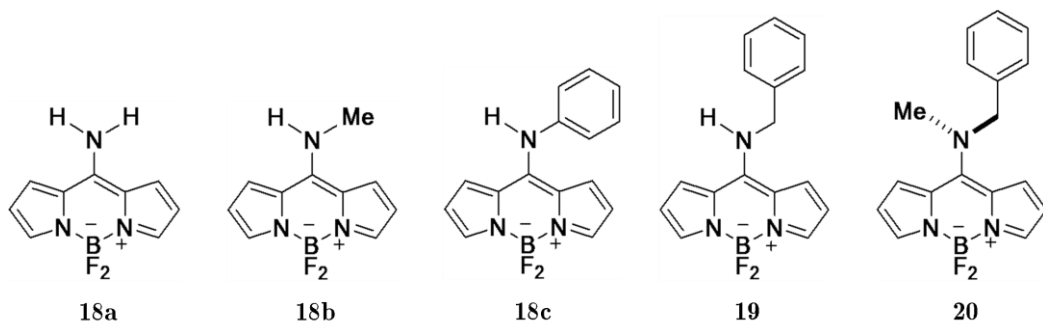
Figure 3.20 Structure of the 8-amino-substituted BODIPY derivatives investigated.

Computational method

In the framework of Density Functional Theory (DFT), all geometries were optimised at the B3LYP/6-31G(d,p) level[39], applying the Polarizable Continuum Model (in its IEFPCM formulation[30]) to account for solvent effects. On the basis of these structures, Time-Dependent Density Functional Theory (TD-DFT) has been applied to compute the vertical transition energies.


coplanar   perpendicular
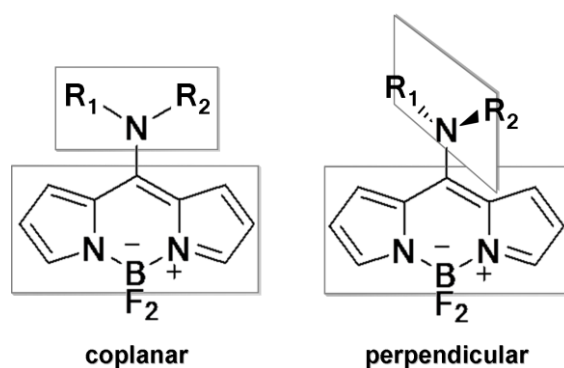
Figure 3.21   Representation of coplanar and perpendicular conformations of *meso*-substituted BODIPY.

Impact of the meso-substituent donor character and orientation

To evaluate how the donating strength of the *meso*-substituent can affect both conformational and electronic properties, we investigated **18a** (regarded as the reference compound), **18b** and **18c**, which differ by the donor character of the -NHR *meso*-substituent ($-NH_2$ < $-NHCH_3$ < -NHPh). All optimised geometries present a coplanar-like arrangement, with dihedral angles close to 180° for **18a** and **18b**, and a slight distortion in **18c** which exhibits a -167° angle between the two moieties, most likely as a result of the steric hindrance generated by the larger substituent size.

Substitution by a donor group is known to bring about an asymmetric destabilisation of the frontier orbitals, with a larger effect on the HOMO. Figure 3.22 presents the evolution in the energy of the frontier orbitals of **18a**, **18b** and **18c** and clearly, the expected trends are not observed, as the HOMO orbitals remains almost at the same energy, while a larger effect is noticeable on the LUMO. This can be rationalised considering the electronic density present at the 8-position in both orbitals. While there is a substantial contribution on the amino nitrogen atom in the LUMO, the HOMO orbital possesses a node in its wave function at this position (absence of electronic density on the 8-nitrogen atom), with the electronic cloud localised on the two pyrrole rings. Consequently, the frontier orbitals are not equally affected by the *meso*-substitution. The methylation in **18b** expectedly results in a very small destabilisation of both frontier orbitals. Regarding the evolution of the LUMO, it should be noted that this orbital is significantly stabilised in **18c** as a result of the larger delocalisation which extends over the phenyl moiety.
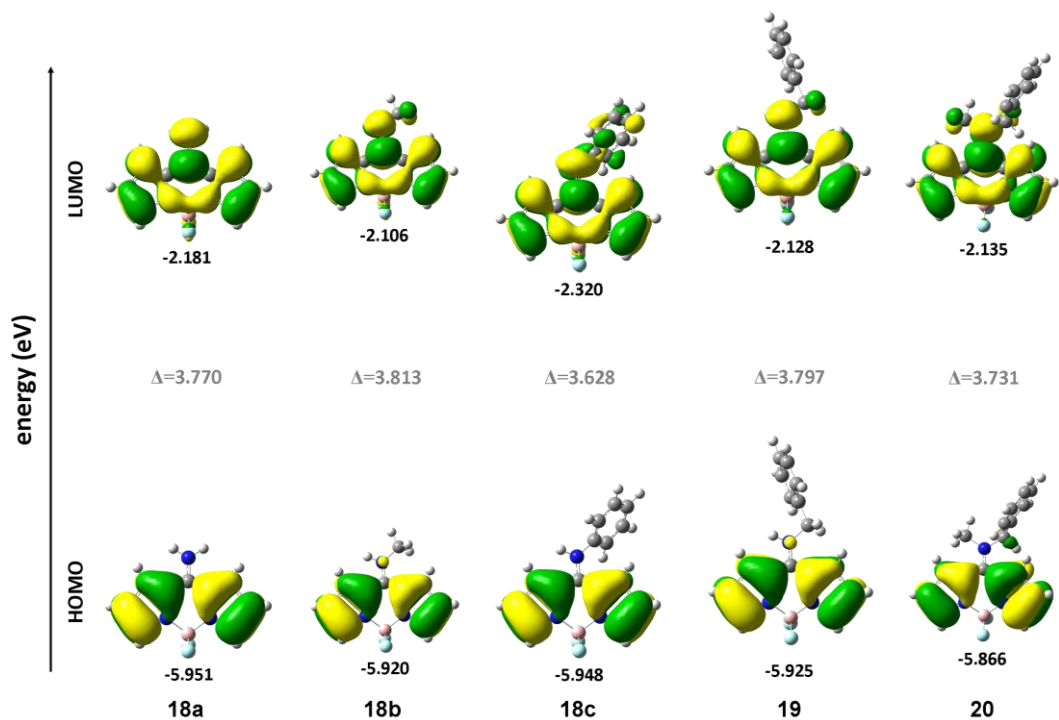
Figure 3.22 Graphical representation of the frontier orbitals of **18a-c**, **19** and **20**, with their associated energy.

As expected from the relative positions of the frontier orbitals, almost exclusively involved in the $S_0 \rightarrow S_1$ electronic transition, and the energy gaps between them, the largest wavelength is computed for **18c** at 377 nm while similar lower values are obtained for **18a** and **18b** with transitions at 363 nm and 361 nm, respectively (Table 3.8).

Table 3.8 Computed wavelengths/energies of the first absorption vertical transition of **18a-c**, **19** and **20** compounds and their associated oscillator strengths, with the nature of the transition.

	transition energy (eV)	transition wavelength (nm)	oscillator strength f	nature of the transition			
18a	3.42	363	0.4420	HOMO	→	LUMO	96.9%
				HOMO-2	→	LUMO	3.0%
18b	3.43	361	0.4055	HOMO	→	LUMO	96.8%
				HOMO-2	→	LUMO	2.7%
18c	3.29	377	0.3925	HOMO	→	LUMO	96.7%
				HOMO-2	→	LUMO	2.8%
19	3.42	363	0.3939	HOMO	→	LUMO	96.8%
				HOMO-2	→	LUMO	2.7%
20	3.30	375	0.3287	HOMO	→	LUMO	96.5%
				HOMO-2	→	LUMO	2.8%

The first absorption band being in all cases dominated by the HOMO→LUMO transition, it is sufficient to follow the evolution of these two orbitals to get insight into how the photophysical properties might be affected by the nature of the amino-substituent and its orientation relative to the BODIPY plane. We computed the potential energy surfaces (PES) of the three compounds in their ground state as a function of the dihedral angle between the chromophoric core and amino-substituent planes. According to these PES and associated Boltzmann population histograms (Figure 3.23 - left), we restrain our investigations to ±50° around the fully planar position. In this range of dihedral angles, we plotted the evolution of the frontier orbitals together with the corresponding HOMO/LUMO gap (Figure 3.23 - right).
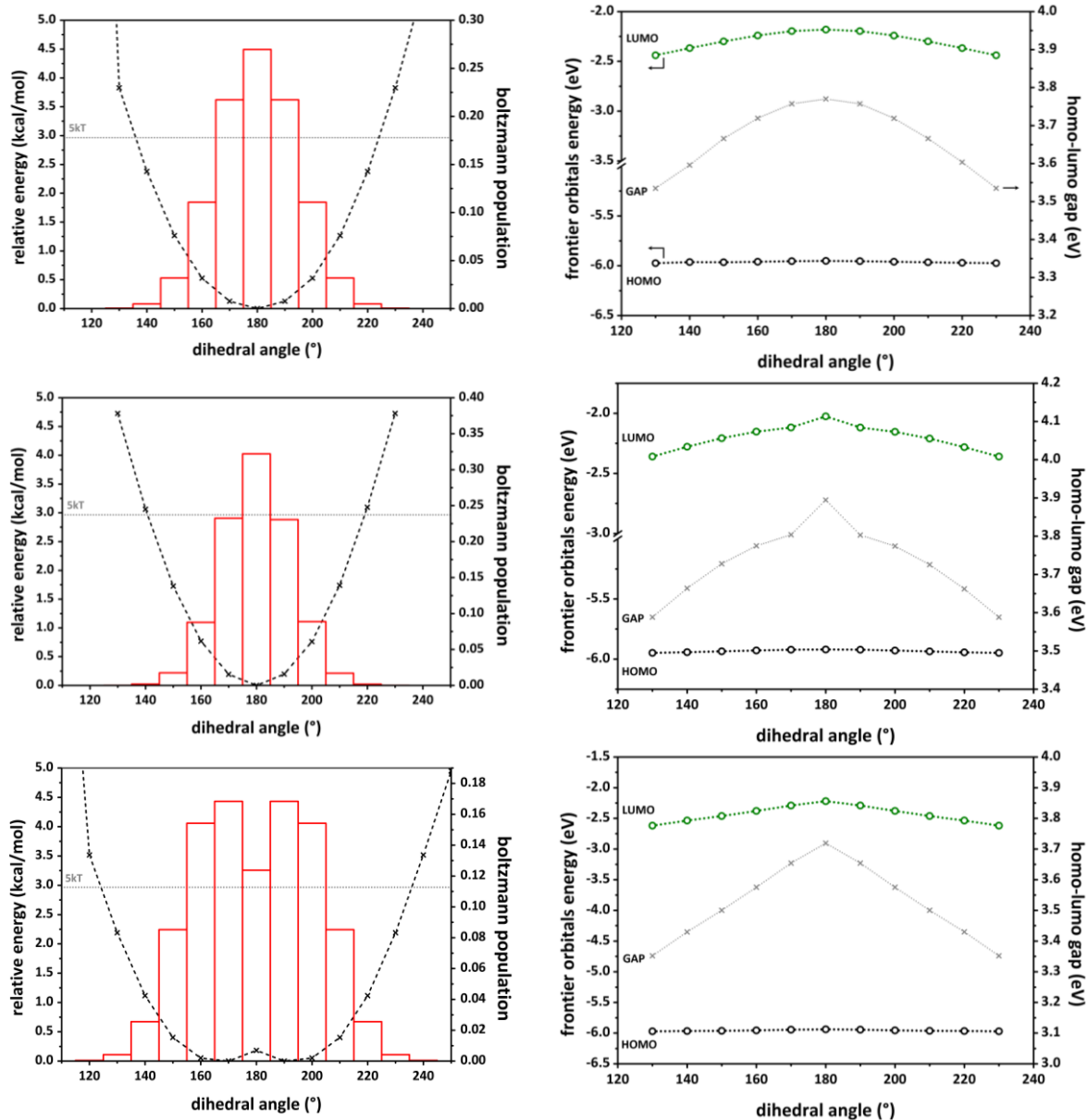
Figure 3.23 Individual PES with Boltzmann population histograms (in red) for **18a**, **18b** and **18c** and associated HOMO-LUMO evolution and energy gap (in grey), as a function of the dihedral angle between the BODIPY core and *meso*-substituent planes.

While the HOMO is only very slightly affected by the modification of the torsion angle, the LUMO experiences a large stabilisation when going from coplanar arrangement (180° angle) to more perpendicular-like conformation. This evolution confirms that the coplanar configuration is accompanied by a widening of the gap, which should translate into blue-shifted transitions.

For each geometry considered, the $S_0{\rightarrow}S_1$ transition was thus computed and the corresponding transition energy plotted against the dihedral angle (Figure 3.24): its evolution is in very good agreement with the trends already noticed in the HOMO/LUMO gap. Upon twisting of the *meso*-substituent away from coplanarity, the absorption maximum is red-shifted.
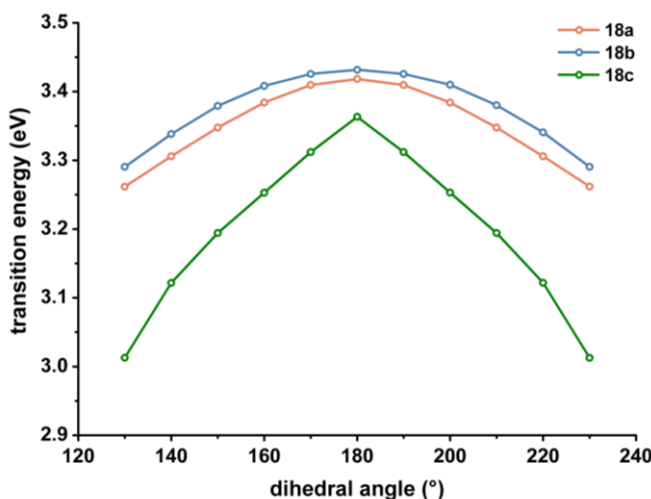
Figure 3.24 Evolution of the transition energy as a function of the dihedral angle between the BODIPY core and *meso*-substituent.

The optimised geometries of **19** and **20** reveal a coplanar-like conformation of the *meso*-substituent with respect to the BODIPY core, with dihedral

angles of -177° and -166°, respectively. In these two systems, the substituent is not directly linked to the nitrogen in *meso*-position so that delocalisation in the LUMO does not extend over the phenyl ring as in **18c**. However, vanishingly small weights are noticeable over the -CH2 and, additionally in **20**, over the carbon atom of the phenyl to which it is linked. This is consistent with the overall frontier orbital delocalisation **19** and **20** experience compared to **18c**. While methylation of the nitrogen is expected to bring about a destabilisation of the LUMO, rather similar energies are computed for this orbital in **19** and **20**, most likely due to the larger delocalisation of the LUMO in **20** (contribution on the methyl group). However, it also increases the donor character of the *meso*-substituent, which is illustrated by the HOMO destabilisation when going from **19** to **20**.

3.4   Conclusions

In this chapter, we reviewed different approaches to modulate the optical properties of BODIPY derivatives through the study of several series of compounds. Our theoretical results support the experimental observation that conformational restrictions via homo- or heterocyclic annulation constitute an efficient strategy to obtain large spectral displacements towards longer wavelengths. More specifically, we evidenced that symmetrical di-substitution (position 3 and 5) combined with annulation allows for an expansion of the conjugated system, and leads to very large bathochromic shifts of both the absorption and emission maxima, by up to ~50 nm. Regarding the consequences of a substitution at the 2-position, the same trends are reported, with lower oscillator strengths. Contrary to what is observed for the α- and β-substitution, the introduction of a substituent at the *meso*-position, while providing another way to

functionalise the BODIPY core, does not affect the absorption and emission wavelengths. However, it can greatly modify the fluorescence quantum yields: when steric hindrance prevents the rotation of the *meso*-group, the fluorescence can be enhanced. The opposite trend is observed for molecules where free rotation of the substituent is allowed, which results in a quenching of the fluorescence. Finally, we showed that the optical properties can also be tuned towards shorter wavelengths via the introduction of amino groups on the *meso*-position of BODIPY core. In summary, our theoretical results allowed us to reach a deeper insight into the changes of the spectroscopic properties of BODIPY derivatives, illustrating the relationships between their structure and conformation and their optical properties, with either hypso- or bathochromic shifts and modulation of the fluorescence.

References

[1]   K. Tram, H. Yan, H. A. Jenkins, S. Vassiliev, D. Bruce, *Dyes and Pigments* **82**, 392 (2009).

[2]   A. Schmitt, B. Hinkeldey, M. Wild, G. Jung, *J Fluoresc.* **19**, 755 (2009).

[3]   I. J. Arroyo, R. Hu, G. Merino, B. Z. Tang, E. Peña-Cabrera, *J. Org. Chem.* **74** (15), 5719 (2009).

[4]   T. Rohand, W. Qin, N. Boens, W. Dehaen, *Eur. J. Org. Chem.* 4658 (2006).

[5]   A. Burghart, H. Kim, M. B. Welch, L. H. Thoresen, J. Reibenspies, K. Burgess, F. Bergström, L. B.-Å. Johansson, *J. Org. Chem.* **64**, 7813 (1999).

[6]   L. Thoresen, H. Kim, M. Welch, A. Burghart, K. Burgess, *Synlett.* 1276 (1998).

[7]   J. Chen, A. Burghart, A. Derecskei-Kovacs, K. Burgess, *J. Org. Chem.* **65**, 2900 (2000).

[8]   Z. Shen, H. Röhr, K. Rurack, H. Uno, M. Spieles, B. Schulz, G. Reck, N. Ono, *Chem. Eur. J.* **10**, 4853 (2004).

[9]   A. Loudet, K. Burgess, *Chem. Rev.* **107**, 4891 (2007).

[10]   W. Zhao, E. M. Carreira, *Chem. Eur. J.* **12**, 7254 (2006).

[11]   R. Gresser, H. Hartmann, M. Wrackmeyer, K. Leo, M. Riede, *Tetrahedron* **67**, 7148 (2011).

[12]   A. Loudet, R. Bandichhor, L. Wu, K. Burgess, *Tetrahedron* **64**, 3642 (2008).

[13]   R. Gresser, M. Hummert, H. Hartmann, K. Leo, M. Riede, *Chem. Eur. J.* **17**, 2939 (2011).

[14] M. Wada, S. Ito, H. Uno, T. Murashima, N. Ono, T. Urano, Y. Urano, *Tetrahedron   Lett.* **42**, 6711 (2001).

[15] S. Goeb, R. Ziessel, *Org. Lett.* **9**, 737 (2007).

[16] K. Umezawa, Y. Nakamura, H. Makino, D. Citterio, K. Suzuki, *J. Am. Chem. Soc.* **130**, 1550 (2008).

[17] K. Umezawa, A. Matsui, Y. Nakamura, D. Citterio, K. Suzuki, *Chem. Eur. J.* **15**, 1096 (2009).

[18] A. B. Descalzo, H.-J. Xu, Z.-L. Xue, K. Hoffmann, Z. Shen, M. G. Weller, X.-Z. You, K. Rurack, *Org. Lett.* **10**, 1581 (2008).

[19] Y.-W. Wang, A. B. Descalzo, Z. Shen, X.-Z. You, K. Rurack, *Chem. Eur. J.* **16**, 2887 (2010).

[20] B. Valeur, *Molecular Fluorescence. Principles and Applications*, Wiley-VCH (2002).

[21] M. J. S. Dewar, E. G. Zoebisch, E. F. Healy, and J. J. P. Stewart, *J. Am. Chem. Soc.* **107**, 3902 (1985).

[22] AMPAC 8, 1992-2008 Semichem, Inc. PO Box 1649, Shawnee, KS 66222.

[23] R. A. L. Vallée, M. Van der Auweraer, F. C. De Schryver, D. Beljonne, M. Orrit, *ChemPhysChem*, **6**, 81 (2005).

[24] L. Jiao, C. Yu, M. Liu, Y. Wu, K. Cong, T. Meng, Y. Wang, E. Hao, *J. Org. Chem.* **75**, 6035 (2010).

[25] V. P. Yakubovskyi, M. P. Shandura, Y. P. Kovtun, *Dyes Pigm.* **87**, 17 (2010).

[26] J. Spandl, D. J. White, J. Peychl, C. Thiele,   *Traffic* **10**, 1579 (2009).

[27] V. Leen, D. Miscoria, S. Yin, A. Filarowski, J. Molisho Ngongo, M. Van der Auweraer, N. Boens, W. Dehaen, *J. Org. Chem.* **76**, 8168 (2011).

[28] Gaussian 09, Revision A.02 and B.012, M. J. Frisch, G. W. Trucks, H. B. Schlegel, G. E. Scuseria, M.A. Robb, J. R. Cheeseman, G. Scalmani, V. Barone, B. Mennucci, G.A. Petersson, H. Nakatsuji, M. Caricato, X. Li, H. P. Hratchian, A. F. Izmaylov, J. Bloino, G. Zheng, J. L. Sonnenberg, M. Hada, M. Ehara, K. Toyota, R. Fukuda, J. Hasegawa, M. Ishida, T. Nakajima, Y. Honda, O. Kitao, H. Nakai, T. Vreven, J. A. Montgomery Jr., J. E. Peralta, F. Ogliaro, M. Bearpark, J. J. Heyd, E. Brothers, K. N. Kudin, V. N. Staroverov, R. Kobayashi, J. Normand, K. Raghavachari, A. Rendell, J. C. Burant, S. S. Iyengar, J. Tomasi, M. Cossi, N. Rega, J. M. Millam, M. Klene, J. E. Knox, J. B. Cross, V. Bakken, C. Adamo, J. Jaramillo, R. Gomperts, R. E. Stratmann, O. Yazyev, A. J. Austin, R. Cammi, C. Pomelli, J. W. Ochterski, R. L. Martin, K. Morokuma, V. G. Zakrzewski, G. A. Voth, P. Salvador, J. J. Dannenberg, S. Dapprich, A. D. Daniels, O. Farkas, J. B. Foresman, J. V. Ortiz, J. Cioslowski, and D. J. Fox, Gaussian, Inc., Wallingford CT, 2009.

[29] T. Yanai, D. P. Tew, N. C. Handy, *Chem. Phys. Lett.* **393**, 51 (2004).

[30] B. Mennucci, E. Cancès, J. Tomasi, *J. Phys. Chem. B* **101**, 10506 (1997).

[31] M. Cossi, V. Barone, *J. Chem. Phys.* **115**, 4708 (2001).

[32] R. Improta, V. Barone, G. Scalmani, M. J. Frisch, *J. Chem. Phys.* **125**, 054103:1 (2006).

[33] R. Improta, G. Scalmani, M. J. Frisch, V. Barone, *J. Chem. Phys.* **127**, 074504:1 (2007).

[34] V. Leen, T. Leemans, N. Boens, W. Dehaen, *Eur. J. Org. Chem.* 4386 (2011).

[35] R. Ziessel, L. Bonardi, G. Ulrich, *Dalton Trans.* 2913 (2006).

[36] M. Landrum, A. Smertenko, R. Edwards, P. J. Hussey, P. G. Steel, *Plant J.* 62, 529 (2010).

[37] J. Bañuelos, V. Martín, C. F. A. Gómez-Durán, I. J. Arroyo-Cordoba, E. Peña-Cabrera, I. García-Moreno, A. Costela, M. A. Pérez-Ojeda, T. Arbeloa, I. López Arbeloa, *Chem. Eur. J.* 17, 7261 (2011).

[38] C. A. Osorio-Martínez, A. Urías-Benavides, C. F. A. Gómez-Durán, J. Bañuelos, I. Esnal, I. López Arbeloa, E. Peña-Cabrera, *J. Org. Chem.* 77, 5434 (2012).

[39] A. D. Becke, *Phys. Rev. A* 33, 2786 (1986).

Chapter 4

A joint experimental/theoretical study of molecular chromoionophores for zinc ion detection

The perylene monoimide derivative investigated in this chapter has been synthesised in the group of Prof. Dr. Klaus Müllen at the Synthetic Chemistry Department of the Max Planck Institute for Polymer Research in Mainz, Germany. The formation of the complex and the associated optical response were characterised with several spectroscopic techniques (FD-MS, ^{1}H-NMR, UV-Vis) as well as isothermal titration microcalorimetry (ITC). We performed quantum-chemical calculations to get insight into the detection mechanism and the consequences of Zn^{2+} binding on the optical properties of the PMI-DPA compound. Finally, we conducted further experiments to demonstrate the successful detection of Zn^{2+} with thin films on glass and, ultimately, the incorporation of the

sensitive molecule in a sol-gel deposited as the active layer within an optical fibre sensor (in collaboration with the 'Materials Science' and 'Electromagnetism and Telecommunication' departments of the UMONS-Faculté Polytechnique).

D espite its biological benefits, zinc is also known as a contributing factor in several psychiatric and neurological diseases.[1-3] Moreover, it is an environmental pollutant that may for instance be found in agricultural wastes and cause phytotoxicity.[4] Nowadays, zinc is one of the most heavily consumed metals in industry, with numerous applications such as in alloys, in particular for the corrosion protection of steel, oxide fillers and batteries. Its widespread use has raised the need for Zn^{2+} chemosensors and the development of probes for the zinc ion in water has retained much interest in the past decade.[5] In this context, our work aims at the development of a zinc ion sensor for monitoring the corrosion of galvanised steel.

The possibility to efficiently custom-design the molecular structure of organic dyes according to needs provides a cheap and straightforward platform for the creation of efficient optical sensors. Most organic-based optical probes rely either on inter/intramolecular photo-induced electron transfer (PET) or on charge transfer (see chapter 1). In short, the former usually consists of a chromophore-spacer-receptor system that undergoes fluorescence quenching or enhancement in the presence of the analyte, while the latter involves a conjugated chromophore-receptor pair and relies on ratiometric sensing using either light absorption or emission. Among all the available chromophores, perylene dyes are widely used in commercial applications due to their outstanding chemical, thermal and photochemical stability, their low toxicity, and low cost.[6-14] These features make them attractive building blocks for the design of novel zinc ion chemosensors. More specifically, appropriate functionalisation of perylene monoimide (PMI) at the 9 and/or 10 peri-positions allows for the generation of push-pull type molecules that can act as intramolecular charge transfer-based sensors, using the imide group as the acceptor and a zinc ionophore as the donor. In this work, PMI has been substituted with

the very popular dipicolylamine ligand (DPA) which is, owing to the nitrogen lone pair it possesses, a very good candidate for ICT.
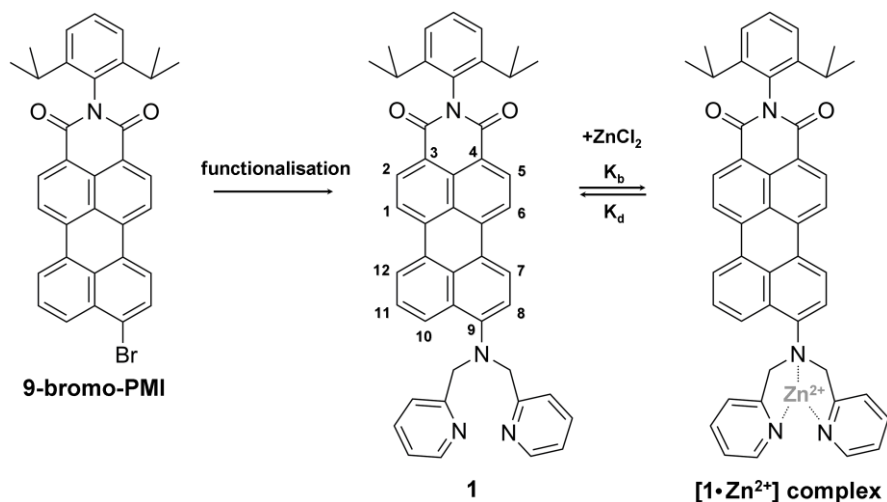
**Figure 4.1**   Structure of the PMI-DPA sensor **1** and its complex with zinc ion.

Computational method

The ground-state geometry of **1** in the absence/presence of Zn^{2+} was optimised at the density functional theory B3LYP/6-31G* level[15]. Those equilibrium geometries were subsequently used as input for the calculation of the electronic excited states and the simulation of the optical absorption spectra in the framework of time-dependent density functional theory (TD-DFT). We used the LanL2DZ[16] effective core potential and a valence basis set to describe the zinc ion. Solvent effects were taken into account by combining a dielectric continuum model (IEFPCM[17]) with an explicit description of the first solvation shell by acetone molecules. Static isotropic molecular polarisabilities were computed at the B3LYP/6-31+G(d) level from the previously optimised geometries by solving the

coupled perturbed Hartree-Fock equations. All the calculations were carried out using the Gaussian (G09) program package[18].

4.1   Geometries of [1·Zn^{2+}]

Optimisation of the PMI-DPA-Zn^{2+} system yields two different local minima with relatively close energy (~0.39 eV). In the first conformation (noted **1a** hereafter), one pyridine rotates around the CH$_2$-pyridine bond so that the zinc ion interacts with the two pyridinic nitrogen atoms (Figure 4.2, Table 4.1).

front and side views of 1
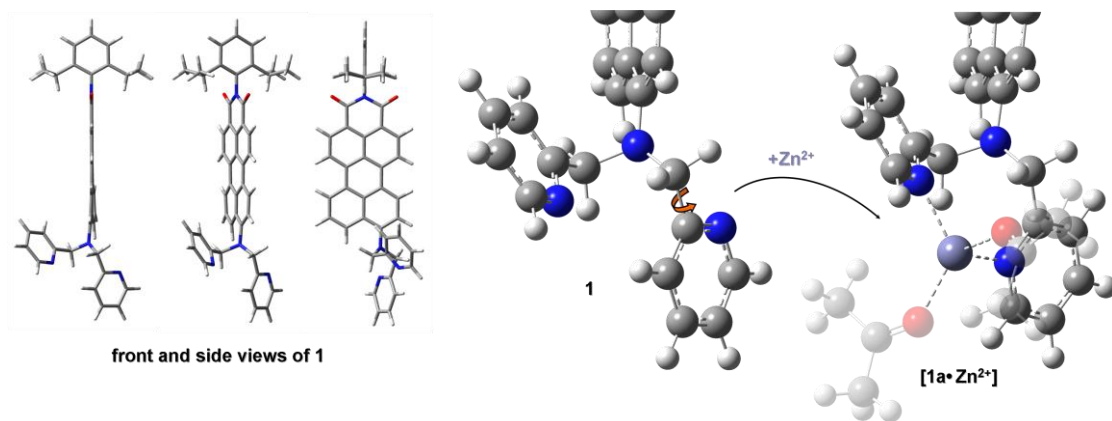
Figure 4.2 Optimised geometries of **1** and **1a**·Zn^{2+}.

The larger conformational rearrangement, which brings the ion closer to the nitrogen atom on the 9-position (N9) in the more stable conformation (noted **1b**), involves a second rotation around the C9-N9 bond (Figure 4.3, Table 4.1). However, in both cases, the coordination shell of Zn^{2+} appears incomplete, suggesting that at least one additional ligand, such as a one acetone molecule interacting via its oxygen atom, could also bind the metal ion. To investigate the relative stability and spectroscopic

properties of complexes characterised by different coordination numbers (CN) of Zn^{2+} (namely 4, 5 and 6), acetone molecules were explicitly added to the system. They appear slightly transparent in Figure 4.2 and 4.3, for the sake of clarity. All geometry optimisations yield stable structures, except CN=6 in **1b**, because of too large steric hindrance. We examined only 1:1 complexes, consistent with the isothermal titration calorimetry experiments (section 4.3).
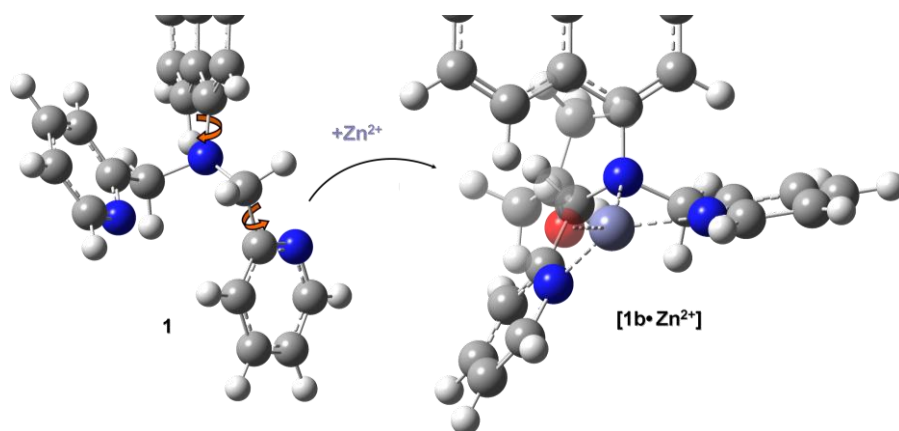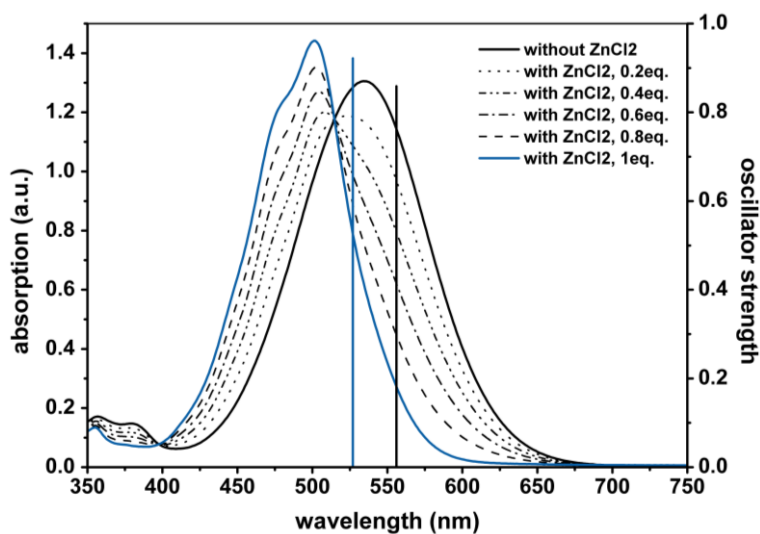

Figure 4.3 Optimised geometries of **1** and **1b**•Zn^{2+}.

Table 4.1 Zn-N and Zn-O bond lengths in **1a**•Zn^{2+} and **1b**•Zn^{2+}.

	bond lengths (Å)	**1a**•Zn^{2+}	**1b**•Zn^{2+}
	Zn-N9	3.90	2.24
	Zn-Npyr1	2.15	2.01
	Zn-Npyr2	2.13	2.02
	Zn-O1	2.08	2.01
	Zn-O2	2.09	-

4.2   Optical properties

Figure 4.4 Absorption spectra of the complexes of **1** (4.42 ×
10^{-5} M) with increasing amounts of ZnCl$_2$ in acetone solution.
The black and blue vertical bars are the oscillator strengths
associated to the computed transition for **1** and **1a·**Zn^{2+},
respectively.

In the absence of Zn^{2+}, the calculated absorption spectrum from the
optimised ground state geometry of **1** presents an absorption band at 555
nm associated with an excited state largely dominated by the
HOMO/LUMO transition. Though slightly underestimated (0.1 eV), the
computed transition energy can be considered in good agreement with the
experimental value of 534 nm measured in acetone (Figure 4.4). In the
presence of one equivalent of ZnCl$_2$, an hypsochromically shifted peak at
501 nm is observed, with a clear isosbestic point at 515 nm (Figure 4.4),
consistently with a transition from purple (i.e., the colour of **1**) to red (a
colour similar to PMI without substitution in 9-position). We simulated

the absorption spectra for the two conformations of the complex, with the different coordination numbers possible for the zinc ion.

*Conformation n°1: **1a**•Zn^{2+}*

Two acetone molecules were included to the system in **1a** to obtain the (distorted) tetrahedral geometry of the tetra-coordinated complex (see Figure 4.2). The simulated absorption spectrum of **1a**•Zn^{2+} presents a strong absorption band at 527 nm corresponding to the $S_0 \rightarrow S_1$ transition, essentially characterised by a HOMO→LUMO excitation, as found in the free molecule. The computed blue shift of the first absorption band upon complexation amounts to 28 nm, in very good agreement with the experimental shift (33 nm), and comprises two different contributions: a conformational reorganisation and a change in the electronic structure. As already mentioned, the main structural modification in the presence of the ion involves the rotation of one pyridine unit in the ionophore. To assess this effect, we have computed the absorption spectrum of the complex in its equilibrium geometry, after removal of the zinc ion and acetone molecules, to isolate the conformational rearrangement. It is found to provide only a 3 nm contribution to the hypsochromic shift, which is thus dominated by electronic effects (discussed hereafter). Note that the same conclusions can be drawn for the complexes with CN=5 and CN=6 (Table 4.2).

*Conformation n°2: **1b**•Zn^{2+}*

Complex **1b** is characterised by a larger torsion angle around the perylene-ionophore C-N bond, together with a shorter distance between Zn^{2+} and N9, suggesting a stronger electronic interaction and, as a result, a stronger impact on the absorption spectrum compared to **1a**. In line

with these expectations, the simulated absorption spectrum of **1b•Zn^{2+}** + one acetone molecule (CN=4) shows a more pronounced blue shift (compared to **1a•Zn^{2+}**): the lowest optical transition (mainly HOMO→LUMO) is computed at 504 nm, hypsochromically shifted by 51 nm with respect to the free dye. Of this shift, a 14 nm contribution stems from conformational effects. The structure with CN=5, obtained by adding a second solvent molecule, shows the same behaviour (Table 4.2).

**Table 4.2** Calculated spectroscopic properties of the free dye and the complexes investigated.

	1	**1a•Zn^{2+}**			**1b•Zn^{2+}**	
	free dye	CN4	CN5	CN6	CN4	CN5
λ_{abs} max (nm)	555	527	530	533	504	510
hypsochromic shift (nm/cm^{-1})	-	28 / 957	25 / 850	22 / 744	51 / 1823	45 / 1590
electron density of N9 in HOMO	0.0985	0.0336	0.0431	0.0561	0.0146	0.0239

Discussion

In all the structures investigated, the quantum-chemical calculations indicate that addition of Zn^{2+} to the PMI-DPA dye entails a blue shift of the lowest absorption band, qualitatively and quantitatively in agreement with the experimental spectroscopic data in solution. Focusing on the electronic structure, we notice that the formation of the complex is accompanied by an asymmetric stabilisation of the frontier molecular orbitals that are mostly involved in the lowest electronic excitation, with

a larger lowering of the HOMO, resulting in the overall blue shift (Figure 4.5).
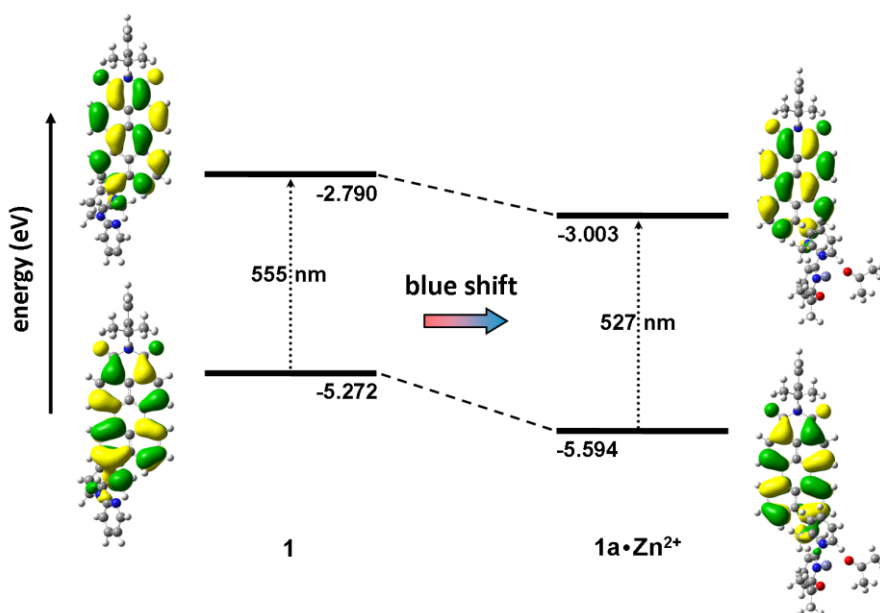
Figure 4.5 Evolution and graphical representation of the frontier orbitals of **1** upon complexation of Zn^{2+}.

This effect is due to a reduced electronic density over the nitrogen atom in the 9-position (thereby reducing its electron-donating strength) and a concomitant smaller intramolecular charge transfer character of the amino-substituted PMI dye in the presence of Zn^{2+}. This is confirmed by the analysis of the electronic density distribution over N9 in the HOMO level (Table 4.2): in the presence of the zinc ion, the donating strength of the nitrogen drastically decreases, in particular for **1b**, as does the intramolecular charge transfer (ICT) character.

4.3 Thermodynamics of Zn²⁺ complexation

4.3.1 Stability of the complex

Isothermal Titration Microcalorimetry (ITC) represents a valuable experimental method in the determination of the thermodynamic parameters characterizing recognition processes.[19] ITC measurements were carried out in the group of Prof. Müllen at the Max Planck Institute for Polymer Research in Mainz. By determining the heat changes accompanying the binding between the ligand and the cation, one can follow the complexation event and assess for parameters like the stoichiometry, the complexation enthalpy (ΔH) and entropy (ΔS), and the dissociation constant (K_d, Figure 4.1). The stoichiometry of the complex determined by ITC is approximately 1:1 (1.18±0.03), which correlates well with the UV-Vis data. The complexation of Zn^{2+} by **1** in acetone is detected as an endothermic process with a moderate positive enthalpy (4.7 kcal/mol), compensated by a higher entropic term ($T\Delta S = 12.0$ kcal/mol), rendering the Gibbs energy negative (-7.3 kcal/mol). The dissociation constant of $[\mathbf{1}\cdot\mathrm{Zn}]^{2+}$ is in the micromolar range ($K_d = 5 \times 10^{-6}$ mol/L, $K_b = 2 \times 10^5$ L/mol).

The enthalpy and Gibbs free energy changes associated to the complexation of Zn^{2+} were quantum-chemically evaluated according to the following equation:

$$\Delta H° (298.15K) = \Sigma(E_{elec} + H_{corr})_{products} - \Sigma(E_{elec} + H_{corr})_{reactants}$$
$$\Delta G° (298.15K) = \Sigma(E_{elec} + G_{corr})_{products} - \Sigma(E_{elec} + G_{corr})_{reactants}$$

The individual free energy terms comprised in these equations were calculated by summing thermal corrections to enthalpy and Gibbs free energy, H_{corr} and G_{corr}, respectively, extracted from the vibration frequency analysis (performed on each isolated energy minimum structure) to the

total electronic energies E_{elec} obtained from single-point calculations on optimised geometries at the B3LYP/6-311G(d) level (Table 4.3).

Table 4.3 Single-point electronic energy and thermal corrections to enthalpy and Gibbs free energy (at 298.15K) for the reactants and products involved in the complexation reaction of Zn^{2+} (in atomic units).

	1	acetone	Zn^{2+}	**1a•Zn^{2+}** (CN4)
E_{elec} *(from single point)*	-1346510.70	-121241.19	-768489.85	-1630025.77
H_{corr}	487.55	56.70	350.06	608.45
G_{corr}	409.44	35.21	275.59	512.74
$E_{elec} + H_{corr}$	-1346023.15	-121184.48	-768139.78	-1629417.32
$E_{elec} + G_{corr}$	-1346101.26	-121205.98	-768214.26	-1629513.03

Calculating $\Delta H°$ ($\Delta G°$) by simply taking the difference of individual enthalpy (Gibbs free energy) values for the reactants and the products requires to pay particular attention to the proper equilibration of the complexation reaction ; thus, the following equation is considered: **1** + $[Zn((CH_3)_2CO)_6]^{2+} \rightarrow$ **1a•Zn^{2+}**$_{[CN4]}$ + $4(CH_3)_2CO$. From the values collected in Table 4.3, we calculated a negative Gibbs free energy of -21.41 kcal.mol^{-1}, in line with the exergonic character already measured in the ITC experiment. A positive enthalpy of complexation of 7.67 kcal.mol^{-1} is computed, again in line with the endothermic character measured.

4.3.2 Response to other ions

In order to investigate the response of **1** to other cations, namely Ca^{2+}, Ag^+, Hg^{2+}, Fe^{2+}, Cu^{2+}, Ni^{2+} and Co^{2+} (where the metal salts were $CaCl_2$,

AgNO$_3$, HgCl$_2$, FeCl$_2$, CuCl$_2$, NiCl$_2$, respectively), fluorescence experiment were conducted. None of the equimolar complexes of **1** with the above-mentioned cations results in a fluorescence enhancement at 600 nm upon irradiation at 515 nm (Figure 4.6), in contrast to the results for the Zn^{2+} ion. The Hg^{2+} ion generated a negligible two-fold increase of compound **1** fluorescence, as compared to the fluorescence enhancement induced by Zn^{2+} (20-fold increase).
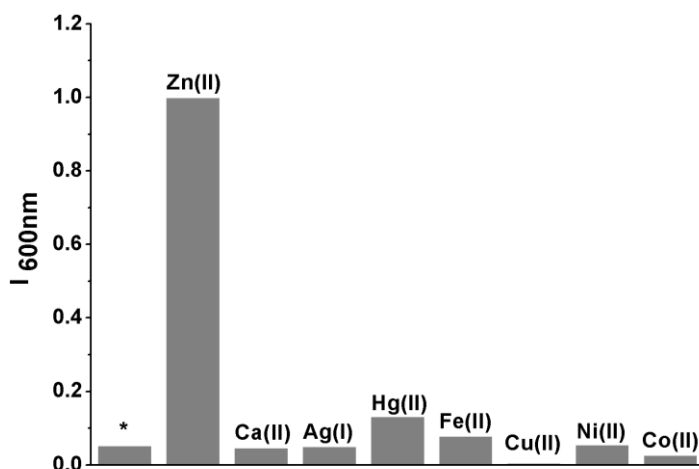
Figure 4.6 Fluorescence intensity at 600 nm of a 1:1 mixture of metal salts and compound **1** at 600 nm upon excitation at 515 nm. The control measurement is labelled with the asterisk. Cu^{2+} quantitatively quenches the fluorescence, due to the photo-induced electron transfer already demonstrated by others[20].

The simulation of the emission spectra associated to all these cation complexes is a computationally very demanding task. Thus, we decided to focus on the thermodynamic aspects of the complexation of **1** with the

copper ion, which results in a quenching of the fluorescence. To this end, we proceeded as for the complexation of the zinc ion presented in the previous section.

The most common coordination number of Cu^{2+} being 4, we calculated the thermal corrections to the enthalpy and Gibbs free energy for $[Cu(acetone)_4]^{2+}$ as well as for the **1a•Cu^{2+}** (CN4) complex. Single-point calculations on these two systems at the B3LYP/6-311g(d) level were performed to compute the ΔH and ΔG of complexation and values of - 18.63 kcal.mol^{-1} and -32.53 kcal.mol^{-1}, respectively, were obtained. These values are more negative than those determined for the Zn^{2+} complexation. This indicates that the unwanted presence of Cu^{2+} in the environment where the detection of the zinc ion is intended to be done could lead to interference and diminish the efficiency of the sensor. However, in the framework of the corrosion detection of galvanised steel, the key aspect does not lie in the interference from other ions but rather in the sensitivity of the sensor response in the presence of Zn^{2+}.

4.4 Detection of Zn^{2+} by PMI-DPA within an optical fibre sensor

Among the possible platforms that can serve for the development of sensing devices, the optical fibres display many attractive features, such as their flexibility, small dimensions and light weight, but also the possibility to perform distributed measurements over potentially long distances. Optical fibres can be decorated with a Bragg grating, which is a periodic and permanent modulation of the core refractive index of a section of the optical fibre along the propagation axis that acts as a wavelength-selective filter around the so-called Bragg wavelength.[21] When the Bragg grating is tilted by a few degrees relative to the

perpendicular to the fibre axis (TFBG), the fibre becomes sensitive to the environment as the TFBG couples light from the core to the cladding. As a result, it presents a comb-like transmission amplitude spectrum comprising several tens of resonances, each one characterised by its own sensitivity to the surrounding refractive index. The resulting TFBG spectrum is directly influenced by the refractive index of the surrounding medium and naturally act as a refractometer accurate to 10^{-4} RIU (refractive index unit).[22-24] Specific chemical sensors can be built by using TFBGs covered with a dedicated coating that changes its refractive index when in contact with the target chemical species.[25,26] The sensor envisioned in this work consists in a standard silica fibre with a tilted fibre Bragg grating covered by a sensitive layer of **1** whose refractive index (real and imaginary part) changes after the formation of a complex with Zn^{2+}.

4.4.1. Estimation of the refractive index change upon complexation

The refractive index modification accompanying the complexation of Zn^{2+} has to be large enough to enter the range of detection of the fibre aforementioned. We thus performed quantum-chemical calculations to estimate the change in refractive index upon complexation, Δn, as a function of the number density. Δn was computed from the calculated molecular polarisabilities of **1** and **1a**•$Zn^{2+}_{[CN4]}$. The molecular polarisability α, i.e., the linear response to an electric field of the electronic charge distribution of a molecule, is a microscopic quantity that can be related to the macroscopic refractive index n through the following expression according to the Lorentz-Lorenz equation:

$$n^2 = -\frac{2N\alpha + 3\varepsilon_0 V}{N\alpha - 3\varepsilon_0 V} \qquad (4.1)$$

where N is the number of molecules in a volume V and ε_0 is the vacuum permittivity.

We considered the case of a single molecule in a varying volume comprised between two limit cases, the van der Waals density and a large dilution. In order to approach the experimental conditions, where the dye concentration amounts to ~1.5% in weight of the final dry film, we estimated a volume of V~150000 $\mathring{A}^3$ for a single molecule and computed the corresponding Δn for V and V±33%, both in the gas phase and considering the solvent effects of water (Table 4.4). Chloride ions are added to complete the coordination of Zn^{2+} in the gas phase, and kept when accounting for the water, for better comparison.

**Table 4.4** Computed Δn upon complexation of Zn^{2+} by **1**, in the gas phase and in water.

volume ($\mathring{A}^3$)	n (**1**) gas phase	n (**1**) pcm	n (**1a•Zn^{2+} + 2 Cl$^-$**) gas phase	n (**1a•Zn^{2+} + 2 Cl$^-$**) water	Δn gas phase	Δn water
100000	1.00623	1.00903	1.00660	1.00952	0.00037	0.00049
150000	1.00415	1.00601	1.00440	1.00634	0.00024	0.00033
200000	1.00311	1.00451	1.00330	1.00476	0.00018	0.00025

The Δn values found are all above the detection limit of the fibre sensors considered in this work ($*10^{-4}$), indicating that **1** may successfully be used in such devices for Zn^{2+} sensing.

4.4.2 Detection of zinc ions by 1 in the solid state

On glass substrates

Prior to depositing **1** on optical fibres, experiments were first performed on simple glass substrates. Films of about 100 nm thickness were prepared by drop casting THF solutions of **1** and they were dipped in aqueous Zn^{2+} solutions of various concentrations (**1** is not soluble in water). We followed the evolution of the optical properties of **1** upon complexation with the zinc ion by recording absorption spectra every 2 minutes over a 30 minutes immersion period. As a control experiment, a film was dipped into pure water.
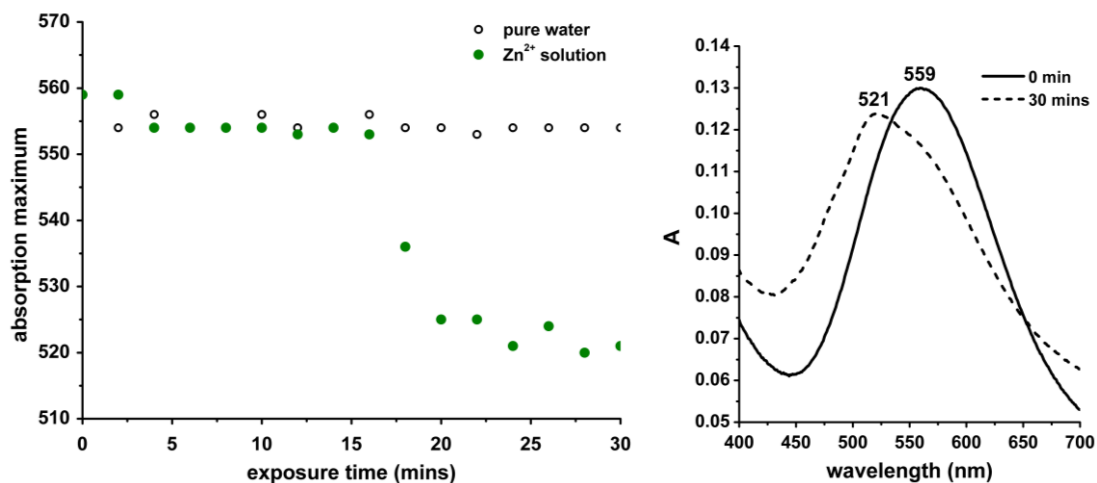
Figure 4.7 Evolution of the absorption maximum with time of exposure to the Zn^{2+} solution (full dots) and pure water (open dots) of 100 nm thick films of **1** on glass (left) and absorption spectra of a film of **1** dipped in an aqueous solution of Zn^{2+} (2.0M) at t=0min and t=30mins (right).
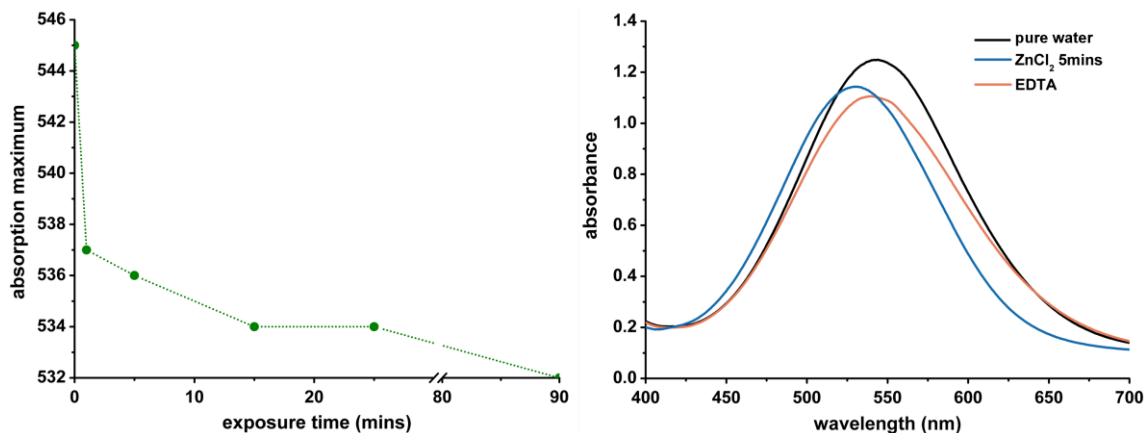
The evolution of the absorption maximum as a function of immersion time in a 2 mol.L^{-1} Zn^{2+} solution (and in pure water) is displayed in Figure 4.7, together with the initial (t=0) and final (t=30 mins) spectra. When dipped in water (and at t=0 in the Zn^{2+} solution), the absorption spectrum is similar to that observed in acetone solutions, with a slight (~0.1 eV) shift most probably associated to the difference in dielectric environment, and it does not evolve with time. In the presence of Zn^{2+}, the absorption peak gradually shifts hypsochromically from 559 nm to 521 nm, as a result of the complexation of the zinc ions (as no spectral change is observed in the control experiment). This shift of 38 nm is very similar to that measured in solution (33 nm). However, it appears more clearly only after 15 mins and one can clearly note the persistence of a shoulder around 560 nm in the spectrum at t=30mins. This long response time and spectral behaviour is most likely due to the slow diffusion of the ions in the rather thick, hydrophobic organic layer.

To improve the diffusion of Zn^{2+}, the dye was then encapsulated in a silica sol-gel and deposited on a glass substrate to perform a similar experiment previously described. Incorporating **1** in the sol-gel permits to deposit even thicker, more uniform films[i] for a better optical signal, while allowing the easy diffusion of the ions.

---

[i] The interrogation length of the TFBG is of the order of the wavelength, typically 1μm. To obtain maximum response of the TFBG to the refractive index changes of the sensitive coating, its thickness should thus be more than 1μm.

Figure 4.8 (left) Evolution of the absorption maximum with time of exposure to a 1M Zn^{2+} solution of a 5 μm-thick sensitive sol-gel coating on glass and (right) absorption spectra of the coating in pure water (black line), after 5 mins exposure to the Zn^{2+} solution (blue line), and after addition of EDTA at the end of the Zn^{2+} exposure (orange line).

As displayed Figure 4.8, the response time is clearly reduced with a measured 8 nm blue-shift within the first minute of the experiment, corroborating the better diffusion of the zinc ion when **1** is encapsulated in a sol-gel, rather than simply deposited as a pure film. To assess for the reversibility of the complexation event, EDTA was added in the solution and the absorption spectrum was recorded after rinsing with water. Maximum absorption in pure water occurs at 544 nm and shifts towards 530 nm after 5 mins of exposure to Zn^{2+}. Upon addition of EDTA, the absorption band shifts back to 540 nm, evidencing the reversibility of the complexation.

The same sensitive sol-gel encapsulating **1** was deposited on an optical fibre and the TFBG transmitted amplitude spectra recorded in pure water and in the presence of Zn^{2+} ions (1M solution) are presented in Figure 4.9. These experiments were done with the support of Dr. Ir. Marc Debliquy and Jean-Michel Renoirt, from the Materials Science and Electromagnetism and Telecommunication departments of the UMONS-Faculté Polytechnique.
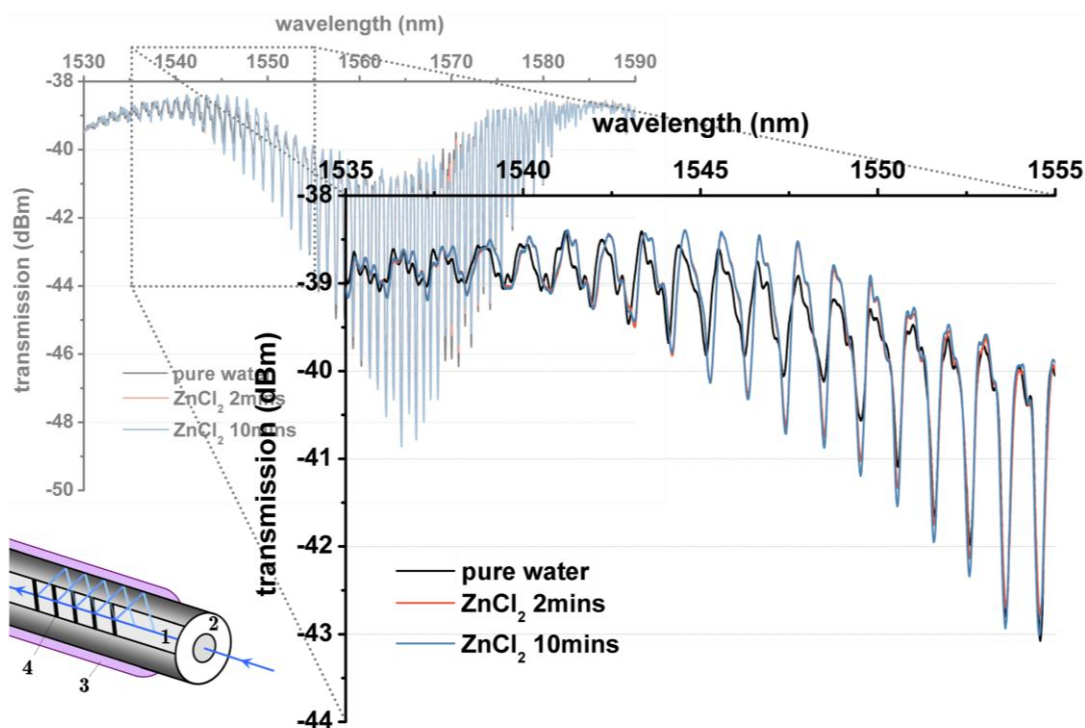

Figure 4.9 Transmission spectrum of the TFBG in pure water (black curve) and in contact with a Zn^{2+} solution for 2 (orange curve) and 10 mins (blue curve) with a zoom over the 1535-1555 nm region; inset: structure of the fibre sensor (1: core, 2: cladding, 3: sol-gel+**1**, 4: TFBG).

After 2 mins of exposure to the Zn^{2+} ions (orange curve), the resonance modes in the range 1543-1550 nm are drastically affected, with an amplitude change of about 1dB at 1548 nm. This results from the fact that, upon complexation, the absorption peak of the sensitive layer shifts to lower wavelengths. As the wavelength-dependent extinction coefficient is related to the imaginary part of the complex refractive index, complexation of the zinc ion induces a refractive index change of the layer, which translates here into a modified transmission spectrum. The second spectrum (blue curve), recorded after 10 mins of exposure, is virtually superimposable to the one measured after 2 mins, illustrating the rapid response of the sensor, as the detection of Zn^{2+} is already achieved in this time range.

4.5   Higher rylene derivatives

Among all the very attractive features of perylene derivatives, the availability of actives sites to efficiently tune the absorption spectrum towards the red part of the spectrum by extending π-conjugation along the molecular long axis constitutes a valuable asset in the context of optical fibre sensing. The reason for this resides in the ability to work at longer wavelengths, thus possibly fitting the windows in the transmission spectrum of glass optical fibres (Figure 4.10). This becomes even more important when the optical fibre technology is used to monitor large structures and the requirement of minimal signal loss is crucial.
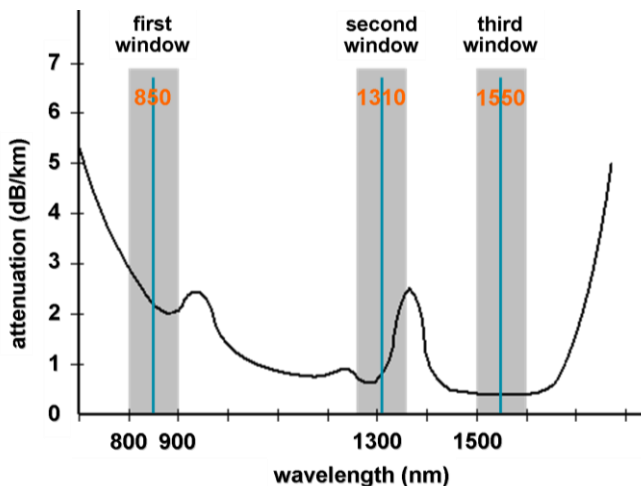
Figure 4.10 Attenuation of the optical signal as a function of the wavelength of the light beam and transmission windows of a glass optical fibre.

More specifically, although the transmission loss is not the lowest in the first window, the possibility to use low-cost optical sources and detectors in the 800-900 nm band makes it very attractive. In this context, we investigated the behaviour of the zinc chemosensor along a series of rylene derivatives in which additional naphtalene units are incorporated between the imide structure and the DPA moiety to yield terrylene derivative TMI-DPA and quaterrylene derivative QMI-DPA (Figure 4.11).[27-29]
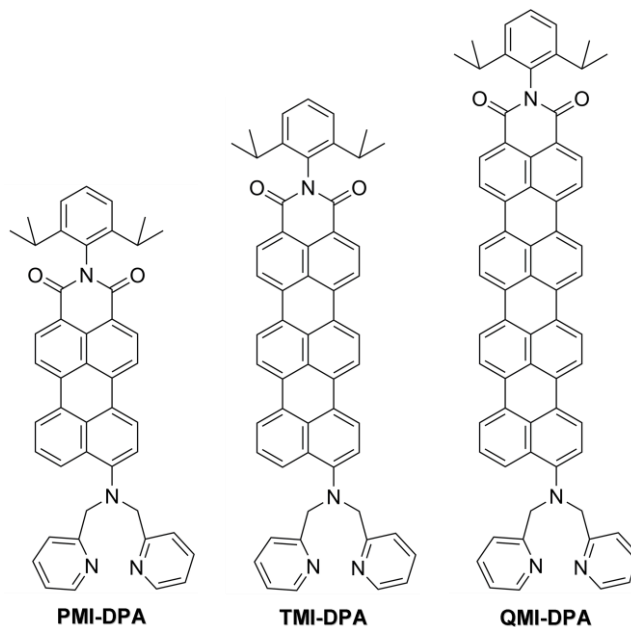
Figure 4.11 Structure of the PMI-DPA sensor and associated higher rylene derivatives, TMI-DPA and QMI-DPA.

Considering the increasing size of the systems, the study of the complexation becomes computationally very heavy and the calculations were thus performed in the gas phase, with chloride ions added in the complexes to complete the coordination of the zinc ion, instead of two solvent molecules. To assess for the potential spectral displacement associated to the complexation event, calculations on the free systems were performed at the same level of theory employed in the study of PMI-DPA, i.e., using DFT at the B3LYP/6-31G(d) level, with the LanL2DZ pseudopotential and basis set to describe Zn^{2+}. We only considered the conformation noted **a** earlier (with CN4 for the metal cation) and simulated the absorption spectra of the free and complexed systems for the two aforementioned higher rylene derivatives, **2a** and **3a**, respectively (Table 4.5).

Table 4.5 Computed wavelengths/energies of the first absorption vertical transition, associated oscillator strengths and shift upon complexation of the zinc ion.

	transition energy (eV)	transition wavelength (nm)	oscillator strength f	shift upon complexation (eV / nm)
1a	2.37	522	0.7286	-
2a	1.94	638	1.2411	-
3a	1.66	749	1.8715	-
1a·$Zn^{2+}_{[CN4]}$	2.47	503	0.7713	0.10 / 19
2a·$Zn^{2+}_{[CN4]}$	2.00	621	1.2598	0.06 / 17
3a·$Zn^{2+}_{[CN4]}$	1.69	732	1.7861	0.03 / 17

Upon extension of the π-conjugated system (PMI-DPA→TMI-DPA→QMI-DPA), the first absorption band is substantially shifted towards longer wavelengths, compared to **1a**, by 116 nm and 227 nm for **2a** and **3a**, respectively. As the transitions computed are all characterised by a HOMO→LUMO excitation, we focused our attention on these orbitals and how they evolve with the length of the system (Figure 4.12). Both frontier orbitals, delocalised over the whole rylene conjugated system, are strongly affected by the increasing π-conjugation of the system and, as the HOMO is destabilised and LUMO stabilised along the series **1a→2a→3a**, the π-conjugation extension is accompanied by a narrowing of the HOMO-LUMO gap (total decrease of 0.93 eV from **1a** to **3a**). We also observe a strengthening of the transition intensity with higher oscillator strength along the series, as a longer conjugation causes an enhancement of the transition dipole moment. This behaviour is in

agreement with the reported dependence between the number of naphtalene units in rylene derivatives and their extinction coefficient.[30]
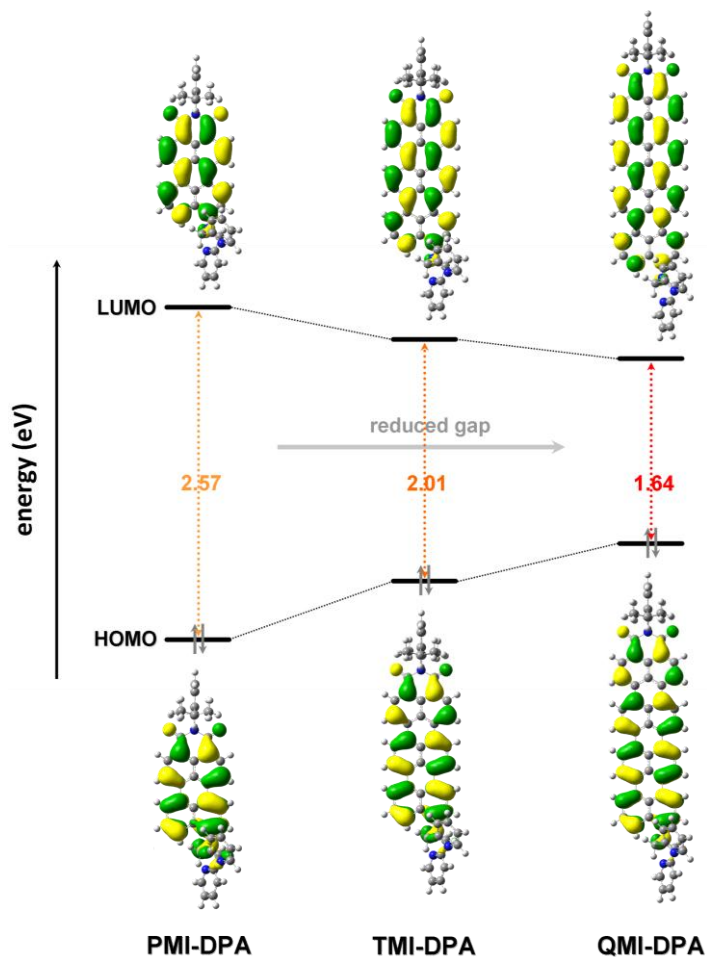
Figure 4.12 Graphical representation of the HOMO and LUMO of perylene derivatives of increasing length and evolution of their energies, with HOMO/LUMO gap values.

The spectral displacement originating from the complexation of Zn^{2+} by **1a** amounts to 19 nm, as calculated in the gas phase. A similar

hypsochromic shift (17 nm) is computed when going from **2a** to **2a·**$Zn^{2+}_{[CN4]}$ and from **3a** to **3a·**$Zn^{2+}_{[CN4]}$. The change in the conformation of **2a** and **3a** upon complexation is similar to that observed in **1a** and the origin for the blue-shift is very likely to arise from electronic effects. To confirm this, the evolution of the frontier orbitals upon complexation was investigated and an asymmetrical stabilisation is observed, with a larger effect on the HOMO, which leads to a wider HOMO-LUMO gap and a blue-shift of the absorption spectrum. Moreover, as in the perylene compound, the electron density in the HOMO for the nitrogen atom bearing the DPA group decreases for the two higher rylene derivatives upon complexation of the cation, resulting in the alteration of the intramolecular charge transfer from the nitrogen lone pair to the imide group. Considering that the zinc ion detection is achieved with higher rylenes, QMI-DPA is a very interesting compound for optical fibre technology as it is optically active in a range of wavelengths close to the first transmission window.

4.6 Exploiting the aza-BODIPY structure for zinc ion detection

BODIPY derivatives can feature the required characteristics for the design of chromoionophores active at wavelengths of ~800 nm and above, taking advantage of the multiple possible modifications of the BODIPY core. More specifically, combining the replacement of the carbon atom in the 8-position by a nitrogen atom with extended conjugation and electron donating group substitution within a rigid structure is expected to result in NIR absorbing and emitting dyes. Gresser et al. reported a series of benzannulated aza-BODIPY dyes, with absorption and fluorescence maxima ranging from 681 to 793 nm and 723 to 841 nm, respectively.[31]
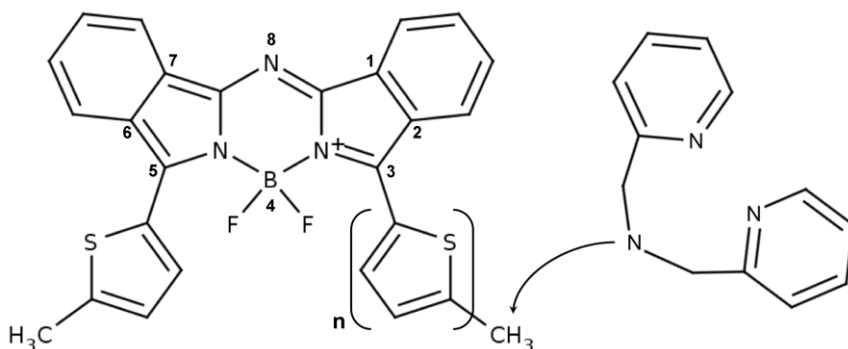
Figure 4.13 Structure of the chromoionophore **BDP-1-DPA** resulting from the combination of the aza-BODIPY derivative reported by Gresser et al. (noted **BDP-1**) with the dipicolylamine unit. Compounds **BDP-2-DPA** and **BDP-3-DPA** are obtained for n=2 and n=3, respectively.

Grafting the DPA unit on the longest-wavelength active compound among the series described by Gresser et al. (dye **BDP-1**) is expected to result in a chromoionophore for zinc ion sensing based on intramolecular charge transfer. This is a consequence of the donor-π-acceptor nature of the system, in which the aza-BODIPY unit acts as the acceptor and the DPA group acts as the donor, operating in a range of wavelengths fitting the first transmission window aforementioned. Increasing the number of thiophene units between the aza-BODIPY and the ionophore is a reasonable approach to allow for further expansion of the π-conjugated system and possible tuning of the sensor response to Zn^{2+}.

Calculations were performed to get insight into the complexation phenomenon and its consequences on the optical properties of **BDP-1-DPA**. We also investigated the influence of the conjugated spacer length by adding one and two thiophene groups, to yield compounds **BDP-2-DPA** and **BDP-3-DPA**, respectively (Figure 4.13). To conserve a

reasonable computational time, no solvent effects were considered and the B3LYP/6-31G(d) level of theory was employed.

4.6.1 Complexation of Zn^{2+} by BDP-1-DPA

We first investigated the impact of grafting the DPA unit on the thiophene group at the 3-position of **BDP-1**. For this purpose, the geometry optimisations of **BDP-1** and **BDP-1-DPA** were performed and the optical properties were simulated. In a second step, the influence of the presence of Zn^{2+} was studied.

The geometry of **BDP-1** is in very good agreement with reported data, as the benzoannulated groups are in the plane of the aza-BODIPY core, and a dihedral angle of ~30° between this rigid plane and the methylthiophene substituents is found (31° reported). The computed absorption maximum is located at 657 nm and corresponds to a HOMO→LUMO excitation (in line with reported calculations at the B3LYP/6-31G(d,p) level).

The grafting of the DPA moiety on **BDP-1-DPA** introduces a further planarisation of the system as, while the dihedral angle between the core and the thiophene at the 5-position remains unchanged (~31°), it decreases to ~25° for the 3-thiophene-DPA substituent. Just as a bathochromic shift is expected to accompany the planarisation of BODIPY derivatives (see chapter 3), more planar aza-BODIPY dyes present a spectral displacement towards longer wavelengths.[32] **BDP-1-DPA** exhibits a maximum absorption band, arising from a HOMO→LUMO transition, at 696 nm, red-shifted by 39 nm compared to **BDP-1**. The evolution of the frontier orbitals illustrates this trend as upon substitution, both levels are substantially destabilised, with a larger effect on the HOMO, in line with the donor character of the DPA unit, yielding a smaller HOMO-LUMO gap.
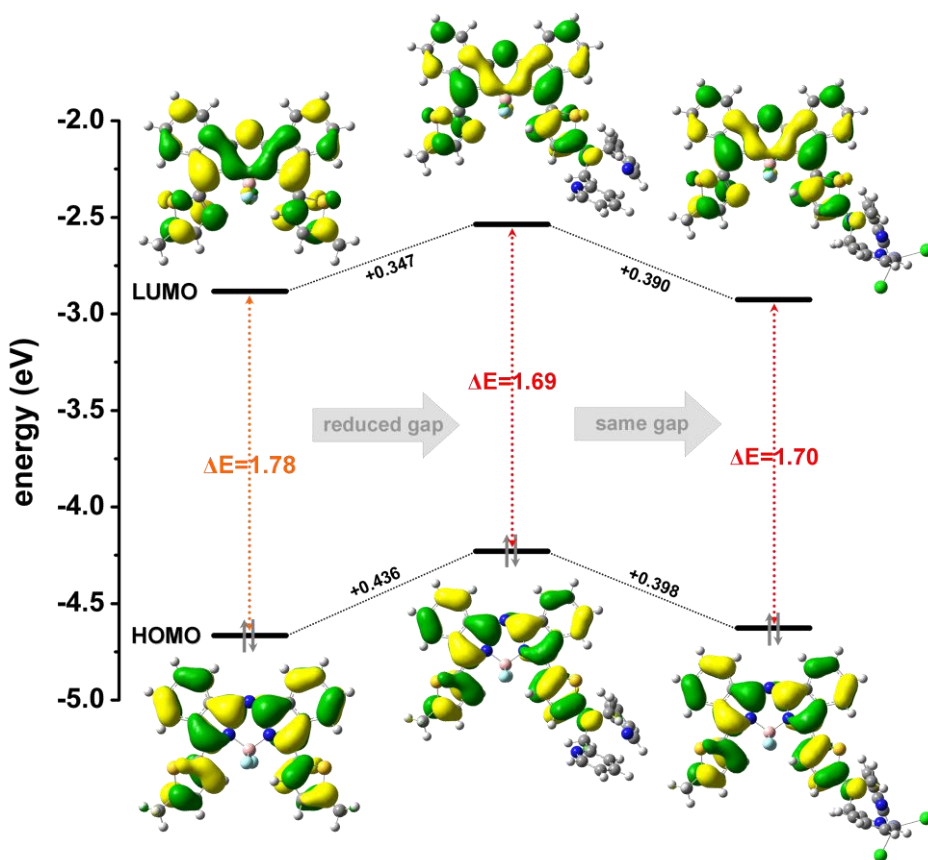
Figure 4.14 Graphical representation and evolution in energy of the frontier orbitals of **BDP-1**, **BDP-1-DPA** and **BDP-1-DPA·**$Zn^{2+}_{[CN4]}$.

Unlike what is observed with the PMI-DPA chromoionophore, the complexation of the zinc ion in the **BDP-1-DPA·**$Zn^{2+}_{[CN4]}$ conformation of the aza-BODIPY-DPA compound (cf. section 4.1) leads to a symmetrical stabilisation of the HOMO and LUMO, so that the energy gap between them remains the same (Figure 4.14). As a result, the absorption maximum is computed at the same wavelength compared as in **BDP-1-**

DPA, which led us to the conclusion that **BDP-1-DPA** is not a suitable compound for use into zinc ion detection applications.

4.6.2   Influence of the π-conjugated spacer length

A bathochromic shift of the absorption maximum being expected as a consequence of the introduction of more repeating unit in donor-π-bridge-acceptor dyes, one and two thiophene units were added to determine the effect of increasing the conjugated spacer length of **BDP-1-DPA**. Expectedly, the supplementary thiophene units allow for an extension of the π-conjugation and are thus responsible for a bathochromic shift of the absorption maximum along the **BDP-1-DPA→BDP-2-DPA→BDP-3-DPA** series. When the spacer is composed of two thiophene groups (in **BDP-2-DPA**), the absorption transition is computed at 750 nm, and reaches 801 nm when a third unit is added; compared to **BDP-1-DPA**, red-shifts of 54 nm and 105 nm are expected for **BDP-2-DPA** and **BDP-3-DPA**, respectively. This spectral behaviour is in accordance with the evolution of the frontier orbitals (involved in the transition), which results in a lowering of the HOMO-LUMO gap: the LUMO orbital is markedly stabilised with the lengthening of the spacer while the HOMO is slightly affected.
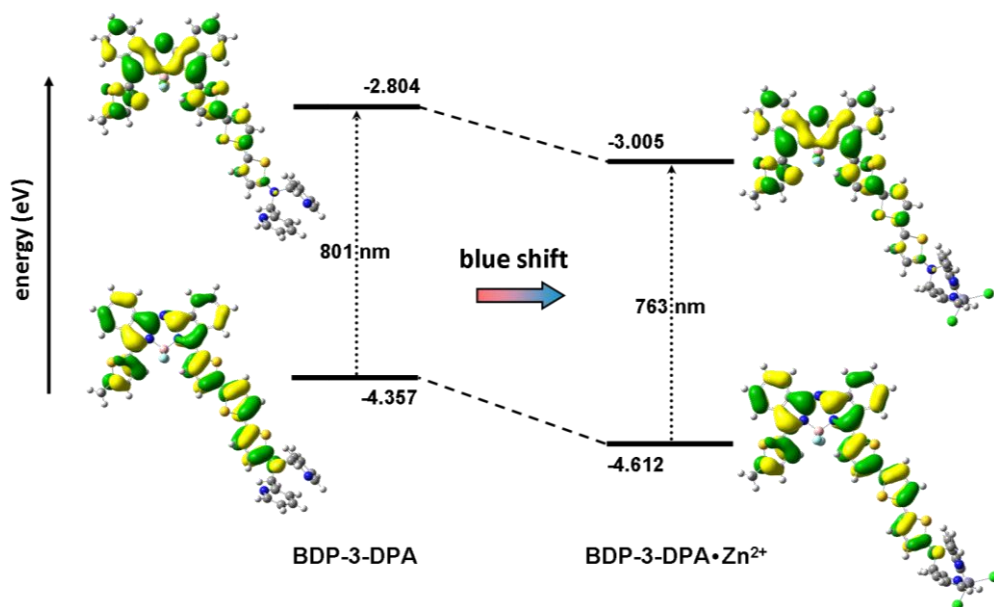
Figure 4.15 Evolution and graphical representation of the frontier orbitals of **BDP-3-DPA** upon complexation of Zn^{2+}.

Considering the interesting behaviour expected from the presence of the terthiophene spacer, we focused on compound **BDP-3-DPA** and investigated the potential optical response of the system upon complexation of the zinc ion. Interestingly, in the presence of Zn^{2+}, the absorption maximum is computed at 763 nm, yielding upon complexation an hypsochromic shift of 38 nm, in the range of what is calculated for the PMI-DPA system. The $S_0 \rightarrow S_1$ transition corresponds to a HOMO→LUMO excitation. In **BDP-3-DPA**, the HOMO orbital is delocalised over the whole π-conjugated system, whereas the LUMO is more centered on the aza-BODIPY unit, with however small weights remaining on the terthiophene (Figure 4.15), indicating that an intramolecular charge transfer occurs between the latter and the aza-BODIPY core. The frontier orbitals of **BDP-3-DPA•**$Zn^{2+}_{[CN4]}$ follow the same trend in terms of delocalisation, with however a HOMO that

presents lower contributions on the terthiophene segment (as compared to **BDP-3-DPA**). The frontier orbital evolution upon complexation is in line with the expected alteration of the ICT caused by the presence of Zn^{2+} already observed for the rylene-DPA systems. Contrary to its counterpart **BDP-1-DPA**, which does not show any optical change in the presence of zinc ion, **BDP-3-DPA** allows for detection of Zn^{2+} and constitutes, on the same grounds as those identified for **QMI-DPA**, an interesting candidate for optical fibre technology.

4.7 Conclusions

In this chapter, we present an in-depth study of chromoionophores for zinc ion detection, combining experimental and theoretical approaches. As the first stage in the study, a perylene monoimide chromophore was combined with a dipicolylamine complexing unit (PMI-DPA). Characterised by an hypsochromic shift of the absorption maximum in solution, the complexation of Zn^{2+} by PMI-DPA also gives rise to a large enhancement of the fluorescence. The quantum-chemical calculations allow to gain further insight into the electronic processes responsible for the spectral displacement of the first absorption band towards smaller wavelengths. Namely, the intrinsic push-pull character of PMI-DPA arising from the acceptor nature of the imide group and donor nature of the dipicolylamine unit results in an intramolecular charge transfer (ICT) upon photoexcitation. The optical response of the chromophore to the Zn^{2+} ions is related to the degree of electronic coupling between the ionophore unit and the perylene unit. More specifically, the DPA nitrogen lone pair being involved in the complexation of Zn^{2+}, its donating strength is reduced, which contributes to the alteration of the ICT and results in the observed blue-shift. The thermodynamics of the complexation of PMI-DPA with Zn^{2+} as well as Cu^{2+} was evaluated theoretically: the results

computed for the copper ion suggest a lower detection efficiency for Zn^{2+} in the case where interfering Cu^{2+} ions would be present.

As we envision the use of PMI-DPA within optical fibre sensor devices, we investigated the possible extension of the wavelength working range of the sensitive compound to fit the "first window" of the transmission spectrum of an optical fibre and thus reduce signal losses. It is shown that by incorporating naphtalene units to yield higher rylene derivatives (terrylene and quaterrylene), the absorption maximum can be bathochromically shifted by up to 227 nm, without altering the process of cation detection. We finally simulated the refractive index change of PMI-DPA upon complexation and showed it is in the range of detection of a tilted fibre Bragg grating (TFBG). In order to demonstrate the feasibility of zinc ion detection in the solid state with fibre sensor technology, we performed a series of experiments in which the optical response upon complexation was measured. We first considered pristine films of PMI-DPA on glass as the active layer, and then we focused on the encapsulation of the dye in a silica sol-gel, improving the response time by an order of magnitude. The very same sensitive sol-gel has been deposited on the TFBG of optical fibres and a significant modification of its transmission spectrum was recorded in the presence of zinc ions. PMI-DPA and the higher rylene compounds can thus be considered as promising systems for the detection of Zn^{2+} ions, both in organic solutions and in thin film sensors.

The inclusion of the DPA unit onto an aza-BODIPY derivative with an oligothiophene spacer of increasing length has been shown to provide interesting optical features with absorption in the NIR region of the spectrum (~800 nm, for the terthiophene-containing compound). As in the perylene derivatives, a significant blue-shift is expected upon complexation of Zn^{2+}.

References

[1]   C. J. Frederickson, J. Y. Koh, A. I. Bush, *Nat. Rev. Neurosci.* **6**, 449 (2005).

[2]   M. P. Cuajunqco, G. J. Lees, *Neurobiol. Dis.* **4**, 137 (1997).

[3]   C. W. Levenson *Nutrition Reviews* **64**, 39 (2006).

[4]   A. Voegelin, S. Pfister, A. C. Scheinost, M. A. Marcus, R. Kretzschmar, *Environ. Sci. Technol.* **39**, 6616 (2005).

[5]   Z. Xu, J. Yoon, D. R. Spring, *Chem. Soc. Rev.* **39**, 1996 (2010).

[6]   A. Bannani, C. Bobisch, R. Moeller, *Science* **315**, 1824 (2007).

[7]   S. Bhosale, A. L. Sisson, P. Talukdar, A. Fuerstenberg, N. Banerji, E. Vauthey, G. Bollot, J. Mareda, C. Roeger, F. Wuerthner, N. Sakai, S. Matile, *Science* **313**, 84 (2006).

[8]   L. Schmidt-Mende, A. Fechtenkotter, K. Müllen, E. Moons, R. H. Friend, J. D. MacKenzie, *Science* **293**, 1119 (2001).

[9]   G. P. Wiederrecht, B. A. Yoon, M. R. Wasielewski, *Science* **270**, 1794 (1995).

[10]   H. Langhals, W. Jona, *Chem. Eur. J.* **4**, 2110 (1998).

[11]   L. Fan, Y. Xu, H. Tian, *Tetrah. Lett.* **46**, 4443 (2005).

[12]   P. Yan, M. W. Holman, P. Robustelli, A. Chowdhury, F. I. Ishak, D. M. Adams, *J. Phys. Chem. B* **109**, 130 (2005).

[13]   Y. Che, A. Datar, K. Balakrishnan, L. Zang, *J. Am. Chem. Soc.* **129**, 7234 (2007).

[14]   X. He, H. Liu, Y. Li, S. Wang, Y. Li, N. Wang, J. Xiao, X. Xu, D. Zhu, *Adv. Mater.* **17**, 2811 (2005).

[15]   A. D. Becke, *J. Chem. Phys.* **98**, 5648 (1993).

[16]   W. R. Wadt, P. J. Hay, *J. Chem. Phys.* **82**, 270 / 284 / 299 (1985).

[17] B. Mennucci, E. Cancès, J. Tomasi, *J. Phys. Chem. B* **101**, 10506 (1997).

[18] Gaussian 09, Revision A.02 and B.012, M. J. Frisch, G. W. Trucks, H. B. Schlegel, G. E. Scuseria, M. A. Robb, J. R. Cheeseman, G. Scalmani, V. Barone, B. Mennucci, G. A. Petersson, H. Nakatsuji, M. Caricato, X. Li, H. P. Hratchian, A. F. Izmaylov, J. Bloino, G. Zheng, J. L. Sonnenberg, M. Hada, M. Ehara, K. Toyota, R. Fukuda, J. Hasegawa, M. Ishida, T. Nakajima, Y. Honda, O. Kitao, H. Nakai, T. Vreven, J. A. Montgomery, Jr., J. E. Peralta, F. Ogliaro, M. Bearpark, J. J. Heyd, E. Brothers, K. N. Kudin, V. N. Staroverov, R. Kobayashi, J. Normand, K. Raghavachari, A. Rendell, J. C. Burant, S. S. Iyengar, J. Tomasi, M. Cossi, N. Rega, J. M. Millam, M. Klene, J. E. Knox, J. B. Cross, V. Bakken, C. Adamo, J. Jaramillo, R. Gomperts, R. E. Stratmann, O. Yazyev, A. J. Austin, R. Cammi, C. Pomelli, J. W. Ochterski, R. L. Martin, K. Morokuma, V. G. Zakrzewski, G. A. Voth, P. Salvador, J. J. Dannenberg, S. Dapprich, A. D. Daniels, O. Farkas, J. B. Foresman, J. V. Ortiz, J. Cioslowski, and D. J. Fox, Gaussian, Inc., Wallingford CT, 2009.

[19] S. Bjelic, I. Jelesarov, *J. Mol. Recogn.* **21**, 289 (2008).

[20] K. Qvortrup, A. D. Bond, A. Nielsen, C. J. McKenzie, K. Kilsa, M. B. Nielsen, *Chem. Comm.* **17**, 1986 (2008).

[21] A. D. Kersey, M. A. Davis, H. J. Patrick, M. LeBlanc, K. P. Koo, C. G. Askins, M. A. Putnam, E. J. Friebele, *IEEE J. Lightwave Technol.* **15**, 1442 (1997).

[22] G. Laffont, P. Ferdinand, *Meas. Sci. Technol.* **12**, 765 (2001).

[23] C. Caucheteur, P. Mégret, *Photon. Technol. Lett.* **17**, 2703 (2005).

[24] C.-F. Chan, C. Chen, A. Jafari, A. Laronche, D. J. Thomson, J. Albert, *Appl. Opt.* **46**, 1142 (2007).

[25] F. Baldini, M. Brenci, F. Chiavaioli, A. Giannetti, C. Trono, *Anal. Bioanal. Chem.* **402**, 109 (2011).

[26] M. Debliquy, J.-M. Renoirt, C. Caucheteur, P. Mégret, M.-G. Olivier, *Proceedings of SPIE Photonics Europe*, paper n° 8439-92 (2012).

[27] F. O. Holtrup, G. R. J. Müller, H. Quante, S. De Feyter, F. C. De Schryver, K. Müllen, *Chem. Eur. J.* **3**, 219 (1997).

[28] H. Langhals, G. Schönmann, L. Feiler, *Tetrahedron Lett.* **36**, 6423 (1995).

[29] Y. Avlasevich, K. Müllen, *J. Org. Chem.* **72**, 10243 (2007).

[30] Y. Avlasevich, C. Li, K. Müllen, *J. Mater. Chem.* **20**, 3814 (2010).

[31] R. Gresser, M. Hummert, H. Hartmann, K. Leo, M. Riede, *Chem. Eur. J.* **17**, 2939 (2011).

[32] W. Zhao, E. M. Carreira, *Chem. Eur. J.* **12**, 7254 (2006).

Conclusions
and perspectives

This work is devoted to the rational development of chromoionophores from a comprehensive understanding of the photophysics underlying the detection process. Using quantum chemical methods in combination with basic spectroscopic experiments, we addressed two aspects of designing molecular sensors for cations, namely, the relationships between the structure and optical properties of the organic chromophore building blocks, and the photophysical processes involved in the cation detection.

As a first step, we focused in chapter 3 on studying series of compounds from the versatile family of BODIPY dyes, to assess the consequences of structural modifications on their optical properties.
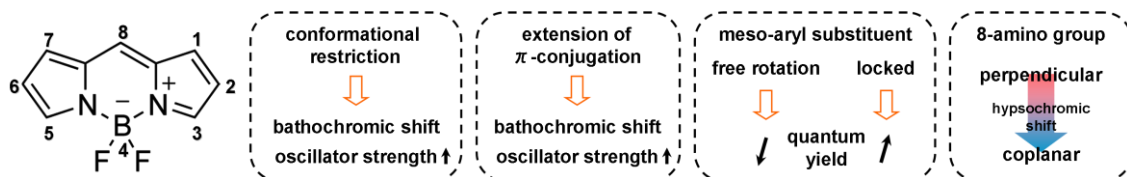
We show that large bathochromic shifts together with higher oscillator strength values can be achieved by imposing conformational constraints via homo- or heterocyclic annulation, as a result of the more rigid structure. More generally, extension of the π-conjugation leads to spectral displacements towards longer wavelengths and can be efficiently obtained by substitution of the BODIPY core, more specifically with electron donating groups. On the one hand, 3,5-symmetrical di-substitution provides further bathochromic shift of the absorption and emission maxima. On the other hand, substitution at the *meso*-position can have very different effects on the optical properties. The introduction of an aryl group at the 8-position does not particularly affect absorption and emission features but allows for a modulation of the fluorescence quantum yield, depending on the possible rotation of the group with respect to the BODIPY core. In constrast, the 8-amino-BODIPY derivatives we studied do not exhibit fluorescence quenching, but provide a way to modulate the optical properties towards shorter wavelengths, owing to the evolution of the absorption maximum with the twist angle between the BODIPY core and the *meso*-substituent.

In chapter 4, we presented a joint experimental/theoretical study of molecular chromoionophores for the detection of the zinc ion. First, we investigated extensively a perylene monoimide (PMI) derivative functionalised with a dipicolylamine (DPA) complexing unit. Based on the experimental observation of a blue-shift of the absorption maximum in the presence of the zinc ion, we performed a theoretical study to unravel the electronic processes responsible for the spectral displacement associated with the Zn^{2+} complexation by PMI-DPA. It turns out that the system, which exhibits an intrinsic push-pull character owing to the acceptor nature of the imide group and the donor nature of DPA, undergoes an intramolecular charge transfer (ICT) upon photoexcitation.

Once the lone pair of the DPA unit gets involved in the complexation of the zinc ion, the ICT is altered and a hypsochromic shift is observed. The thermodynamic characterisation of the complex reveals that the presence of interfering copper ions might result in a lower detection efficiency for Zn^{2+}.

Our research takes place in the framework of optical fibre sensor technology, more specifically for the distributed monitoring of corrosion of galvanised steel. In this context, it is highly desirable to make use of chromoionophores that are optically active in certain ranges of wavelengths, namely, in the transmission windows of the optical fibre, where the signal loss is reduced. For this purpose, we modelled higher rylene derivatives (terrylene and quaterrylene) and showed that the zinc ion detection ability is maintained, while the optical signalling of the complexation event is transposed to longer wavelengths.

Through a series of experiments, we demonstrated the feasibility of a PMI-DPA-based fibre optical sensor for the zinc ion. Starting from pristine films on glass substrates, the dye was then encapsulated in a silica sol-gel to improve the response time. This sol-gel was deposited on the tilted fibre Bragg grating along an optical fibre, whose transmission spectrum was significantly modified in the presence of Zn^{2+}. Perylene derivatives substituted with the dipicolylamine moiety thus constitute promising candidates for the detection of the zinc ion both in solution and in the solid state, and can more specifically be envisioned for implementation on optical fibres.

Along the same line, the combination of the DPA unit with a rigidified aza-BODIPY derivative constitutes another promising platform for ion detection. Upon complexation of the zinc ion, a blue-shift is expected, which relies on the same electronic processes as those identified for the

PMI-DPA system. Owing to their outstanding photophysical properties, and more specifically the high fluorescence quantum yield they display, BODIPY derivatives constitute very attractive candidates for immobilisation (in a sol-gel matrix) or direct grafting at the tip of optical fibres for fluorescence detection. However, very preliminary results of excited-state calculations have suggested a more complex behaviour in the first excited state, with a perpendicular arrangement of the conjugated spacer-DPA moiety with respect to the aza-BODIPY core, and thus a charge transfer (CT) character of the first excited state. Given the known sensitivity of CT to solvent polarity a careful study accounting for the solvent effects is highly desirable to get insight into the excited-state properties of these compounds and assess the consequences of zinc ion complexation and their potential performances as efficient fluorescent Zn^{2+} sensors.

In light of the understanding gained through the study of PMI-DPA and aza-BODIPY-DPA in terms of the mechanisms at stake in the detection process, these systems provide a well-defined platform for further optimisation of the ionophore building block, i.e., the replacement of the dipicolylamine moiety by other zinc ion complexing units.

Given the excellent signal transmission that can be achieved in optical fibres using light beams with wavelengths around 1310 or 1550 nm, the development of chromoionophores active at such longer wavelengths would be of major interest, in particular in the context of distributed monitoring over long distances. In this perspective, two-photon-active systems constitute prime candidates to circumvent the scarcity of chromophores in the long wavelength region. Such molecules can absorb two photons, the transition energy to the excited state corresponding to the sum of the individual photon energies. Following the strategies

already reported for the design of chromophores with large two-photon absorption cross sections, the elaboration of chromoionophores with specific dependence on cation binding of their two-photon spectroscopic properties is of great interest for operating in the range of the 1310 nm transmission window of the optical fibre. The detailed exploration of the non-linear optical properties of PMI-DPA and aza-BODIPY-DPA, as well as the effect of Zn^{2+} complexation on these features, would be an important first step, before devoting efforts to their improvement and, more generally, the optimisation of two-photon-active molecular cation sensors.

Owing to its very attractive properties (lightness, resistance, electrical and thermal conductivity, strength, ductility..), aluminium is one of the most widely used metals in technological applications, for instance in the aeronautic industry and construction. Aluminium is covered by a thin layer of aluminium oxide in the presence of oxygen, which gives it remarkable corrosion resistance. However, once the oxide layer is damaged, aluminium is prone to severe corrosion, with possibly dramatic consequences. The design of chromoionophores for Al^{3+} detection, in possible combination with optical fiber technology, is thus of high interest as an extension of the present work. The high affinity of the Al^{3+} ion for ionophores bearing negatively-charged oxygen atoms leads us to propose the catechol unit as a ligand to be coupled with appropriate chromophores. In the study of those new compounds, particular attention will have to be paid to the pH range in which the sensor has to perform.

Beyond the development of organic molecules for metal ion detection, a very different aspect of cation complexation can also be envisioned, with the theoretical study of the important biological process of metal-induced oxidation of polyphenols and the redox processes related to the

antioxidant/pro-oxidant properties of those polyphenols. As a first step, investigation of the redox properties of the Fe^{III} complexes with model organic ligands such as the catechol unit could be undertaken with the theoretical methodology employed in this work, paving the way towards a comprehensive understanding of the antioxidant activity of polyphenols.

List of Publications

"Synthesis, Spectroscopy, Crystal Structure Determination, and Quantum Chemical Calculations of BODIPY Dyes with Increasing Conformational Restriction and Concomitant Red-Shifted Visible Absorption and Fluorescence Spectra."
V. Leen, W. Qin, W. Yang, J. Cui, C. Xu, X. Tang, W. Liu, K. Robeyns, L. Van Meervelt, D. Beljonne, R. Lazzaroni, **C. Tonnelé**, N. Boens, W. Dehaen.
Chem. Asian J. **5**, 2016 (2009).

"Synthesis of stable free base secochlorins and their corresponding metal complexes from meso-tetraarylporphyrin derivatives."
M. Lo, J.-F. Lefebvre, N. Marcotte, **C. Tonnelé**, D. Beljonne, R. Lazzaroni, S. Clément, S. Richeter.
Chem. Commun. **48**, 3460 (2012).

"Visible Absorption and Fluorescence Spectroscopy of Conformationally Constrained, Annulated BODIPY Dyes."
N. Boens, V. Leen, W. Dehaen, L. Wang, K. Robeyns, W. Qin, X. Tang, D. Beljonne, **C. Tonnelé**, J. M. Paredes, M. J. Ruedas-Rama, A. Orte, L. Crovetto, E. M. Talavera, J. M. Avarez-Pez.
J. Phys. Chem. A, **116**, 9621 (2012).

"UV-Vis spectroscopy of the coupling products of the palladium-catalyzed C-H arylation of the BODIPY core."

L. Wang, B. Verbelen, **C. Tonnelé**, D. Beljonne, R. Lazzaroni, V. Leen, W. Dehaen, N. Boens.

Photochem. Photobiol. Sci. **12**, 835 (2013).

"8-HaloBODIPYs and Their 8-(C, N, O, S) Substituted Analogues: Solvent Dependent UV–vis Spectroscopy, Variable Temperature NMR, Crystal Structure Determination, and Quantum Chemical Calculations."

N. Boens, L. Wang, V. Leen, P. Yuan, B. Verbelen, W. Dehaen, M. Van der Auweraer, W. D. De Borggraeve, L. Van Meervelt, D. Beljonne, R. Lazzaroni, **C. Tonnelé**, M. J. Ruedas-Rama, A. Orte, L. Crovetto, E. M. Talavera, J. M. Alvarez-Peze.

Submitted

"Functional Layers for Zn^{II} Ion Detection : From Molecular Design to Optical Fiber Sensors."

Z. Liu°, **C. Tonnelé°**, G. Battagliarin, C. Li, R. A. Gropeanu, T. Weil, M. Surin, D. Beljonne, R. Lazzaroni, M. Debliquy, J-M.Renoirt, K. Müllen.

Submitted (°co-first authors)

"Fe-Catechol complexes: a model system to study the oxidation of polyphenols."

C. Tonnelé, D. Beljonne, R. Lazzaroni, O. Dangles, P. Trouillas.

In preparation